OPTICAL AND ELECTRONIC STUDIES OF AIR-SENSITIVE VAN DER WAALS MATERIALS ENCAPSULATED BY HEXAGONAL BORON NITRIDE

Dennis Wang

Submitted in partial fulfillment of the

requirements for the degree of

Doctor of Philosophy

in the Graduate School of Arts and Sciences

COLUMBIA UNIVERSITY

2018

ABSTRACT

OPTICAL AND ELECTRONIC STUDIES OF AIR-SENSITIVE VAN DER WAALS MATERIALS ENCAPSULATED BY HEXAGONAL BORON NITRIDE

Dennis Wang

Layered van der Waals materials have played a pivotal role in expanding the scope of condensed matter physics by examining the effects of reduced dimensionality in various systems. These include semiconductors, ferromagnets, and charge density wave materials, among many others. Hexagonal boron nitride (hBN) is often used as a passivation/encapsulation layer for air-sensitive materials in optical and electronic studies owing to its effectiveness as a substrate for graphene in transport measurements. In this thesis, samples probed by Raman spectroscopy and as well as those measured through electronic transport were first encapsulated during fabrication. The specific experimental details are found in each corresponding chapter.

This thesis aims to characterize several 2-D materials and explore physical phenomena arising from combinations thereof through optical and electronic means. Before delving into the specific research projects, it provides a motivation for each, descriptions of the material(s) involved, and sample fabrication techniques used to assemble the various heterostructures. Topics to be covered include the effects of encapsulation on the transition metal dichalcogenide (TMD) 1T'-$MoTe_2$ subject to elevated temperatures, how the nearly commensurate to commensurate phase transition of another TMD, the charge density wave material 1T-TaS_2, in its few-layer form can be tuned electronically, preliminary results of electronic transport in graphene-ferromagnet heterostructures, and an outline of other optical studies on mono- to few-layered forms of related materials and possible future directions that may be pursued.

Contents

List of Figures

List of Tables

Acknowledgments

I would like to thank everyone who made this thesis possible.

First and foremost, I would like to thank Professor Irving P. Herman and Professor Abhay Pasupathy, my thesis co-advisers at Columbia University, for their mentorship and guidance on my research projects. They have opened my eyes to what science is all about.

Second, I would like to thank Dr. Wei Tsen, Dr. Jayakanth Ravichandran, Dr. Datong Zhang, and Dae In Kim for introducing me to electronic transport and optical measurements as I was just getting started, and I would like to extend a special thanks to Kori Smyser for her help with the 1T'-$MoTe_2$ project. I also thank all of my fellow lab colleagues, including Dr. Christopher Gutierrez, Dr. Daniel Rhodes, Dr. Youngduck Kim, Dr. Sanghoon Chae, Dr. Ali Dadgar, Dr. Younghun Jung, Dr. Carlos Forsythe, Dr. Tarun Chari, Alex Kerelsky, Andrew Wieteska, Apoorv Jindal, Benjamin Foutty, Bumho Kim, Drew Edelberg, En-Min Shih, Erick Andrade, Evan Telford, Jiayang Hu, Josh Swann, Minyong Han, Theo Axenie, Yihang Zeng, and all other masters and undergraduate students who have given me a helping hand. Furthermore, I would like to thank Chanul Kim, Christopher Choi, E-Dean Fung, Peijie Ong, and Timothy Liu, my former classmates, for their encouragement during difficult times.

Third, I thank Professor Jim Hone, Professor Cory Dean, Professor Ken Shepard, and Professor Philip Kim for generously allowing me to work in their labs on a regular basis.

Finally, I acknowledge all the funding agencies that have provided support for these studies, including the IGERT (DGE-1069240) and MRSEC (DMR-1420634) programs of the National Science Foundation and the Department of Energy (DE-SC0016703).

Dedication

To my parents,

Dr. Jian-Juei Wang

&

Dr. Shiu-Sian Angel Hsu

Chapter 1

Background and overview of the dissertation

1.1 Introduction

Spurred on by the experimental discovery of isolated monolayer graphene, a multitude of studies over the past decade or so have examined two-dimensional (2-D) materials from the standpoint of their mechanical, optical, and electronic properties. [1-3] These materials possess interlayer bonds arising from van der Waals adhesion that are much weaker than their intralayer ones, allowing for the famous "scotch tape method," also known as micromechanical exfoliation, whereby bulk crystals are thinned down to multi-, few-, or monolayers that can in turn be mixed and matched with other materials to form various vertical heterostructures. [4] It is particularly interesting to compare and contrast the properties of bulk crystals with their ultrathin counterparts and how they interact with their surroundings.

Sometimes, however, interactions with the environment are not desirable because of their adverse effects on materials properties. This is precisely the case for air-sensitive materials, the main focus of this dissertation. It is also where hexagonal boron nitride (hBN) comes to the rescue, as expounded upon below.

With applications ranging from cosmetics to lubricants [5, 6], hBN is a versatile material that found its way into condensed matter physics because of its excellent chemical and thermal stability. Specifically, researchers discovered that, as a substrate, using it as part of the heterostructure improved the mobility of graphene devices by almost an order of magnitude compared to those on SiO_2. [7] hBN, a large band gap insulator with large optical phonon modes, also possesses an atomically smooth surface with few dangling bonds, making it an ideal

encapsulating layer for air-sensitive materials and combinations thereof in optical and electronic transport measurements. This dissertation details several experiments that were enabled by the presence of hBN as an encapsulating layer.

1.2 Summary of experiments

Chapter 2 provides an in-depth treatment of more or less standardized nanofabrication methods common to all projects while leaving project-specific techniques to their respective chapters. It covers everything from micromechanical exfoliation, the technique that revolutionized experimental physics in 2-D, to the assembly of van der Waals heterostructures, an extension that allows materials to be stacked together and their collective properties examined as a whole – or, in case of a single material encapsulated by hBN, its intrinsic properties examined with minimal external perturbations except those deliberately applied.

Chapters 3 and 4 contain studies of two layered transition metal dichalcogenides (TMDs): 1T'-$MoTe_2$ and 1T-TaS_2, respectively. TMDs, which take on the form MX_2 (where M is the transition metal and X is the chalcogen), are best known for the fact that several of them are semiconductors with an indirect band gap in their multilayer form but a direct band gap in their monolayer form. In recent years there have been extensive studies of certain TMDs displaying more exotic phenomena in the ultrathin limit, including charge density waves [8-14] and superconductivity [15-19], among others.

The distorted octahedral form of molybdenum ditelluride, 1T'-$MoTe_2$, is one such example – contrary to its trigonal prismatic polytype, 2H-$MoTe_2$, theory has predicted that a monolayer of 1T'-$MoTe_2$ belongs to a class of quantum spin Hall insulators, of interest to both fundamental physics as well as for fabricating field-effect transistors. [20] A schematic of the

three TMD polytypes (2H, 1T, and 1T') is shown in Fig. 1.1. Structurally, the chalcogen atoms in a 1T crystal are rotated 60° about the c-axis relative to those in a 2H crystal, while the transition metal atoms in a 1T' crystal are also displaced to form 1-D zigzag chains.

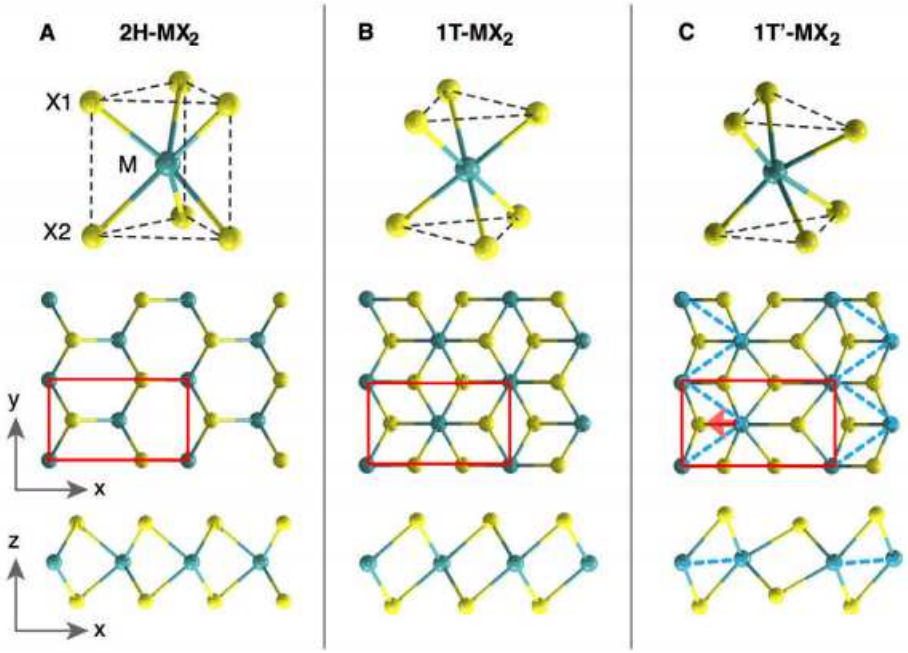

Figure 1.1: Atomistic structure of monolayer transition metal dichalcogenide MX_2. (a) 2H-MX_2 where M atoms are trigonal-prismatically coordinated by six X atoms, forming ABA stacking with the P6m2 space group. (b) 1T-MX_2 where M atoms are octahedrally coordinated with the nearby six X atoms, forming ABC stacking with the P3m1 space group. (c) 1T'-MX_2, where the distorted M atoms form one-dimensional zigzag chains indicated by the dashed blue line. Their unit cell is indicated by red rectangles. Reproduced from Ref. [20].

The quantum spin Hall effect is a member of the "quantum Hall trio," the other two being the quantum Hall and quantum anomalous Hall (the latter will be discussed in Chapter 5). [21] A schematic of all three is shown in Fig. 1.2. It is characterized by counter-propagating modes along the edge of the sample in the absence of an externally applied magnetic field, where the direction of propagation depends on the spin of the electron.

Chapter 3 of this dissertation explains how optical microscopy, Raman spectroscopy, and atomic force microscopy (AFM) were utilized to quantify the rate at and extent to which heating both encapsulated and unencapsulated 1T'-$MoTe_2$ in an inert environment compromise the material integrity; it is found that hBN does, in fact, delay the onset of structural damage and thus serves as an effective passivation layer.

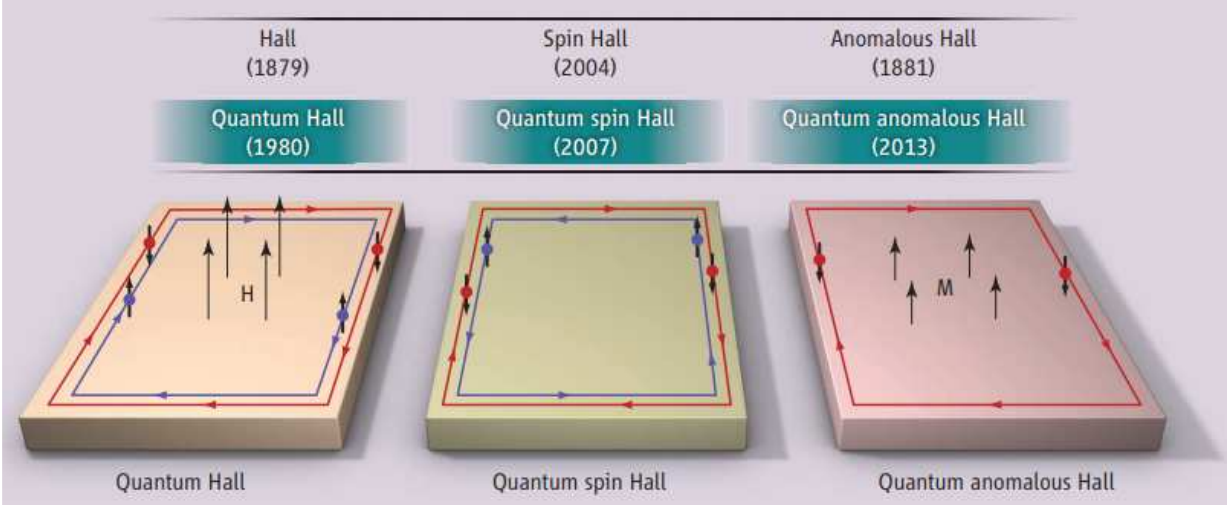

Figure 1.2: Numbers in parentheses indicate the years of each discovery. H is the external magnetic field, and M is the magnetization. For all three quantum Hall effects, electrons flow through the lossless edge channels, with the rest of the system insulating. When there is a net forward flow of electrons for Hall resistance measurement, (left) those extra electrons occupy only the left edge channels in the quantum Hall system regardless of their spins, (center) opposite-spin electrons occupy opposite sides in the quantum spin Hall system, and (right) only spin-down electrons flow through the left edge in the quantum anomalous Hall system. The locking schemes between spin and flow direction, and the number of edge channels depend on the material details, and only the simplest cases are illustrated here. Reproduced from Ref. [21].

Chapter 4 of this dissertation shifts the focus to 1T-TaS_2, an octahedral polytype of TaS_2 (structure shown in Fig. 1.1) that, given its tendency to oxidize, also requires encapsulation by hBN. It is known for its distinct charge density wave (CDW) phases, transforming from the commensurate (C) to nearly commensurate (NC) and finally incommensurate (IC) phase with increasing temperature. In general, a CDW consists of a periodic, spatially modulated array of

electrons throughout a 1-D linear chain compound or 2-D layered crystal accompanied by a concomitant periodic distortion of the atomic lattice. A simplified 1-D model of this is illustrated schematically in Fig. 1.3, where the ions are shown in red and the electron density in blue. [22]

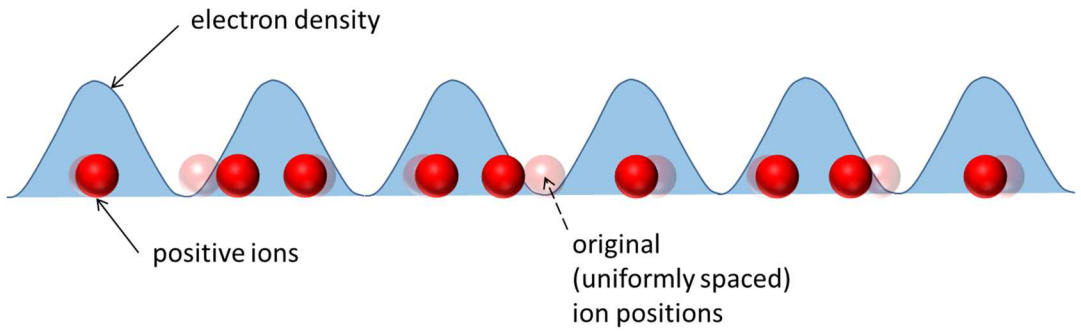

Figure 1.3: Schematic of CDW in one dimension showing the displacement of ions (red) and the modulation in electron density (blue). Reproduced from Ref. [22].

The NC to C phase transition in 1T-TaS_2 occurs simultaneously with a first-order metal-to-insulator transition (MIT). As its name suggests, a MIT turns a material from electrically conductive, like a metal, to electrically insulating. Microscopically, this phenomenon exemplifies the importance of electron-electron correlations in strongly correlated materials – namely, materials with partially filled electronic bands can still exhibit insulating behavior due to pronounced Coulomb repulsion between electrons, contrary to classical band theory. By combining electronic transport data with results from infrared nanoimaging, it is demonstrated that the NC-C phase transition in 1T-TaS_2 depends on the temperature, material thickness, and electrical current running through it, rendering it highly tunable.

Chapter 5 of this dissertation examines the coupling between graphene and another class of van der Waals materials that until recently has eluded the spotlight: magnetism. Once again, this stems from the propensity of layered, chromium-based magnets, including chromium trihalides of the form CrX_3 (X = Cl, Br, and I) and the ternary compounds $CrSiTe_3$ and

$Cr_2Ge_2Te_6$, to degrade in air and highlights the need for hBN encapsulation. Before delving into the mechanisms through which graphene and these magnets interact, giving rise to exotic physical phenomena, the following section is devoted to characterizing each individually.

As previously mentioned, graphene is the quintessential 2-D material, the first of its kind to be isolated down to a monolayer despite long-standing speculations that this was not possible from a theoretical energetics standpoint. [23] It consists of carbon atoms arranged in a honeycomb lattice, with nearest neighbors occupying inequivalent sites – these are depicted by sites A (blue) and B (yellow) in Fig. 1.4 (left). As its name suggests, hBN has an identical structure except with boron and nitrogen atoms occupying all A sites or all B sites or vice versa. hBN and graphene also have a lattice mismatch of less than 2%. Graphene, a zero-bandgap semiconductor, possesses a linear energy dispersion near its K and K' points at the edge of its Brillouin zone, known as Dirac peaks. Roughly speaking, the slope of the Dirac peak (resistance versus gate voltage in electronic measurements) provides a measure of sample quality – the steeper the slope, the higher the mobility. The energy dispersion of graphene in one Brillouin

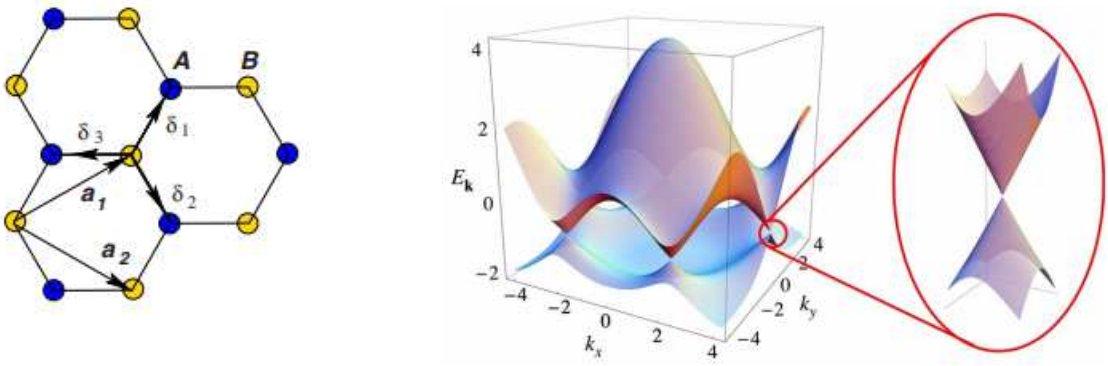

Figure 1.4: (left) Honeycomb lattice structure of graphene, made out of two interpenetrating triangular lattices (a_1 and a_2 are the lattice unit vectors, and δ_i, i = 1, 2, 3 are the nearest-neighbor vectors. (right) Electronic dispersion in the honeycomb lattice, where the vertical energy scale is in units of the nearest-neighbor hopping energy (t = 2.7 eV). The circled region zooms in on energy bands close to the Dirac points. Reproduced from Ref. [23].

zone and a close-up at one of its Dirac peaks is shown in Fig. 1.4 (right). The absence of a bandgap allows one to continuously tune its carrier density from the electron to hole side by gating.

Unlike graphene, chromium trihalides are intrinsically magnetic and possess a bandgap. Structurally, they consist of Cr^{3+} ions in a honeycomb network with six octahedrally coordinated X^- ions attached to each, as in Fig. 1.5 (left). The two CrX_3 compounds considered here are $CrCl_3$ and CrI_3, both of which undergo a crystallographic phase transition from a monoclinic to

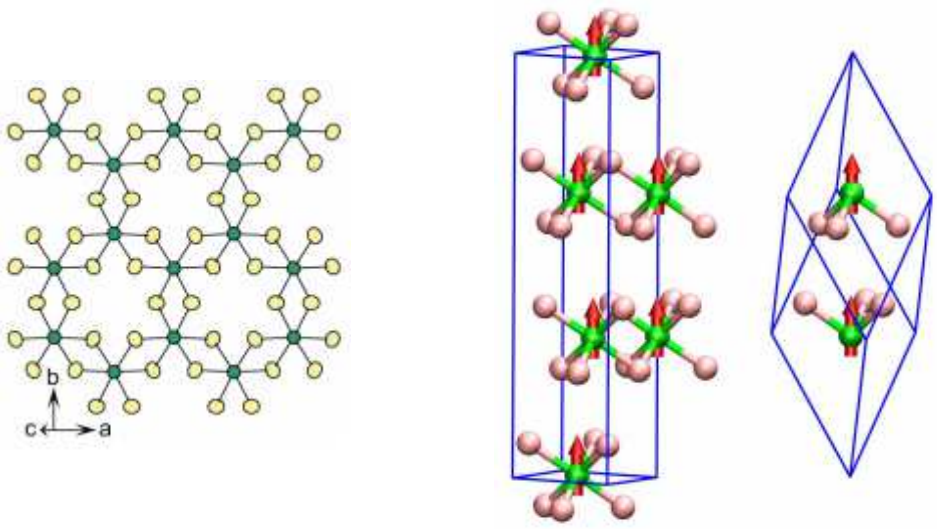

Fig. 1.5: (left) Single CrX_3 layer with a viewing direction normal to the *ab* plane. Cr and halogen atoms are denoted by turquoise and yellow circles, respectively. Reproduced from Ref. [24]. (right) Monoclinic (middle) and rhombohedral (far right) lattices of CrX_3 at high and low temperatures, respectively. The red arrows represent the spin direction of Cr atoms. Reproduced from Ref. [25].

rhombohedral structure from high to low temperatures, shown in Fig. 1.6 (right). This occurs near 240 K and 200 K for $CrCl_3$ and CrI_3, respectively. $CrCl_3$ is a Mott-Hubbard insulator with intralayer ferromagnetic ordering and interlayer antiferromagnetic ordering ($T_C \sim 17$ K) that are in-plane but can be reoriented out-of-plane by applying an external perpendicular magnetic field of only ~ 0.6 T. CrI_3, a ferromagnetic insulator with a measured bandgap of 1.2 eV and an out-

of-plane magnetic moment, has the highest bulk magnetic ordering temperature (T_C = 61 K) and strongest magnetic anisotropy among the chromium trihalides, thanks to increased spin orbit coupling associated with iodine. [26]

Using the magneto-optical Kerr effect (MOKE), it was recently demonstrated that the monolayer and trilayer forms of CrI_3 retain the ferromagnetism of the bulk compound while bilayer CrI_3 is metamagnetic. [27] In a separate study, graphene was shown to couple strongly to semiconducting TMDs through the spin-orbit interaction [28], begging the question of whether or not it is just as strong in other materials as well. These facts motivated the introduction of ferromagnetism in graphene through the exchange interaction and strong spin-orbit coupling by placing it in close proximity to a ferromagnetic material. The anomalous Hall effect (AHE), seen in graphene placed atop a yttrium iron garnet (YIG) ferromagnetic thin film and manifesting as a nonlinear Hall resistivity at small, externally applied magnetic fields, verifies this possibility. [29, 30] Moreover, it has also been suggested that the aforementioned quantum anomalous Hall effect (QAHE) can be realized in graphene heterostructures at significantly higher temperatures than in chromium-doped $(Bi,Sb)_2Te_3$ thin films, the only experimental observation of the QAHE thus far, because in principle the former has far less disorder. [31, 32]

Finally, Chapter 6 of this dissertation discusses the use of Raman spectroscopy to characterize the layer number for several 2-D materials in their few-layer form, as had been done previously for graphene [33] and various other TMDs [34-36]. It also outlines potential avenues for future work. The materials studied here include $ZrTe_5$, 1T'-$MoTe_2$, $CrSiTe_3$, and $CrCl_3$, the motivation being that this optical technique offers a quick, reliable, and noninvasive way to determine sample thickness without having to perform AFM each time. Like 1T'-$MoTe_2$, the monolayer form of $ZrTe_5$ was also predicted to be a quantum spin Hall insulator. [37] Its

structure consists of trigonal prismatic chains of $ZrTe_3$ along the *a* axis linked by parallel chains of Te atoms along the *c* axis; this is illustrated in Fig. 1.6 from several different angles. Like $CrCl_3$, $CrSiTe_3$ is a potential candidate for the ferromagnet in graphene-ferromagnet heterostructures that may give rise to the QAHE. It is an indirect layered semiconductor with a band gap of 0.4 eV [38] and displays ferromagnetic ordering in the bulk at 32 K [38, 39]. $CrSiTe_3$ is composed of Cr and Si atoms sandwiched between planes of Te atoms, as shown in Fig. 1.7.

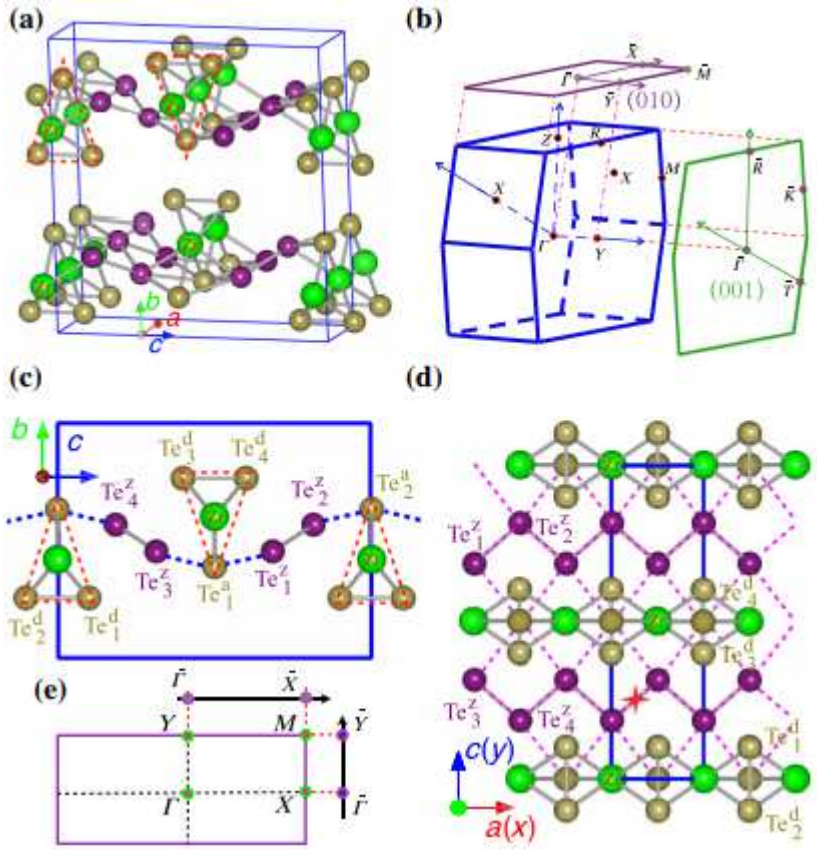

Figure 1.6: (a) Crystal structure of $ZrTe_5$. (b) The bulk Brillouin zone (BZ) and the projected surface BZ of 3-D $ZrTe_5$ ($HfTe_5$). (c), (d), and (e) The side view, top view, and BZ of the single-layer structure, respectively. In (d), the inversion center is indicated by the red star symbol, and the waved grid of the Te square lattice sheet is shown by the pink dotted lines. Reproduced from Ref. [37].

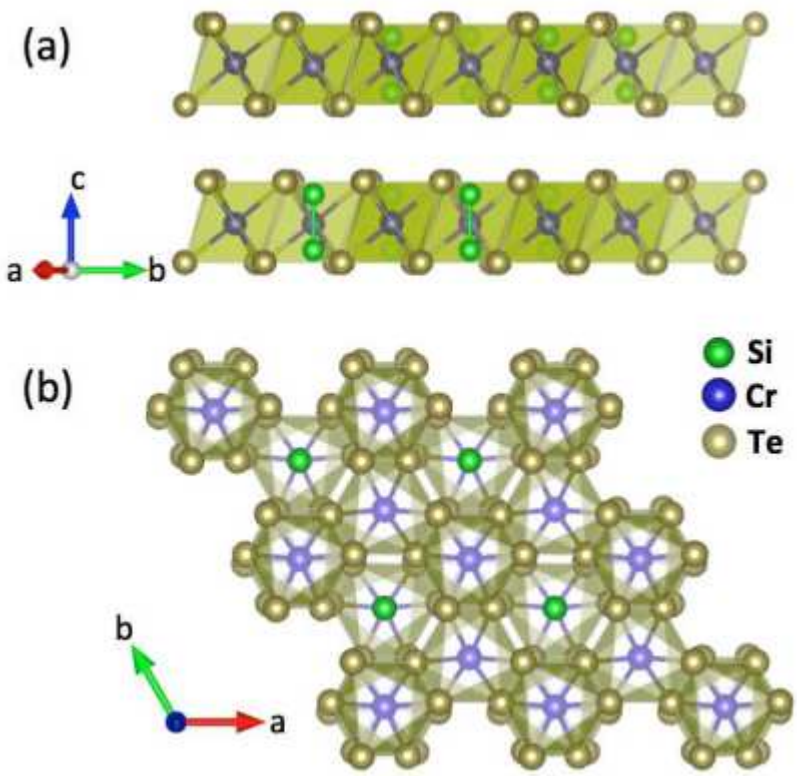

Figure 1.7: Side (a) and top (b) views of the atomic structure for 2-D $CrSiTe_3$. Reproduced from Ref. [40].

1.3 References

1. Wang, Qing Hua, et al. "Electronics and optoelectronics of two-dimensional transition metal dichalcogenides." *Nature Nanotechnology* 7.11 (2012): 699.
2. Butler, Sheneve Z., et al. "Progress, challenges, and opportunities in two-dimensional materials beyond graphene." *ACS Nano* 7.4 (2013): 2898-2926.
3. Xu, Mingsheng, et al. "Graphene-like two-dimensional materials." *Chemical Reviews* 113.5 (2013): 3766-3798.
4. Geim, Andre K., and Irina V. Grigorieva. "Van der Waals heterostructures." *Nature* 499.7459 (2013): 419.
5. Engler, Martin, et al. "Hexagonal boron nitride (hBN): applications from metallurgy to cosmetics." *CFI. Ceramic Forum International*. Vol. 84. No. 12. Göller, 2007.
6. Schwetz, Karl A. "Boron carbide, boron nitride, and metal borides." *Ullmann's Encyclopedia of Industrial Chemistry* (1985).
7. Dean, Cory R., et al. "Boron nitride substrates for high-quality graphene electronics." *Nature Nanotechnology* 5.10 (2010): 722.
8. Goli, Pradyumna, et al. "Charge density waves in exfoliated films of van der Waals materials: evolution of Raman spectrum in $TiSe_2$." *Nano Letters* 12.11 (2012): 5941-5945.
9. Ugeda, Miguel M., et al. "Characterization of collective ground states in single-layer $NbSe_2$." *Nature Physics* 12.1 (2016): 92.
10. Albertini, Oliver R., et al. "Zone-center phonons of bulk, few-layer, and monolayer 1T-TaS_2: Detection of commensurate charge density wave phase through Raman scattering." *Physical Review B* 93.21 (2016): 214109.

11. He, Rui, et al. "Distinct surface and bulk charge density waves in ultrathin 1T-TaS_2." *Physical Review B* 94.20 (2016): 201108.
12. Xi, Xiaoxiang, et al. "Strongly enhanced charge-density-wave order in monolayer $NbSe_2$." *Nature Nanotechnology* 10.9 (2015): 765.
13. Yu, Yijun, et al. "Gate-tunable phase transitions in thin flakes of 1T-TaS_2." *Nature Nanotechnology* 10.3 (2015): 270.
14. Yoshida, Masaro, et al. "Controlling charge-density-wave states in nano-thick crystals of 1T-TaS_2." *Scientific Reports* 4 (2014): 7302.
15. Saito, Yu, Tsutomu Nojima, and Yoshihiro Iwasa. "Highly crystalline 2D superconductors." *Nature Reviews Materials* 2.1 (2017): 16094.
16. Xi, Xiaoxiang, et al. "Ising pairing in superconducting $NbSe_2$ atomic layers." *Nature Physics* 12.2 (2016): 139.
17. Cao, Y., et al. "Quality heterostructures from two-dimensional crystals unstable in air by their assembly in inert atmosphere." *Nano Letters* 15.8 (2015): 4914-4921.
18. Navarro-Moratalla, Efrén, et al. "Enhanced superconductivity in atomically thin TaS_2." *Nature Communications* 7 (2016): 11043.
19. de la Barrera, Sergio C., et al. "Tuning Ising superconductivity with layer and spin-orbit coupling in two-dimensional transition-metal dichalcogenides." *arXiv preprint arXiv:1711.00468* (2017).
20. Qian, Xiaofeng, et al. "Quantum spin Hall effect in two-dimensional transition metal dichalcogenides." *Science* (2014): 1256815.
21. Oh, Seongshik. "The complete quantum Hall trio." *Science* 340.6129 (2013): 153-154.

22. Kogar, Anshul. *This Condensed Life* https://thiscondensedlife.wordpress.com/category/screening/ (2016).
23. Neto, AH Castro, et al. "The electronic properties of graphene." *Reviews of Modern Physics* 81.1 (2009): 109.
24. McGuire, Michael A., et al. "Coupling of crystal structure and magnetism in the layered, ferromagnetic insulator CrI_3." *Chemistry of Materials* 27.2 (2015): 612-620.
25. Zhang, Wei-Bing, et al. "Robust intrinsic ferromagnetism and half semiconductivity in stable two-dimensional single-layer chromium trihalides." *Journal of Materials Chemistry C* 3.48 (2015): 12457-12468.
26. Lado, Jose L., and Joaquín Fernández-Rossier. "On the origin of magnetic anisotropy in two dimensional CrI_3." *2D Materials* 4.3 (2017): 035002.
27. Huang, Bevin, et al. "Layer-dependent ferromagnetism in a van der Waals crystal down to the monolayer limit." *Nature* 546.7657 (2017): 270.
28. Wang, Zhe, et al. "Origin and magnitude of 'designer' spin-orbit interaction in graphene on semiconducting transition metal dichalcogenides." *Physical Review X* 6.4 (2016): 041020.
29. Wang, Zhiyong, et al. "Proximity-induced ferromagnetism in graphene revealed by the anomalous Hall effect." *Physical Review Letters* 114.1 (2015): 016603.
30. Tang, Chi, et al. "Approaching quantum anomalous Hall effect in proximity-coupled YIG/graphene/h-BN sandwich structure." *APL Materials* 6.2 (2018): 026401.
31. Chang, Cui-Zu, et al. "Experimental observation of the quantum anomalous Hall effect in a magnetic topological insulator." *Science* (2013): 1232003.

32. Zhang, Jiayong, et al. "Robust quantum anomalous Hall effect in graphene-based van der Waals heterostructures." *Physical Review B* 92.16 (2015): 165418.

33. Ferrari, Andrea C., et al. "Raman spectrum of graphene and graphene layers." *Physical Review Letters* 97.18 (2006): 187401.

34. Wang, Qing Hua, et al. "Electronics and optoelectronics of two-dimensional transition metal dichalcogenides." *Nature Nanotechnology* 7.11 (2012): 699.

35. Terrones, H., et al. "New first order Raman-active modes in few layered transition metal dichalcogenides." *Scientific Reports* 4 (2014): 4215.

36. Zhang, Xin, et al. "Phonon and Raman scattering of two-dimensional transition metal dichalcogenides from monolayer, multilayer to bulk material." *Chemical Society Reviews* 44.9 (2015): 2757-2785.

37. Weng, Hongming, Xi Dai, and Zhong Fang. "Transition-metal pentatelluride $ZrTe_5$ and $HfTe_5$: A paradigm for large-gap quantum spin Hall insulators." *Physical Review X* 4.1 (2014): 011002.

38. Casto, L. D., et al. "Strong spin-lattice coupling in $CrSiTe_3$." *APL Materials* 3.4 (2015): 041515.

39. Carteaux, V., et al. "Magnetic structure of the new layered ferromagnetic chromium hexatellurosilicate $Cr_2Si_2Te_6$." *Journal of Magnetism and Magnetic Materials* 94.1-2 (1991): 127-133.

40. Lin, Ming-Wei, et al. "Ultrathin nanosheets of $CrSiTe_3$: a semiconducting two-dimensional ferromagnetic material." *Journal of Materials Chemistry C* 4.2 (2016): 315-322.

Chapter 2

Experimental methods

2.1 Overview

The fabrication of layered heterostructures amounts to finding suitable flakes of the desired materials from the bulk crystal, stacking them on top of one another, and performing any additional steps necessary for the sample at hand. A transport device, for instance, would require lithography and wirebonding in order to carry out electrical measurements on it. This section discusses in detail the set of procedures used to fabricate such heterostructures. Lithography and any experimental methods geared towards samples for a specific measurement technique (say, transport) are expounded on in later chapters as they arise. See, for example, Ref. [1].

2.2 Micromechanical exfoliation

4-inch wafers made of 285 nm thick silicon dioxide (SiO_2) on silicon (Si) are first diced into squares that are roughly 1 cm long on each side. The exact side length does not matter unless electron-beam lithography is to be performed on the chip later on, in which case the tool specifications may have more stringent requirements. These squares are sonicated for 15 minutes in acetone to remove organic residues from their surface and sprayed with isopropyl alcohol (IPA) before being dried with a nitrogen gun. Bulk crystals of the material at hand are placed onto Magic scotch tape, which is folded on top of itself repeatedly until the remaining material looks nearly transparent, at which point the tape is put in contact with the pre-cleaned substrate and gently pressed down (or "scratched"). Once there are few to no bubbles between the two surfaces, the chip is held down with a tweezer while the tape is peeled off very slowly starting

from one of its corners. Ideally, the tape does not re-adhere to the substrate during delamination to minimize the presence of tape residue on the SiO_2. Flakes of different thicknesses have different degrees of optical contrast when viewed under an optical microscope due to interference effects from the substrate; these colors can be used to estimate the flake thicknesses or, if a more precise value is desired, the flake height can be measured using atomic force microscopy (AFM).

2.3 Transfer and pickup procedures

To prepare a sample for encapsulation and/or pickup, the above procedure is done twice, each time on a separate substrate: once for hexagonal boron nitride (hBN) and once for the material to be encapsulated and/or picked up. In parallel, polypropylene carbonate (PPC) is spincoated at an appropriate rate and acceleration onto a bare Si chip, also approximately 1 cm^2 in area, to produce a ~1 μm film on top. It has been experimentally verified that this is thick enough to avoid tearing in the film yet thin enough to allow for a smooth, uniform transfer. The chip is cured on a hotplate at 90 °C for 4 minutes. A single holepunch is used to cut out a round hole in a piece of scotch tape; the center of the hole is then overlaid on the center of the spincoated Si chip with the sticky side pressed down to ensure good adhesion. Once again, the tape (along with the PPC film beneath it) is slowly peeled from the chip with the help of a tweezer. The center of the PPC film is finally brought down onto a ~4 mm^2 piece of elastic polydimethylsiloxane (PDMS) sitting atop a glass slide. There should be no bubbles, wrinkles, or tears in the PPC. Both the glass slide and PDMS must be treated with an oxygen plasma beforehand to enhance stickiness. Once a hBN flake of appropriate size and thickness is identified, the glass slide is flipped upside down, affixed to a micromanipulator, and lowered until it contacts the flake at

42 °C until the wavefront has moved beyond the flake. The slide is raised up slowly to prevent any sudden jumps that could result in folds and/or cracks in the hBN. This pickup procedure is repeated as many times as there are layers in the final stack. The transfer procedure, in which the flake/stack is instead placed onto a new substrate, is basically the same, except that the flake/stack contacts the substrate at 30 °C and the PPC overlayer is melted and delaminated from the PDMS by slowly raising the temperature to 85 °C. These procedures are illustrated in Fig. 2.1, reproduced from Ref. [1]. The chip is soaked in acetone overnight and sprayed with IPA to remove PPC residue from its surface.

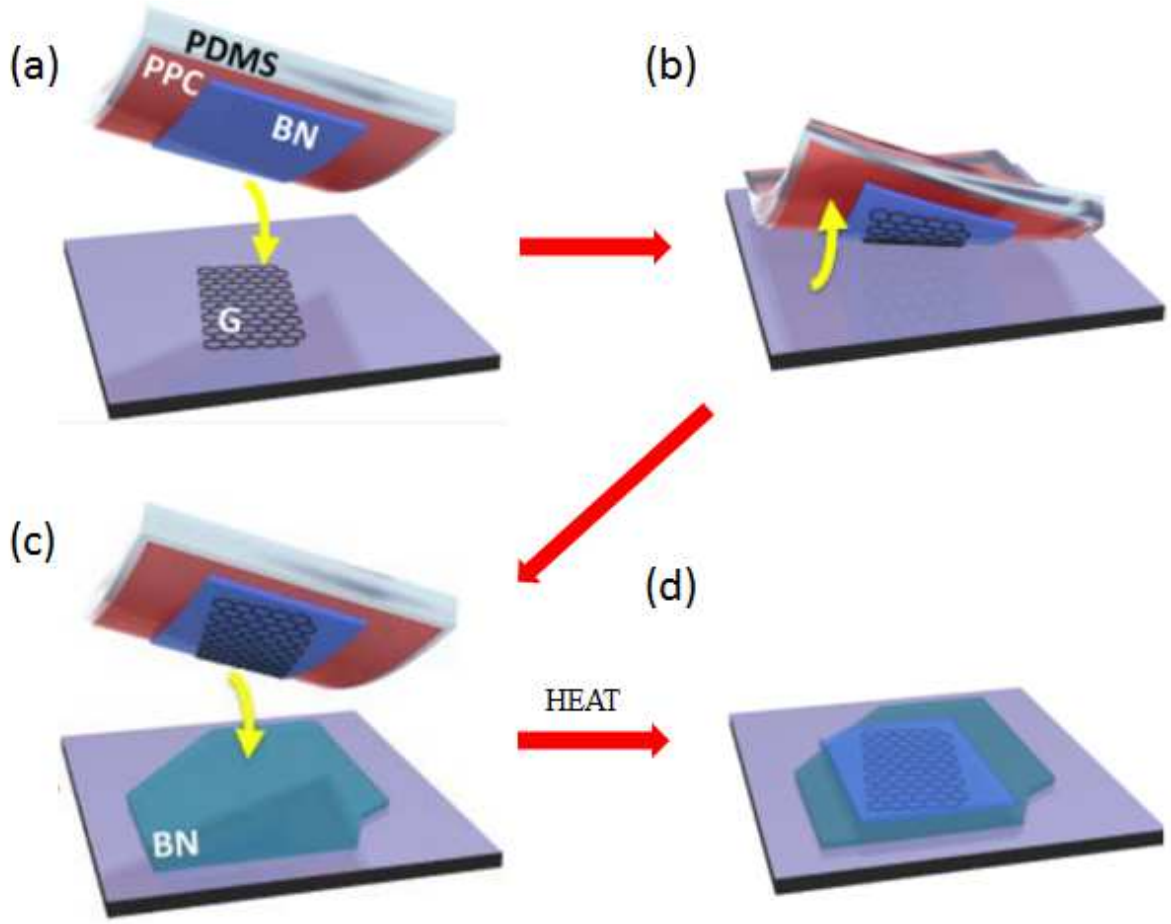

Figure 2.1: Pickup and transfer procedure for the case of simple hBN encapsulation of graphene. A hBN flake that has already been picked up is stamped onto graphene on a SiO_2/Si substrate at 42 °C (a), and the entire stack lifted up at the same temperature (b). For general stacks, (b) can repeated multiple times. The stack is placed in contact with the final substrate in (c), and the temperature gradually increased to 85 °C to allow the PPC to melt and PDMS to delaminate (d). Reproduced from Ref. [2].

2.4 References

1. Wang, L., et al. "One-dimensional electrical contact to a two-dimensional material." *Science* 342.6158 (2013): 614-617.
2. Dean, Cory. "Electron optics in ballistic graphene." INDEX Conference Presentation.

Chapter 3

Raman spectroscopy of encapsulated 1T'-$MoTe_2$ at elevated temperatures

3.1 Motivation

The temperature study of 1T'-$MoTe_2$ in this chapter was motivated by the fact that nearly all transport devices must undergo some form of baking or annealing at elevated temperatures during their fabrication, whether it is to cure a polymer-based resist prior to performing electron beam lithography to pattern electrical contacts, or to burn off sticky polymers such as polypropylene carbonate or propylene carbonate (PPC and PC, respectively) used to assemble heterostructures. While such processing does not pose much of a problem for relatively stable materials like graphene and hBN, it does make a substantial difference for more fragile, oxygen- or moisture-sensitive ones such as 1T'-$MoTe_2$, as any presumably intrinsic material properties deduced from observed phenomena may well be due to unforeseen, irreversible damage caused by heating. For instance, it is common practice to anneal graphene samples under vacuum or in an oxygen-rich or 95/5% argon/hydrogen environment at several hundred °C to minimize any surface contaminants that could adversely affect device performance in terms of sample mobility by introducing scattering centers [1, 2]; this may or may not be appropriate for other materials that could degrade under such conditions. It is shown in this chapter, through Raman spectroscopy, optical microscopy, and atomic force microscopy (AFM), that this is precisely the case for 1T'-$MoTe_2$, where high temperature drives a structural transformation where tellurium escapes from the parent compound at a rate determined by whether or not the sample is well encapsulated.

3.2 Device fabrication

Most of the sample fabrication for this study took place in a nitrogen-filled glovebox to account for the air-sensitive nature of 1T'-$MoTe_2$, which was grown as in Ref. [3]. It was verified that the O_2 and H_2O levels remained below 7 and 0.5 ppm, respectively, at all times. The $MoTe_2$ was micromechanically exfoliated inside the glovebox, and sufficiently thin flakes were located with the help of an x-y scanner (called an autofinder) and encapsulated by hBN as detailed in the previous chapter. Only after encapsulation were the samples removed from the glovebox and soaked in acetone/sprayed with IPA. All measurements described below were taken outside the glovebox, and the samples were stored in a vacuum desiccator in between runs (when not in use) for optimal protection.

3.3 Experiment overview

Overall, the experiment looked at three $MoTe_2$ samples over three runs, where the samples differed in geometry, thickness, uniformity, and coverage by the hBN overlayer, and the runs differed in environmental conditions and temperature range. Sample 1 consisted of a 9 nm thick (~6 unit cells) 1T'-$MoTe_2$ flake covered by a 13 nm thick (~40 layers) hBN flake. Samples 2 and 3 were on a separate chip. Sample 2 consisted of a 4-5 nm (~3 unit cells) 1T'-$MoTe_2$ flake covered by a 10 nm thick (~35 layers) hBN flake, while sample 3 consisted of a 4 nm (~3 unit cells) 1T'-$MoTe_2$ flake covered by a 5 nm thick (~16 layers) hBN flake. 50 optical micrographs of these samples and their vicinity are shown in Fig. 3.1; the contrast was enhanced by 40% to distinguish between different $MoTe_2$ thicknesses, and outlines and arrows have been added to indicate the hBN boundary and where exactly we probed (the thinnest region, whose thicknesses are listed above and in Table 3.1), respectively. These images were taken with a long-working-

Sample Number	$MoTe_2$ Flake Properties
Sample 1 (on first chip)	9 nm (~6 unit cells) covered by 13 nm (~40 layers) hBN
Sample 2 (on second chip)	4-5 nm (~3 unit cells) covered by 10 nm (~35 layers) hBN
Sample 3 (on second chip)	4 nm (~3 unit cells) covered by 5 nm (~16 layers) hBN

Table 3.1: $MoTe_2$ flake properties for each sample.

distance objective while the samples sat in a THMS600 Linkam cell whose stage temperature was adjusted between room temperature and 600 °C. This was also how the Stokes Raman spectra were acquired. An argon-ion laser with a wavelength of 514.5 nm was used for the Raman scattering. The beam had an intensity of 200-300 μW at the sample (after passing through the glass Linkam cell window) and a spot size roughly 1 μW in diameter. It was found that an acquisition time of 120 seconds yielded a signal strong enough to distinguish it from residual background noise, so this was used throughout.

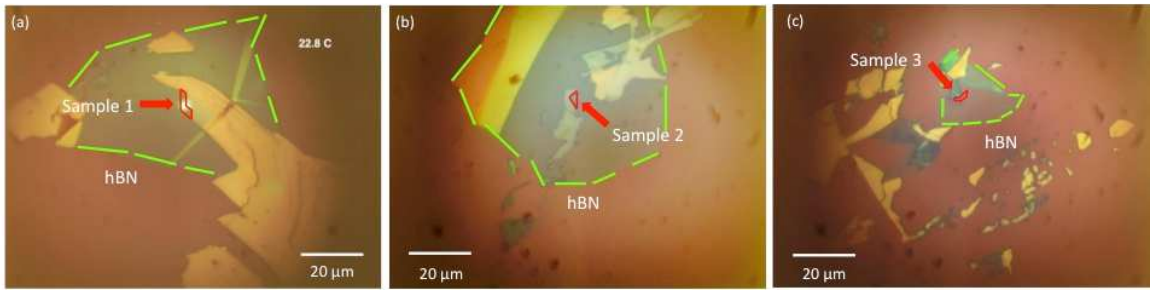

Figure 3.1: Optical micrographs of (a) Sample 1, (b) Sample 2, and (c) Sample 3, at room temperature, before heating. Red outlines denote the thinnest region of the flake, which is probed by Raman scattering, and green outlines denote the edges of the encapsulating hBN.

As can be seen in Fig. 3.1, the hBN overlayers in Samples 1 and 3 did not provide complete coverage of the underlying $MoTe_2$ whereas the hBN overlayer in Sample 2 did, i.e., the probed areas in Samples 1 and 3 were adjoined to thicker $MoTe_2$ flakes that extended beyond the hBN boundary. This fact is crucial to understanding why the Raman spectra in different runs for

different samples varied so drastically, as well as why Sample 2 survived more thermal cycling than the others, as will be discussed later on.

3.4 Heating in air

Run 1, performed on Sample 1, consisted of a temperature ramp in ambient air from 50 to 500 °C in 50 °C increments. There was a 2 minute wait at each temperature setpoint for the temperature to stabilize before commencing with Raman measurements. The $MoTe_2$ started degrading at ~300 °C and then disappearing altogether shortly thereafter in unencapsulated regions and ~400 °C in encapsulated regions based on our observations from optical microscopy.

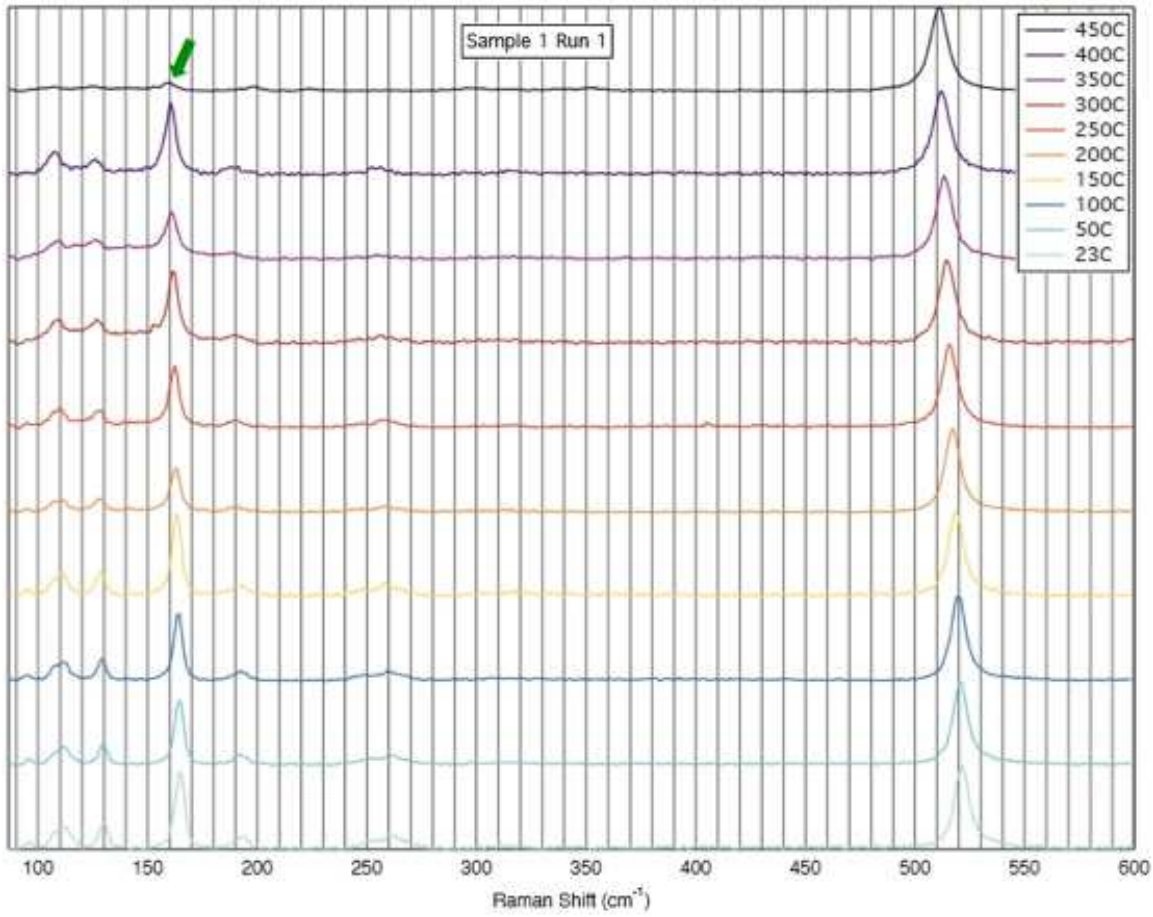

Figure 3.2: Raman spectra of encapsulated 1T'-$MoTe_2$ at various temperatures for Sample 1, Run 1 (in air). The green arrow points to position of the strongest initial $MoTe_2$ peak at room temperature, ~164 cm^{-1}.

Optically, the degradation, as evidenced by the flake's significant change in color, started in uncovered regions of the $MoTe_2$ flake and moved inwards towards covered regions. The Raman measurements confirmed this: a total of six to eight Raman peaks attributable to 1T'-$MoTe_2$ were present between ~96 to 253 cm^{-1} (not including the 520 cm^{-1} Si peak) [4, 5] near the beginning of Run 1, but they essentially vanished by 450 °C (Fig. 3.2). As such, it was not possible to repeat measurements at the same temperatures while cooling the sample back down.

3.5 Heating in argon

Given the degradation observed in Sample 1, Samples 2 and 3 were fabricated and measured in such a way as to further elucidate the mechanism by which it occurred, attempt to delay its onset through varied hBN coverage, and acquire a more detailed and controlled set of temperature-

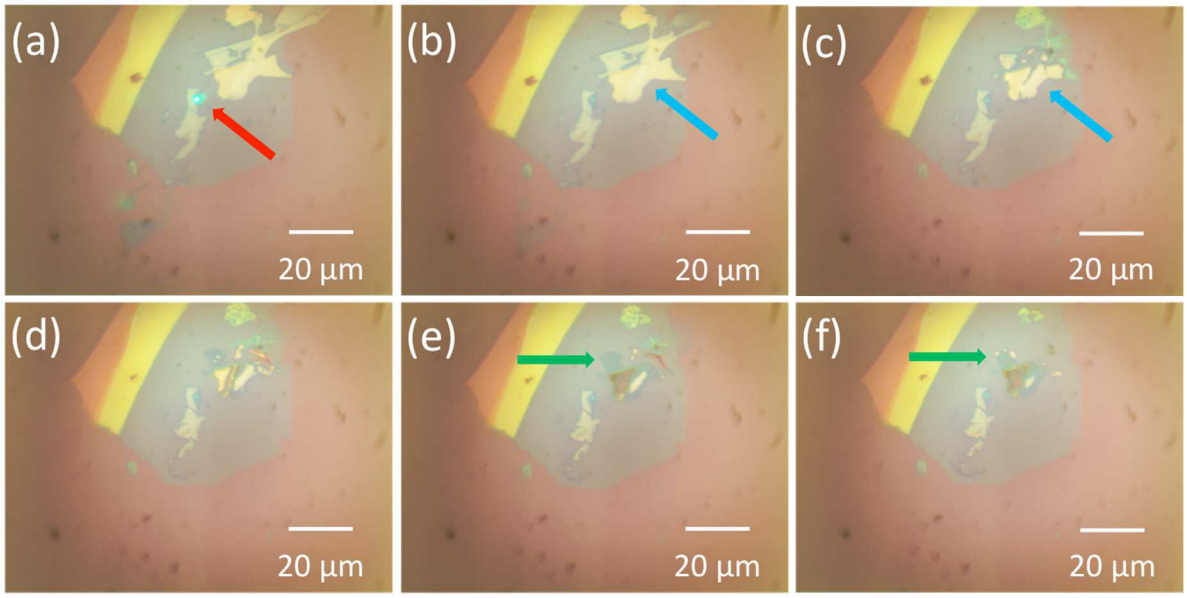

Figure 3.3: Optical micrographs of Sample 2 and nearby $MoTe_2$ flakes, during Run 3: (a) at T_{room} at the beginning of the run, and then after being heated to (b) 325 °C, (c) 475 °C, (d) 550 °C, (e) 575 °C, and (f) 600 °C and then cooled to 100 °C. The red arrow in (a) points to the thinnest region in Sample 2, where it was probed by Raman scattering. The blue arrows in (b) and (c) identify large regions in the flake above and to the right of Sample 2, when this covered part of $MoTe_2$ starts to disappear. The green arrows in (e) and (f) show further decomposition and the lateral movement of parts of that flake.

dependent Raman data using finer temperature steps up to higher temperatures, all under an Ar flow (1 atm, 5 sccm). These two samples were located on the same chip and underwent the same thermal cycling in Runs 2 and 3, with Raman measurements alternating between one sample and the other at each temperature setpoint. Following fabrication, the samples were stored in a vacuum desiccator for five days prior to Run 2. Sample 2 (both the probed area and the thicker regions adjoining it) was completely covered by the hBN overlayer whereas Sample 3 featured incomplete coverage; a visual comparison can be made from Figs. 3.1 and 3.3. Run 2 consisted of heating the samples from room temperature to 50 °C, then up to 300 °C in 50 °C increments, and cooling them back down the same way. Run 3 took place five days after Run 2; once again, the samples were stored in a vacuum desiccator during that intermediary time period. Run 3 featured Samples 2 and 3 being heated and measured at room temperature, 100, 200, and 300 °C (repeating the temperature range of Run 2) before going up to 600 °C in 25 °C increments with "control" measurements interspersed between temperature ramps. These control measurements took place at 100 °C because there was no obvious sign of $MoTe_2$ degradation at that temperature in Run 2; thus they could be used to pinpoint when irreversible damage had occurred in each sample. Note that the images in Fig. 3.1 were taken during these 100 °C stops because images taken at the elevated temperatures immediately preceding them were not as sharp. A summary of the temperature setpoints for all three Runs and Samples can be found in

Sample and Run Number	Gas	Temperature Heating Sequence
Sample 1, Run 1	Ambient air	23, 50, 100, 150, 200, 250, 300, 350, 400, 450 °C
Sample 2, Run 2	Ar flow	25, 50, 100, 150, 200, 250, 300, 250, 200, 150, 100, 50, 25 °C
Sample 2, Run 3	Ar flow	25, 100, 200, 300, 100, 325, 100, 350, 100, …, 600, 100 °C
Sample 3, Run 2	Ar flow	25, 50, 100, 150, 200, 250, 300, 250, 200, 150, 100, 50, 25 °C
Sample 3, Run 3	Ar flow	24.2, 100, 200, 300, 100, 325, 100, 350, 100, 375, 100, 400, 100, 425 °C

Table 3.2: Experimental conditions for each sample/run.

Table 3.2. AFM was done on Sample 2 and its surrounding regions after Run 3 to examine what happened to the parent compound after it had degraded.

Experimentally, it was challenging to keep the laser beam focused on a single spot over the course of each 2-minute measurement due to thermal expansion of the sample. To combat this, the wait time at each temperature setpoint was increased to 5-10 minutes in Run 3, and the beam position and focus more closely tracked with the aid of additional neutral density filters along the beam path before and after the measurements took place. Any measurement where the

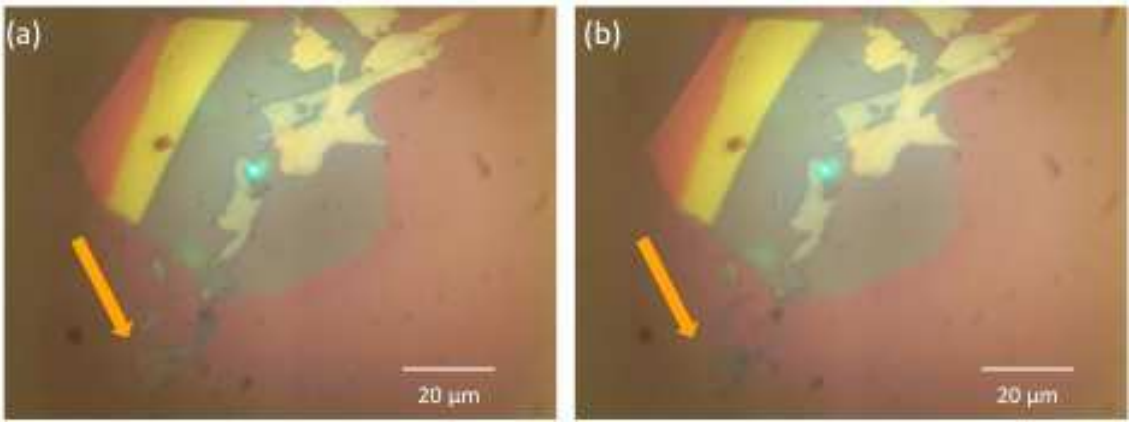

Figure 3.4: Optical micrographs of Sample 2 during Run 2 at (a) 250 °C and (b) 300 °C. The orange arrows indicate the decomposition of small, uncovered flakes under and to the left of the sample in this temperature range.

beam spot had shifted laterally or defocused was retaken.

Optical micrographs of Sample 2 in Figs. 3.3 and 3.4 reveal how different regions of $MoTe_2$, either covered or uncovered, reacted to heat. Figure 3.3a shows Sample 2 in its entirety as well as which area was probed by Raman prior to Run 3; the latter is denoted by a red arrow. No significant changes in covered regions were observed up to 300 °C in Run 2 and ~550 °C in Run 3 (as seen in Fig. 3.3d). Above 550 °C, Sample 2 showed some signs of slight shrinkage and discoloration, though the majority of it remained visually intact up to 600 °C (Fig. 3.3f). The same was not true for uncovered regions, however: Figure 3.4 clearly shows the disappearance of

small, uncovered flakes at the bottom left of the images between 200-300 °C (Run 2) while Figs. 3.3b, c detail the degradation of partially covered flakes between 300-350 °C (Run 3). Sample 3 also suffered from discoloration and shrinkage above 350 °C (Fig. 3.5), becoming so severe above 400 °C that the Raman peaks became nearly invisible and it did not make sense to continue measuring above this temperature. Photodegradation was not observed at the end of the runs despite its endurance of ~80 minutes of integrated irradiation.

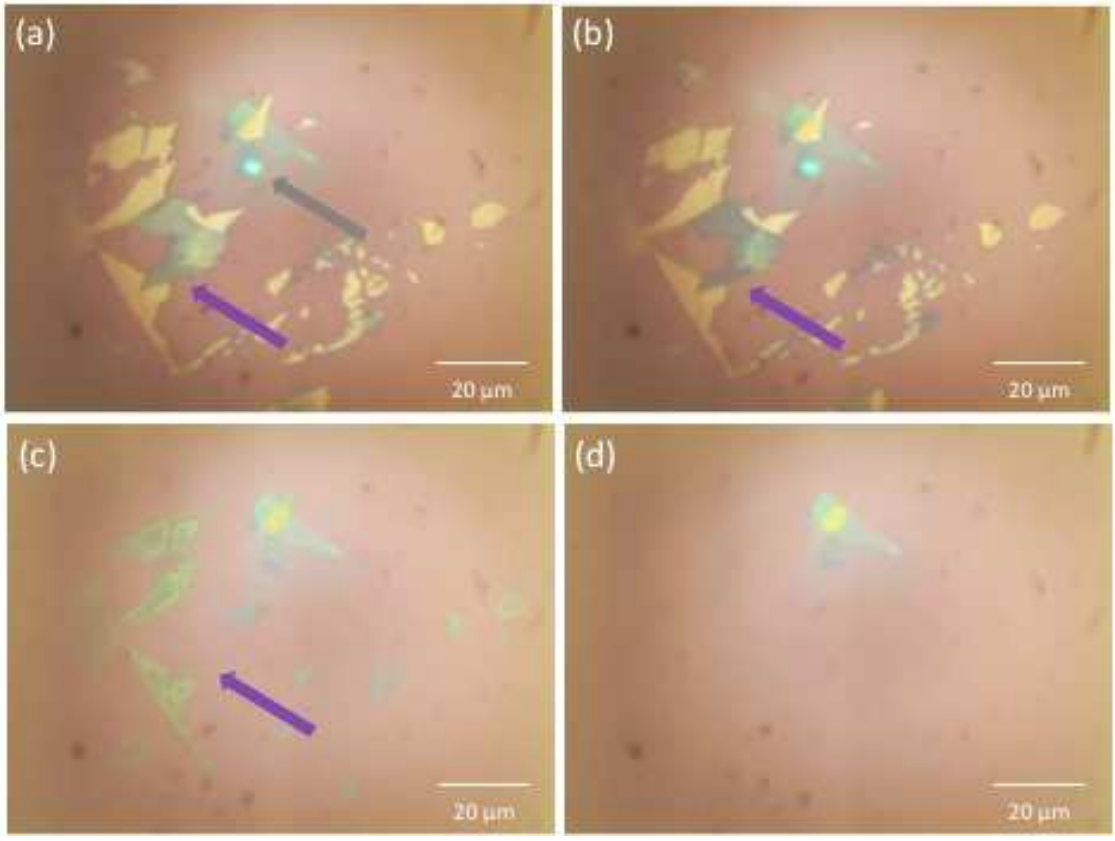

Figure 3.5: Optical micrographs of Sample 3, Run 2 at (a) 250 °C, (b) 300 °C, and then after (c) 375 °C and (d) 400 °C, both taken at 100 °C. The gray arrow in (a) indicates where the sample was probed at all temperatures while the purple arrows in (a), (b), and (c) show the decomposition of small, uncovered flakes below and to the left of the sample, which is complete in (d).

3.6 Peak analysis and formation of tellurium

Figures 3.6 and 3.7 show representative Raman spectra of the thinnest covered region of Sample 2 in Runs 2 and 3, respectively. $MoTe_2$ peaks and their mode assignments (in parentheses, based on previous studies) are shown to reside at 112 (A_g) [5], 128 (A_g) [5, 6], 164 [(A_g) [6] or (B_g) [5]], 191 (B_g) [5], and 253 cm^{-1} (A_g) [5, 6] at room temperature, where the 520 cm^{-1} Si peak and peaks with energies below 112 cm^{-1} (specifically the ones at 96 and 106 cm^{-1}) have been omitted, the latter being too close to the cutoff wavelength of the edge filter to analyze quantitatively [7]. Samples 1 and 3 showed peaks at comparable locations (Figs. 3.2 and 3.8) but different relative peak areas for the 164 and 128 cm^{-1} peaks; this ratio was ~6, 3, and 1 in Samples 1, 2, and 3, respectively.

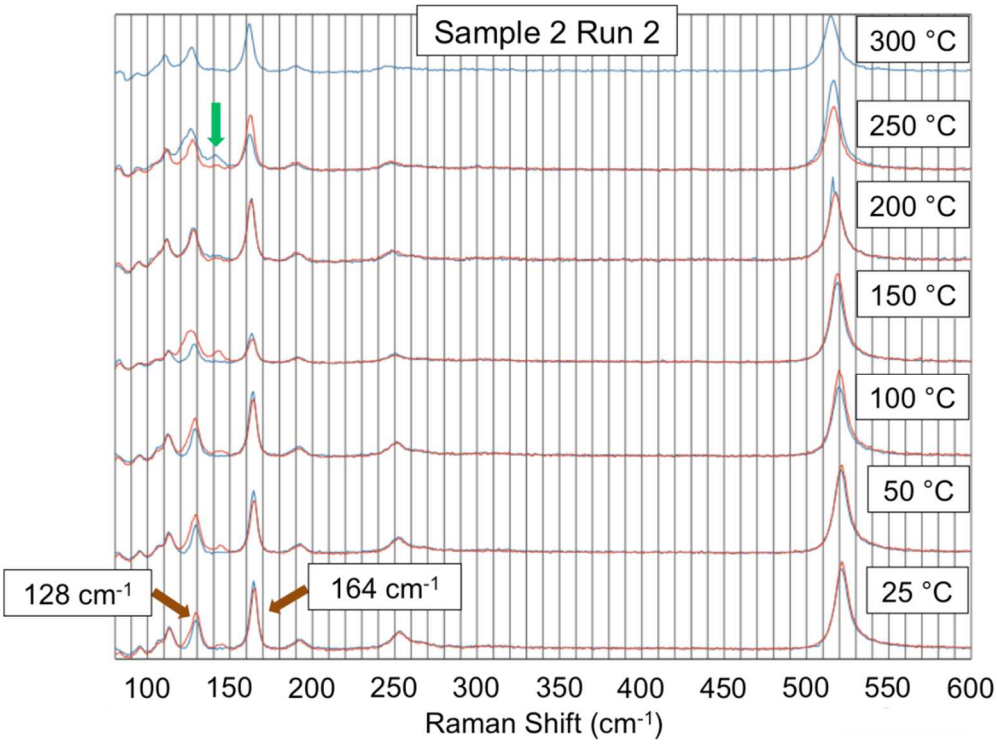

Figure 3.6: Raman spectra of encapsulated 1T'-$MoTe_2$ at various temperatures (Sample 2, Run 2) under Ar flow. The blue and red spectra were acquired during the temperature ramp up and down, respectively. The brown arrows point to the two largest $MoTe_2$ peaks and the green arrow shows the emergence of a tellurium peak ~143 cm^{-1} at higher temperatures.

The aforementioned $MoTe_2$ Raman peaks changed in position, intensity, and integrated area with temperature; the following discussion focuses on the largest peaks as well as the emergence and subsequent disappearance of a couple others. All of the $MoTe_2$ peak intensities became greatly weakened above 550 °C in Run 3, which is consistent with the degradation observed from optical microscopy. Of particular interest is the peak near 143 cm^{-1} that emerged

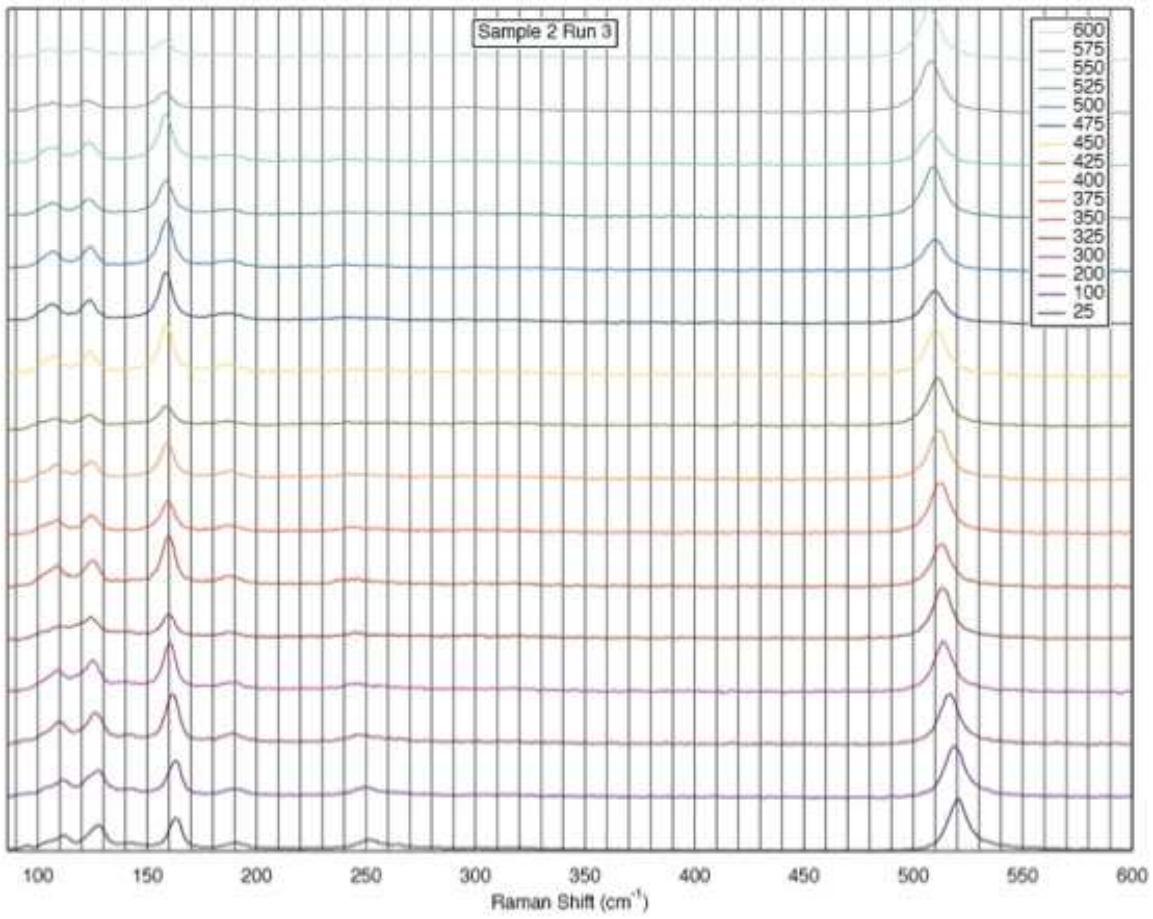

Figure 3.7: Raman spectra of encapsulated 1T'-$MoTe_2$ at various temperatures for Sample 2, Run 3 (Ar flow).

in Sample 2 during Run 2 (Fig. 3.6) and persisted up to ~300 °C in Run 3 (Fig. 3.7). It was also one of two peaks found in Sample 3 during Run 2 (Fig. 3.8), the other being an even more prominent peak at ~123 cm^{-1}; both peaks have been attributed to the formation of Te and reveal

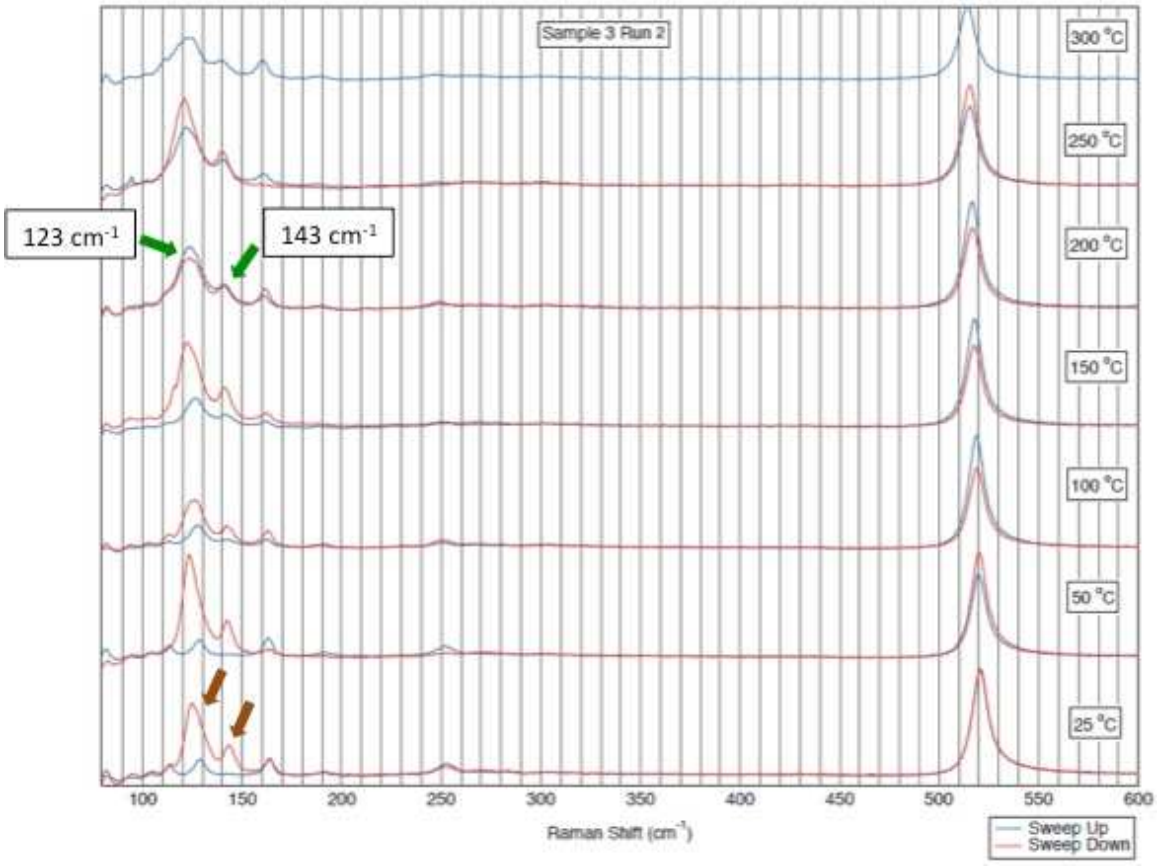

Figure 3.8: Raman spectra of encapsulated 1T'-$MoTe_2$ at various temperatures for Sample 3, Run 2 (Ar flow)

clues about the fate of the decomposed parent compound. The relative strengths of the 123 and 143 cm^{-1} peaks remained fairly constant across various temperatures in Sample 3. They were first observed between 100-150 °C in Sample 3 during Run 2, with the 123 cm^{-1} peak surpassing

the 128 cm^{-1} peak at around 200 °C; they persisted up to 300 °C and during the temperature cooldown to 25 °C. The Raman spectrum of Sample 3 at the beginning of Run 3 matched the spectrum at the end of Run 2, not changing much during the temperature ramp up to ~350-400 °C (Fig. 3.9). All Raman peaks found in Sample 3 had become substantially weakened by 425 °C, the last temperature at which it was probed. The 123 cm^{-1} peak was not strong enough in

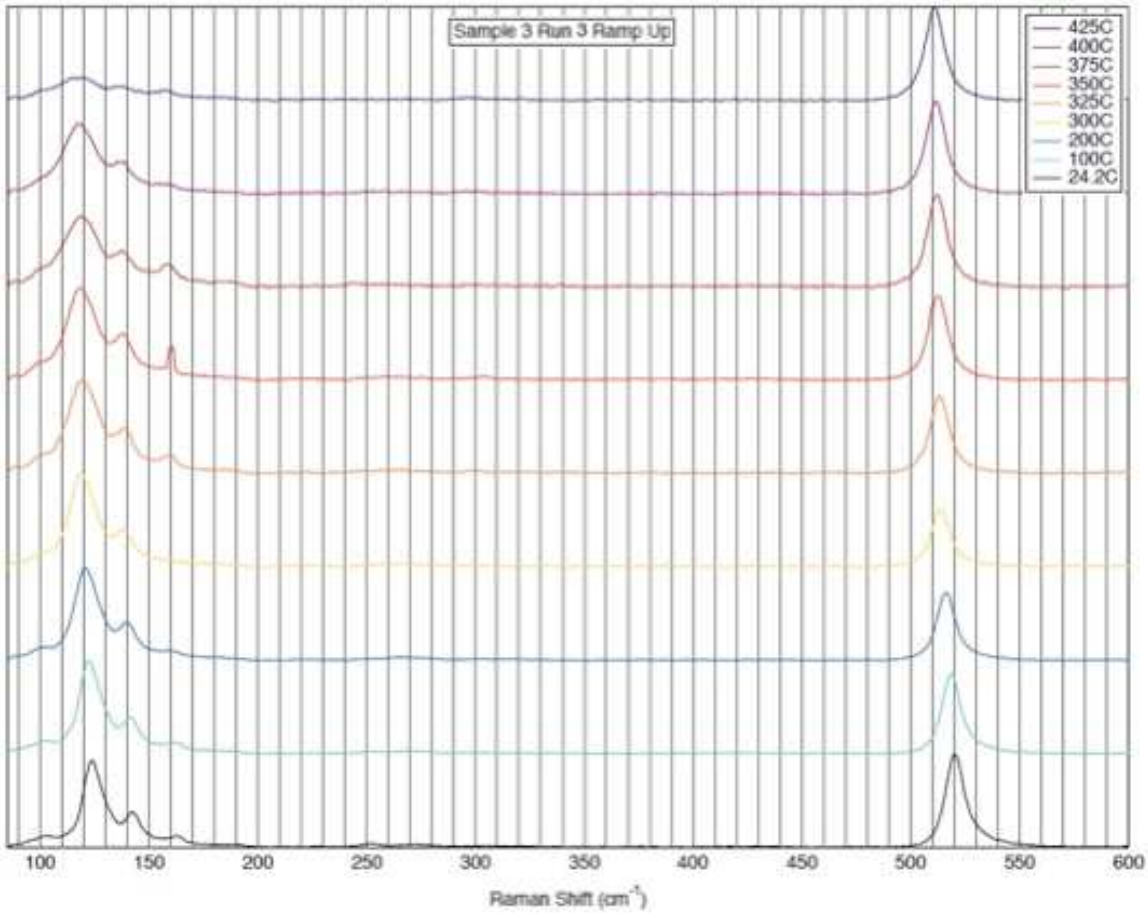

Figure 3.9: Raman spectra of encapsulated 1T'-$MoTe_2$ at various temperatures for Sample 3, Run 3 (Ar flow). No $MoTe_2$ Raman signal was observed at and above 450 °C.

Sample 2 to be observed independently, though it was likely responsible for the asymmetry of the 128 cm^{-1} peak in Fig. 3.6. Neither of the two Te peaks were found in Run 1 for Sample 1, which had undergone heating in air rather than Ar.

A comparison to previous Raman studies of different forms of Te helps classify these peaks: it is known that bulk trigonal Te possesses A_1 and E_{TO} peaks at 120.4 and 140.7 cm^{-1} at 298 K, whereas amorphous Te has peaks at ~121 and 146 cm^{-1}. [7] Nanoplates and nanorods of Te, on the other hand, have peaks located at ~115.4 and 134.3 cm^{-1} [8], much lower in energy than the 123 and 143 cm^{-1} peaks seen in Sample 3. Thus position-wise, the Te peaks in Sample 3 more closely matched those of crystalline and amorphous Te. Crystalline and amorphous Te, however, differ in the ratio of their peak heights (lower energy to higher energy), with the former ~3 to 1 (with linearly polarized incident and unpolarized detected light) and the latter ~4 to 3. [7] Given the similar peak intensity ratios under an identical experimental setup, the Te peaks in Sample 3 were likely crystalline in nature. The same conclusions are drawn when comparing peak areas.

Besides the appearance of Te peaks, the Raman spectra at the beginning and end of Run 2 for Samples 2 and 3 were more or less identical, and any irreversible changes that did occur in Run 3 could also be observed in the corresponding optical micrographs. For instance, the 1T'-$MoTe_2$ peak at ~164 cm^{-1} moved by no more than 0.5 cm^{-1} from its original position after the first round of thermal cycling in Run 2; the same could be said for all other $MoTe_2$ peak frequencies in the 100 °C "control" measurements between temperature steps in Run 3 after calibrating the spectra using the known peak position of Si. Likewise, Samples 2 and 3 experienced no noticeable degradation between the end of Run 2 and the beginning of Run 3 as proved by their matching Raman spectra. Analyzing the difference in $MoTe_2$ peak areas of the thinnest, probed region of Sample 2 reveals that its thickness varied by far less than a monolayer, at least until the optical micrographs suggested otherwise.

The most striking feature of the Raman spectra of Sample 3 is how the Te Raman peaks overshadow even the largest of the initial $MoTe_2$ peaks, a consequence of the former's larger cross section (despite a limited, sub-monolayer thickness) rather than an overwhelming abundance of Te as compared to $MoTe_2$. By contrast, the Te peaks in Sample 2 were not nearly as outstanding and suggest more modest decomposition.

Other products of $MoTe_2$ decomposition were ruled out in both runs conducted in air (Run 1) and argon environments that could contain trace amounts of air (Runs 2 and 3). Namely, none of the characteristic oxide (whether crystalline or polycrystalline) peaks associated with Te or Mo were present, as MoO_2 has peaks at 360, 510, 575, and 748 cm^{-1} [9], MoO_3 (in its powder form) has peaks at 158, 285, 666, 820, and 995 cm^{-1} [10], and TeO_2 has peaks at 426 and 611 cm^{-1} [11]. Nor was there evidence that the 1T'-$MoTe_2$ had undergone a phase transformation into 2H-$MoTe_2$ at any point, though Ref. [12] suggests a transformation in the opposite direction at 400 °C.

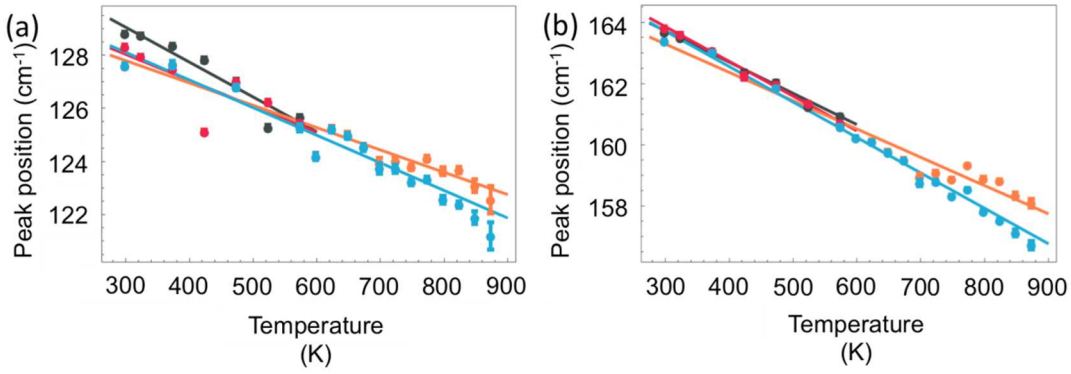

Figure 3.10: Raman shifts versus temperature of the two largest Raman peaks, (a) ~128 cm^{-1} and (b) ~164 cm^{-1}, of the covered 1T'-$MoTe_2$ Sample 2 during the up (red) and down (black) ramps of Run 2 and the up ramp of Run 3 (orange), including linear fits vs. temperature for each. The data for Run 3 are also shown recalibrated to the Si Raman peak (blue).

Fits of frequency vs. temperature for two 1T'-$MoTe_2$ Raman peaks, for Sample 2

128 cm^{-1} peak

- Run 2 Up: 132.97 (± 0.14) cm^{-1} – [0.013097 (± 0.000321) cm^{-1}/K] T(K)
- Run 2 Down: 130.96 (± 0.13) cm^{-1} – [0.009780 (± 0.000314) cm^{-1}/K] T(K)
- Run 3 Up: 130.31 (± 0.12) cm^{-1} – [0.008400 (± 0.000190) cm^{-1}/K] T(K)
- Run 3 Up, Calibrated: 131.22 (± 0.12) cm^{-1} – [0.010388 (± 0.000190) cm^{-1}/K] T(K)
- Unweighted Average of [Run 2 Up/Down and Run 3 Up, Calibrated]: 131.72 (± 0.13) cm^{-1} – [0.011088 (± 0.000282) cm^{-1}/K] T(K)
- Weighted Average of [Run 2 Up/Down and Run 3 Up, Calibrated]: 131.59 (± 0.13) cm^{-1} – [0.010916 (± 0.000255) cm^{-1}/K] T(K)
- Direct fit of [Run 2 Up/Down and Run 3 Up, Calibrated]: 131.81 (± 0.08) cm^{-1} – [0.0112249 (± 0.000143) cm^{-1}/K] T(K)

164 cm^{-1} peak

- Run 2 Up: 166.78 (± 0.06) cm^{-1} – [0.010200 (± 0.000143) cm^{-1}/K] T(K)
- Run 2 Down: 167.26 (± 0.07) cm^{-1} – [0.011337 (± 0.000148) cm^{-1}/K] T(K)
- Run 3 Up: 166.07 (± 0.058) cm^{-1} – [0.009249 (± 0.000089) cm^{-1}/K] T(K)
- Run 3 Up, Calibrated: 167.19 (± 0.06) cm^{-1} – [0.011581 (± 0.000089) cm^{-1}/K] T(K)
- Unweighted Average of [Run 2 Up/Down and Run 3 Up, Calibrated]: 167.08 (± 0.06) cm^{-1} – [0.011039 (± 0.000525) cm^{-1}/K] T(K)
- Weighted Average of [Run 2 Up/Down and Run 3 Up, Calibrated]: 167.11 (± 0.06) cm^{-1} – [0.011197 (± 0.000665) cm^{-1}/K] T(K)
- Direct fit of [Run 2 Up/Down and Run 3 Up, Calibrated]: 167.50 (± 0.04 cm^{-1}) – [0.011842 (± 0.000066) cm^{-1}/K] T(K)

Table 3.3: Fits of frequency vs. temperature for two 1T'-$MoTe_2$ Raman peaks, for Sample 2.

Higher temperatures led to $MoTe_2$ peak Raman shifts toward lower frequencies, as expected, for all samples and runs, regardless of whether it was during a temperature ramp up or cooldown. The $MoTe_2$ peaks also experienced the expected broadening at high temperatures, though this was difficult to monitor precisely because many of them were small and overlapped with each other. Plots of peak position versus temperature for the two largest Raman peaks of Sample 2, near 128 cm^{-1} and 164 cm^{-1}, are shown in Fig. 3.10 for the heating/cooling phases of Run 2 and the heating phase of Run 3. Both the raw data and the data calibrated at 100 °C using

Si are plotted for Run 3. Such trends were representative of all $MoTe_2$ peaks, though other $MoTe_2$ peak positions could not be resolved as clearly because of their lower intensity or proximity to Te peaks. Also shown in Fig. 3.10 are linear fits of frequency versus temperature; linear fits in this temperature range are expected and match well with the data (see Table 3.3) according to the three-phonon coupling model and thermal expansion. As described in Ref. [13], the zonecenter optical phonon frequencies ω_p generally decrease with temperature T and depend on ω_0, the harmonic frequency of the optical mode, $\Delta^{(1)}(T)$, the contribution from thermal expansion, and $\Delta^{(2)}(T)$, the contribution from phonon-phonon coupling. $\Delta^{(1)}(T)$ in turn depends on $\alpha(T)$, the coefficient of linear thermal expansion, and γ_G, equal to $-d(\ln\omega_p)/d(\ln V)$ (where V denotes volume). $\Delta^{(2)}(T)$ includes both coupling between the optical phonon and two lower-energy phonons (three-phonon coupling) and higher-order processes, denoted by the first and second brackets, respectively:

$$\omega_p(T) = \omega_0 + \Delta^{(1)}(T) + \Delta^{(2)}(T)$$

$$\Delta^{(1)}(T) = \omega_0 \left[\exp\left\{ -3\gamma_G \int_0^T \alpha(T')dT' \right\} - 1 \right]$$

$$\Delta^{(2)}(T) = A_1 \left\{ 1 + \sum_{j=1}^{2} \frac{1}{e^{x_j} - 1} \right\} + A_2 \left\{ 1 + \sum_{k=1}^{3} \left(\frac{1}{e^{y_k} - 1} + \frac{1}{(e^{y_k} - 1)^2} \right) \right\}$$

The x_j's and y_k's appearing in $\Delta^{(2)}(T)$ are related by $x_1 + x_2 = y_1 + y_2 + y_3 = \hbar\omega_0/k_BT$. Taking the limit as $k_BT \gg \hbar\omega_0$ yields linear contributions in T from $\Delta^{(1)}(T)$ and the first term of $\Delta^{(2)}(T)$, and quadratic contributions in T from the second term of $\Delta^{(2)}(T)$ (not observed here):

$$\omega_p(T) \approx \omega_0 + aT + bT^2$$

The slopes for the two peaks are comparable. Averaging the fits for the calibrated data for Run 3 with the heating/cooling phases of Run 2 yields an overall fit of 131.72 (±0.13) cm^{-1} – [0.011088

(±0.000282) cm^{-1} K^{-1}]T(K) for the 128 cm^{-1} peak and 167.08 (±0.06) cm^{-1} –[0.011039 (±0.000525) cm^{-1} K^{-1}]T(K) for the 164 cm^{-1} peak. Besides variations arising from errors in the peak fits, there could be a number of factors responsible for the error bars here, including different $MoTe_2$ thicknesses, varied strain due to adhesion to the substrate and/or hBN overlayer, and nonuniform thermal contraction in the cooldown ramps (which in turn depends on the mode, layer number, relative thermal expansion coefficients of the substrate and $MoTe_2$ layer, and the flake's adherence to the substrate during thermal cycling).

3.7 Atomic force microscopy

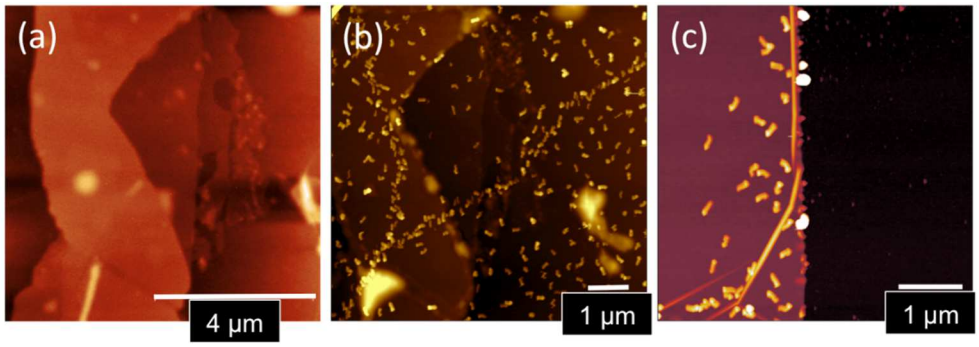

Figure 3.11: *ex situ* AFM traces of the probed region of Sample 2 at room temperature (a) before and (b) after all of the heating and cooling cycles of Runs 2 and 3, showing the presence of nanoparticles, presumably composed of Te, under the hBN. The region probed during Raman scattering is in the triangular area, outlined in red, in Fig. 3.1(b), where Sample 2 is thinnest. (c) Shows the rightmost edge of the hBN on Sample 2, after these runs; no nanoparticles are observed outside the boundaries of the hBN.

Ex situ AFM scans of Sample 2 are shown in Fig. 3.11 before the initiation of Run 2 (a) and after the completion of Run 3 (b and c). The scans in Figs. 3.11a, b focused on the thinnest area probed by Raman (see triangular region outlined in green in Fig. 3.1b), while the scan in Fig. 3.11c was taken at the rightmost edge of the hBN overlayer. Nanoparticles, presumably

composed of Te, are present in Figs. 3.11b, c but not Fig. 3.11a, indicating that they emerged from the original $MoTe_2$ compound as a result of heating the latter up to temperatures as high as 600 °C. The relatively sparse concentration of nanoparticles in Fig. 3.11c compared to Fig. 3.11b, coupled with their proximity to narrow elevated regions of the hBN (shown by the sharp yellow lines in Fig. 3.11c), suggest that the nanoparticles (and any other products of $MoTe_2$ decomposition by heating) migrated away from the parent compound towards the edge of their encapsulating layer through folds or wrinkles. They were subsequently carried away by the flow of argon gas, as suggested by the lack of nanoparticles in the right half of Fig. 3.11c. Such transport beneath the hBN and across the surface of the substrate is reasonable given that Te has a vapor pressure of 100 Pa (0.75 Torr) at 775 K and 1000 Pa (7.5 Torr) at 888 K [14], though its importance at lower temperatures is not clear.

The stability of the samples relative to each other can be deduced from their Raman spectra and/or optical micrographs. Sample 1, which was adjoined to larger and thicker $MoTe_2$ flakes protruding from beneath the hBN and heated in air rather than Ar, was clearly the least stable of the three. While both Samples 2 and 3 were heated in Ar, the former was likely more stable than the latter at identical temperatures because it was covered on all sides by hBN, being completely detached from any $MoTe_2$ flakes that extended beyond the edge of the hBN. The thickness of the hBN layers did not matter given that both were multilayers.

3.8 Degradation pathways

How quickly the $MoTe_2$ decomposes and is transported away from its original site could depend on how much of it is covered by hBN (once again considering any adjoining flakes) and how well the hBN conforms to its surface given its nonuniform thickness. A $MoTe_2$ flake covered by

hBN that conforms well to its local topography could decompose at a slower rate; likewise, any products of heating could be transported away more slowly as well due to the reduced number of available pathways outside the hBN. The delayed transport could also give rise to slower decomposition because the products, left with nowhere to go, remain at the $MoTe_2$ surface and prevent more of it from decomposing. Figures 3.11b, c show that transport of products beneath the hBN occurred at least around 600 °C. Although transport may also have occurred at lower temperatures, the main findings would still hold true.

Sample 2 would decompose uniformly if the decomposition were insensitive to the local thickness of the $MoTe_2$ and if the conformal coverage of the hBN were identical everywhere. Thus although the $MoTe_2$ would decompose into Te at the same rate everywhere, the amount of Te detected by Raman scattering at any given location would depend on how easily it could be transported away from that site. This, however, does not affect the thickness of the $MoTe_2$/Te overlayer below around 550 °C based on the Raman spectra; the fact that the Si substrate produces a large peak proves that the sample is optically thin, and the thickness of optically thin samples should scale with their Raman peak area (neglecting resonance effects). Assuming the Raman susceptibility does not change much with temperature, a higher temperature would lead to increased Stokes scattering rates due to phonon populations. In addition to transport, it is possible that at moderate temperatures $MoTe_{2-x}$ in its solid form recombines with Te in its gaseous form (the vapor pressure of Te being relatively high) to reproduce solid $MoTe_2$ through a reverse sublimation process, $MoTe_{2-x}(s) + xTe(g) = MoTe_2(s)$, diminishing the observed Te Raman signal under these conditions.

There could be several reasons for the smaller Te Raman signal in Sample 2 than in Sample 3. For instance, the decomposition in the probed region of Sample 2 could be slower to

begin with. Another possibility is that the decomposition products there were removed at a faster rate than in Sample 3 although the decomposition rates of the two samples were similar. A third explanation is that Sample 2 decomposed more quickly away from this site but the products of heating were transported to it more slowly because of better coverage by the hBN locally or elsewhere on the flake. The diminished Te signal in Sample 2 from 300 to 250 °C during the temperature ramp down in Run 2 may highlight the importance of transport away from the site, while the nearly nonexistent Te signal at even higher temperatures in Run 3 suggest that any Te that did form at the site was removed even more quickly. Coupled with the absence of significant changes in the $MoTe_2$ peaks between 300 to 550 °C in Run 3, it can be concluded that Te formed more slowly at lower temperatures because of defects or products of heating remaining at the surface and preventing more of it from being formed.

The passivation of 1T'-$MoTe_2$ (subject to heating) through hBN encapsulation mirrors another study examining the passivation of nanoparticle monolayers (exposed to oxygen-rich environments) through encapsulation by various van der Waals layers [15] in that diffusion in both experiments, whether it was decomposed material leaving the parent compound or outside molecules seeping inwards, occurred through the edges rather than bulk of the overlayer. In both cases, the effectiveness of encapsulation was tied directly to the lateral dimensions of the encapsulating layer, not its thickness.

3.9 Conclusions

Overall, it was demonstrated that complete encapsulation by hBN greatly increases the temperature at which significant decomposition of 1T'-$MoTe_2$ begins, to ~550 °C, compared to partial or no hBN coverage. Still some decomposition products were observed at lower

temperatures. This could affect device processing and performance, but some Te loss from the surface may bode well for electrolytic and hydrodesulfurization applications. [16-18] Improved passivation and passivation even above 550 °C might be expected with improved encapsulation, as may occur for $MoTe_2$ flakes and samples of uniform thickness. Raman scattering and optical microscopy have been shown to be valuable *in situ* tools to evaluate stability.

The contents of this chapter were published as Ref. [19].

3.10 References

1. Dean, Cory R., et al. "Boron nitride substrates for high-quality graphene electronics." *Nature Nanotechnology* 5.10 (2010): 722.
2. Garcia, Andrei GF, et al. "Effective cleaning of hexagonal boron nitride for graphene devices." *Nano Letters* 12.9 (2012): 4449-4454.
3. Rhodes, D., et al. "Engineering the structural and electronic phases of $MoTe_2$ through W substitution." *Nano Letters* 17.3 (2017): 1616-1622.
4. Chen, Shao-Yu, et al. "Intrinsic Phonon Bands in High-Quality Monolayer T′ Molybdenum Ditelluride." *ACS Nano* 11.1 (2016): 814-820.
5. Keum, Dong Hoon, et al. "Bandgap opening in few-layered monoclinic $MoTe_2$." *Nature Physics* 11.6 (2015): 482.
6. Sun, Yifan, et al. "Low-Temperature Solution Synthesis of Few-Layer 1T′-$MoTe_2$ Nanostructures Exhibiting Lattice Compression." *Angewandte Chemie International Edition* 55.8 (2016): 2830-2834.
7. Pine, A. S., and G. Dresselhaus. "Raman spectra and lattice dynamics of tellurium." *Physical Review B* 4.2 (1971): 356.
8. Li, Guihua, et al. "Solvothermal synthesis of polycrystalline tellurium nanoplates and their conversion into single crystalline nanorods." *RSC Advances* 4.2 (2014): 954-958.
9. Smudde Jr, George H., and Peter C. Stair. "The oxidation of Mo (100) studied by XPS and surface Raman spectroscopy: the onset of MoO_2 formation and the formation of surface polymolybdate." *Surface Science* 317.1-2 (1994): 65-72.

10. Windom, Bret C., W. G. Sawyer, and David W. Hahn. "A Raman spectroscopic study of MoS_2 and MoO_3: applications to tribological systems." *Tribology Letters* 42.3 (2011): 301-310.
11. Champarnaud-Mesjard, J. C., et al. "Crystal structure, Raman spectrum and lattice dynamics of a new metastable form of tellurium dioxide: γ-TeO_2." *Journal of Physics and Chemistry of Solids* 61.9 (2000): 1499-1507.
12. Cho, Suyeon, et al. "Phase patterning for ohmic homojunction contact in $MoTe_2$." *Science* 349.6248 (2015): 625-628.
13. Herman, Irving P. "Raman Scattering." *Optical diagnostics for thin film processing*. Elsevier, 1996. 583-584. Print.
14. *CRC Handbook of Chemistry and Physics*, 97th edn, 2016, http://hbcponline.com/faces/documents/06_22/06_22_0075.xhtml?search=true (accessed February 2017)
15. Zhang, Datong, et al. "Passivation of CdSe Quantum Dots by Graphene and MoS_2 Monolayer Encapsulation." *Chemistry of Materials* 27.14 (2015): 5032-5039.
16. Liu, Yuan, et al. "Van der Waals heterostructures and devices." *Nature Reviews Materials* 1.9 (2016): 16042.
17. Lu, Qipeng, et al. "2D Transition-Metal-Dichalcogenide-Nanosheet-Based Composites for Photocatalytic and Electrocatalytic Hydrogen Evolution Reactions." *Advanced Materials* 28.10 (2016): 1917-1933.
18. Chhowalla, Manish, et al. "The chemistry of two-dimensional layered transition metal dichalcogenide nanosheets." *Nature Chemistry* 5.4 (2013): 263.

19. Wang, Dennis, et al. "Passivating 1T′-$MoTe_2$ multilayers at elevated temperatures by encapsulation." *Nanoscale* 9.37 (2017): 13910-13914.

Chapter 4

Nature and electronic tunability of the NC-C phase transition in 1T-TaS_2

4.1 Motivation

1T-TaS_2, a layered compound, is characterized by the presence of multiple distinct phases that differ both structurally and electronically. In its ground state at low temperature and ambient pressure, it is a commensurate (C) charge density wave (CDW). It then becomes, through a series of first-order phase transitions, a nearly commensurate (NC) CDW at 225 K, an incommensurate (IC) CDW at 355 K, and finally a metal at 545 K. The compound undergoes a structural transformation accompanied by changes in its transport signature during each of these transitions. It has been found that tuning various external parameters such as pressure and chemical doping suppresses the CDW phases in 1T-TaS_2 and gives rise to superconductivity [1-3], while thinning down bulk crystals significantly alters its electronic properties [4-6]. This chapter utilizes transmission electron microscopy (TEM) and electronic transport to elucidate the nature of the CDW phases and the transitions between them in the ultrathin limit. Few-layer samples exhibited surface oxidation that led to the disappearance of charge ordering; encapsulated samples, however, retained their CDW phases which could be precisely manipulated by electronic means.

4.2 Structure of 1T-TaS_2

Electron diffraction patterns from TEM of a bulk 1T-TaS_2 sample approximately 50 nm thick are shown in Fig. 4.1a, where bright peaks correspond to Bragg scattering from Ta atoms in a triangular lattice with lattice constant a = 3.36 Å. Other surrounding Ta atoms, shown by weaker diffraction peaks, moved towards these ones at lower temperatures in the C-CDW phase (Fig.

4.1b, blue panel), and their displacement formed Star-of-David clusters consisting of 13 atoms each. The clusters as a whole make up a commensurate superstructure with wavelength $\lambda_C = \sqrt{13}a$; it is tilted at an angle of 13.9° relative to the atomic lattice. The top red panel in Fig. 4.1a shows the same crystal in the NC-CDW phase at room temperature, in which case the distortions are still present but, as demonstrated by previous scanning tunneling microscopy (STM) studies, limited to quasi-hexagonal domains with periodicities ranging from 60-90 Å depending on temperature. [7, 8] The discommensuration network separating these domains forms a Kagome

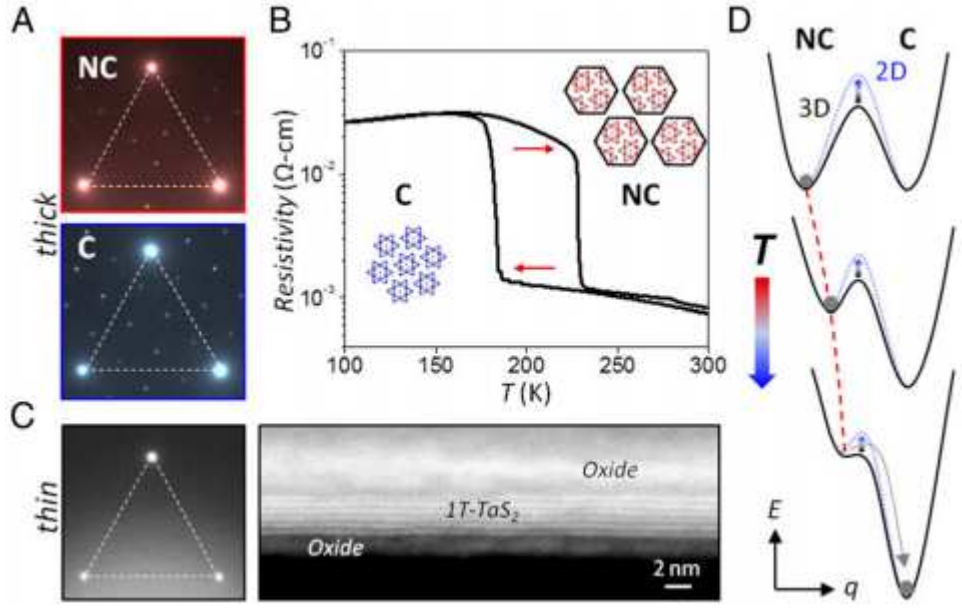

Figure 4.1: NC-C CDW phase transition in bulk 1T-TaS_2 and CDW suppression by oxidation in thin flakes. (a) TEM diffraction images of 50-nm-thick 1T-TaS_2 at 295 K (red, NC phase) and 100 K (blue, C phase). Weaker peaks are due to CDW distortion. (b) Resistivity vs. temperature of bulk 1T-TaS_2 crystal around the first-order, NC-C transition. (*Insets*) Real space schematics of CDW structure. (c) (left) TEM diffraction of few-layer 1T-TaS_2 flake shows absence of CDW order. (right) High-resolution, cross section electron microscopy image reveals presence of amorphous oxide. (d) Free energy schematic of CDW evolution with temperature. Vertical and horizontal axis represent free energy (E) and reaction coordinate (q), respectively. NC domains grow slowly upon cooling until abrupt transition into the C phase. Energy barrier increases in 2-D samples protected from oxidation.

lattice, inside of which the Ta displacements are substantially reduced. [9] This is illustrated schematically in the red inset of Fig. 4.1b.

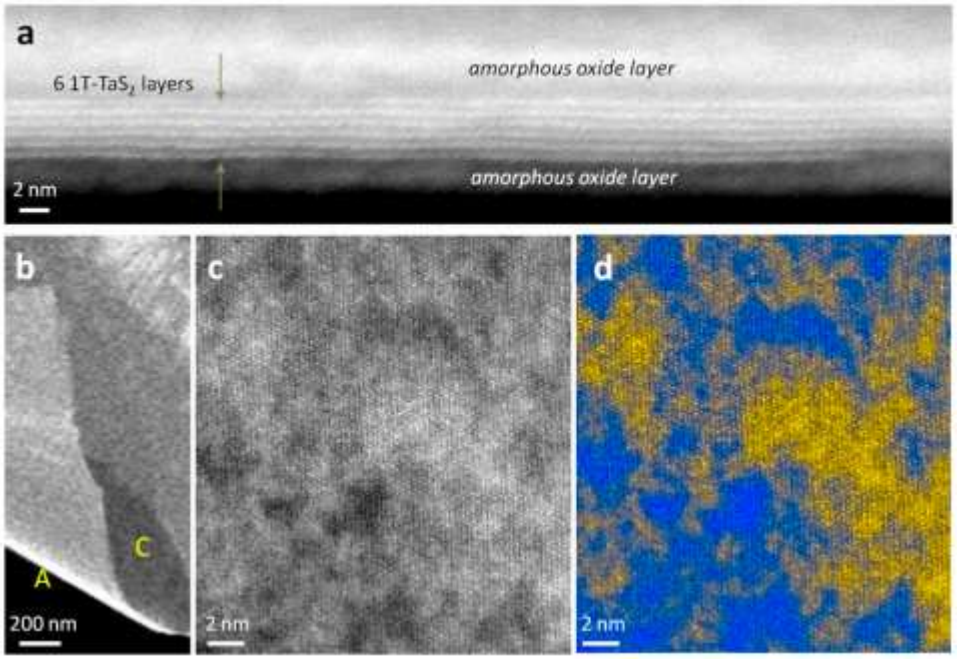

Figure 4.2: High-resolution STEM image of ultrathin 1T-TaS_2 prepared in air. (a) Amorphous layers appear on the top and bottom surfaces. (b) Overview of a curled sheet providing in-plane (A) and planar (C) viewing. (c) High-resolution STEM image of the 1T-TaS_2 sheet shows the high-frequency atomic structure and a lower frequency intensity variation corresponding to the amorphous surface layers. The amorphous surfaces are more clearly visualized in (d), which uses Lab Color space to create blue/yellow contrast of the amorphous (low-frequency) intensity variation.

By contrast, TEM electron diffraction of an ultrathin 1T-TaS_2 crystal (<5 nm thick) exfoliated in and continuously exposed to ambient air showed the same Bragg peaks but a marked absence of any scattering from the CDW (Fig. 4.1c, left panel), suggesting a fundamental structural difference between thin and bulk samples. Fully suspended few-layer samples were studied through high-resolution electron microscopy (Fig. 4.1c, right panel; Fig. 4.2) and energy

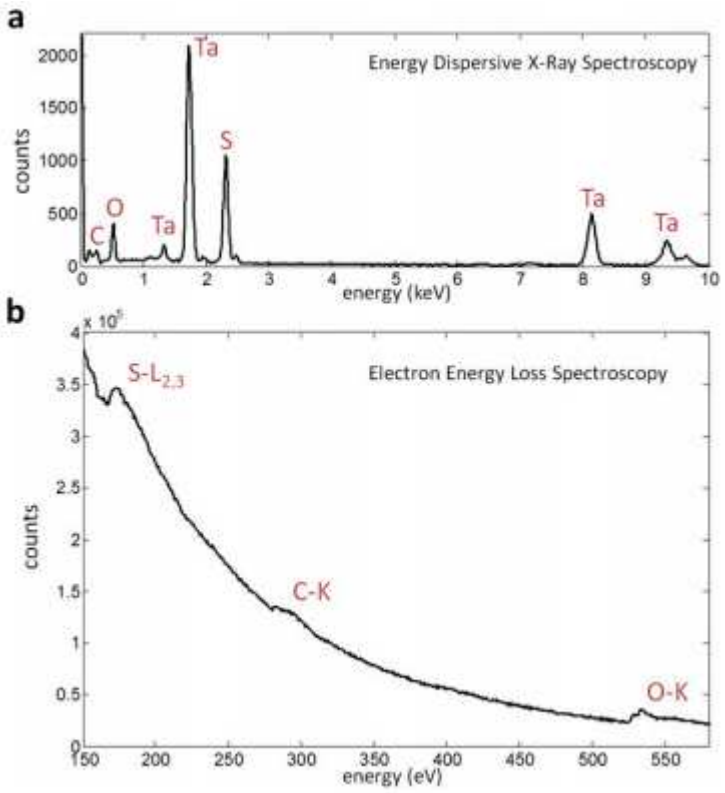

Figure 4.3: Chemical analysis with STEM-spectroscopy of ultrathin 1T-TaS_2 exfoliated in air. In addition to the expected presence of Ta and S, oxygen and trace amounts of carbon are present in both the (a) dispersive X-ray and (b) electron energy loss spectroscopy. The sample was suspended such that all detected elements represent chemical species present in the specimen.

dispersive spectroscopy (Fig. 4.3), and a cross-sectional image shows clear evidence of an amorphous oxide layer on both the sample's top and bottom surfaces. A possible explanation for this is that the formation of the oxide leads to strong surface pinning that prevents charge ordering in the 2-D limit. This hypothesis is supported by the fact that oxidation was not observed in 1T-TaS_2 crystals that were exfoliated and encapsulated with hBN in a glovebox filled with nitrogen (containing <2 ppm of oxygen), all the way down to the thinnest samples measured (2 nm), as discussed in detail in Fig. 4.8.

4.3 Electronic properties

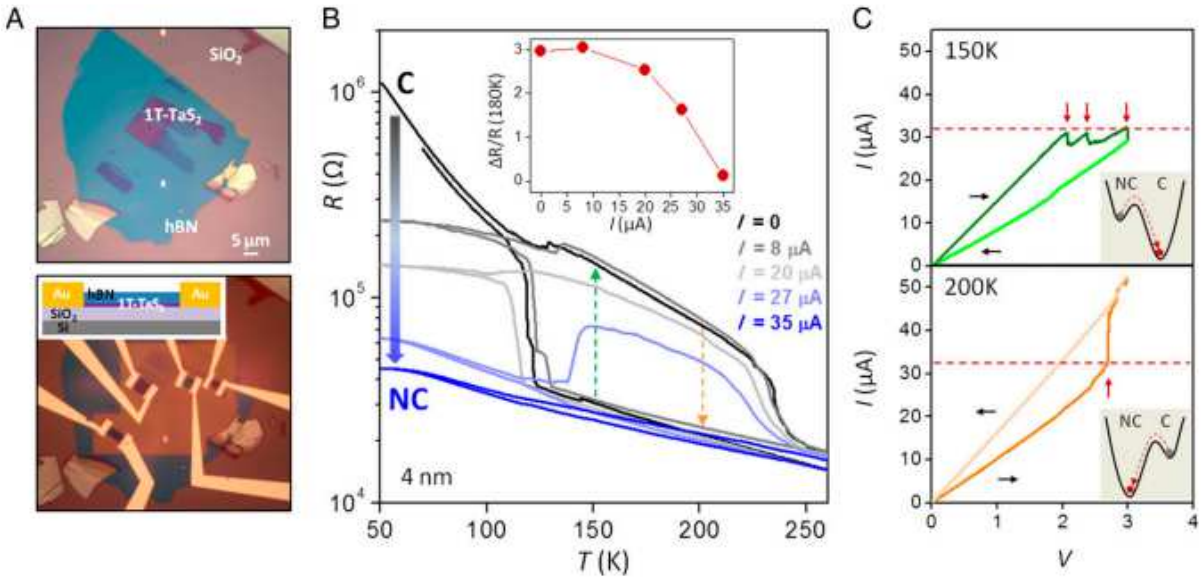

Figure 4.4: Electrical control of NC-C transition in oxidation-free, 2-D devices. (a) Optical images of 1T-TaS_2 flakes on a SiO_2/Si wafer covered by hBN in inert atmosphere before (*Upper*) and after (*Lower*) side electrical contact. (*Inset*) Side-view device schematic. (b) AC resistance vs. temperature for 4-nm-thick device as a function of DC current. Continuous current flow stabilizes NC phase at low temperature. Normalized resistance difference between cooling and warming is plotted as a function of DC current in *Inset*. (c) (*Upper*) Current vs. voltage sweep at 150 K starting in NC phase shows abrupt decreases in current and transition to the C phase. (*Lower*) Same at 200 K starting in C phase shows abrupt increase in current and transition to NC phase. Sweep rate is 3-6 V/min. Free energy schematics of electrically induced transitions are plotted in *Insets*.

Electronically, the different phases of 1T-TaS_2 can be distinguished from one another by their resistivity, which varies with temperature. Figure 4.1b shows that the resistivity of 1T-TaS_2 can abruptly increase (decrease) by over an order of magnitude upon cooling (heating) from the NC (C) to C (NC) phase, where the hysteresis in temperature reflects the metastability of each phase in that region. From a free energy standpoint for a first-order transition (Fig. 4.1d), the NC and C states are separated by an activation barrier, and the overall state of the system is determined by whether or not it has enough thermal energy to overcome the barrier and settle into the lower

energy configuration. As the temperature decreases, so do the activation barrier as well as the energy minimum of the C state relative to the NC state, and vice versa during heating. Again, it is worth noting that while one phase may be energetically favorable over the other for a range of temperatures, it is only when the system acquires sufficient thermal energy to surmount the activation barrier that it breaks free from the metastable state and enters a stable one.

Shown in Fig. 4.4a are optical micrographs of 1T-TaS_2 flakes post-encapsulation (top) and post-fabrication (bottom). Electrical contact to the material was established through edge contacts, shown schematically from the side in the bottom inset (see Methods section in this chapter and Ref. [10]). The resistance versus temperature plot in the main panel of Fig. 4.4b (I = 0, black curve) is for a 4 nm sample, also across the NC-C transition; compared to the behavior observed in bulk TaS_2 (Fig. 4.1b), here the hysteretic loop in temperature is widened significantly and suggests that at least one of the phases has become more metastable.

4.4 Controlling phase through DC currents

Past studies have proved that CDWs couple directly to electric field, making metastable CDW phases more susceptible to electronic perturbations. [6, 11-13] The device examined here demonstrates the improved stability of the NC state at low temperatures with continuous current flow. Figure 4.4b shows that as an additional DC current was increased from 0 to 35 μA for a fixed AC current, the device resistance decreased until the system remained stable in the NC state at temperatures where it would otherwise have transitioned to the C state. The increase in resistance near the phase transition temperature for bulk crystals was also no longer as abrupt at higher DC currents, disappearing altogether at 35 μA. This is plotted in the inset of Fig. 4.4b, where the vertical axis is the ratio of the difference in resistance ΔR between warming and

cooling to the resistance R at T = 180 K (the more conductive state), while the horizontal axis is current. The overall downward slope suggests that current flow prevents the NC phase from transitioning into the C phase. In the case of high DC current and no NC to C phase transition, the current was slowly reduced back to zero at low temperature but the resistance did not change, eliminating Joule heating as the reason for the suppressed transition. Furthermore, the sample reproduced the same current versus temperature plot as before upon cooling and warming again (Fig. 4.5), indicating that no irreversible damage had occurred while adding the DC current.

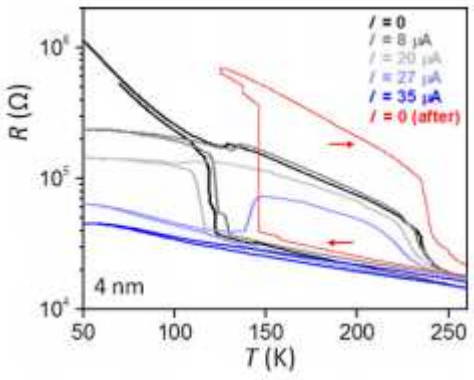

Figure 4.5: Resistance vs. temperature before and after DC current measurements. Trace for I = 0 (after) reproduces original phase transitions suppressed by large DC current.

Having shown that a thermodynamically metastable NC phase can persist down to lower temperatures via the application of a DC current, it is also possible to show that the metastable state can be driven into a stable one by applying an in-plane current after the sample is in thermal equilibrium at a fixed temperature. In particular, in the absence of current flow, the same 4 nm thick sample was cooled from room temperature to 150 K, throughout which it remained in the NC state although the C state is thermodynamically favored at 150 K. There, the voltage across the sample was ramped up while measuring the current through it, as in Fig. 4.4c. The upper panel shows that the measured current increased linearly with voltage (dark green curve) up to a critical current of ~30 μA (red dashed line), when further increases in voltage caused the current

to decrease abruptly in small steps (marked by red arrows). The device remained in the insulating C state upon dialing the bias current back down to zero. At this point, warming up the sample produced a temperature curve resembling the C phase, which transitioned back to the NC phase later on. The dashed green arrow in Fig. 4.4b shows this current-induced NC to C transition, with a corresponding free energy schematic in the upper inset of Fig. 4.4c.

Likewise, the same application of current can drive the reverse transition from a metastable C to a stable NC state. The sample was warmed from 50 to 200 K while in the C phase. At 200 K, the voltage was again swept up, producing a dramatic increase in current and concomitant transition to the NC phase. This is denoted by the orange arrow in Fig. 4.4b and lower inset of Fig. 4.4c. In both directions of the NC-C phase transition, the critical current hovered around 30 μA, suggesting that the current flow, not electric field, was responsible for the transition. It was confirmed that no transition was induced at 260 K up to 45 μA, which is consistent with the fact that no metastable state resides there.

4.5 Discommensurations and dimensionality

Together, these observations point to the ability to controllably tune a NC-C phase transition in thin 1T-TaS_2 through electrical means, alternating between a stable and metastable state for a range of temperatures by effecting or suppressing the transformation. Structurally, the NC phase differs from the C phase in that the former possesses a discommensuration network surrounding commensurate domains while the latter does not (Fig. 4.1b, red inset), thus the NC-C phase transformation can also be interpreted as a discommensuration-melting transition. [14, 15] Assuming that the transport properties within these domains are similar to those of the C phase, the transport data show that they are at least an order of magnitude more resistive than their

surroundings. [3] This is consistent with the observation from a previous study showing that the discommensurations have an atomic structure similar to the metallic phase of 1T-TaS_2. [9]

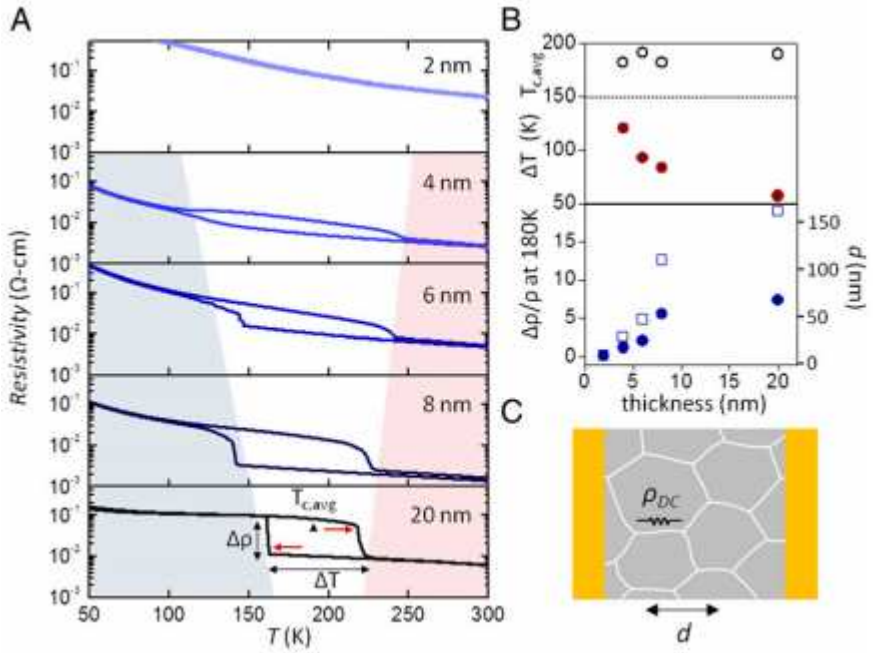

Figure 4.6: Dimensional dependence of phase transition – electron transport. (a) Thickness evolution of temperature-dependent resistivity around NC-C phase transition measured on hBN-covered ultrathin samples and 20-nm-thick flake. (b) Average transition temperature and temperature hysteresis (*Upper*) and normalized resistivity difference (*Lower*) between cooling and warming as a function of sample thickness. Open squares are corrections from contact resistance (Fig. 4.7). Hysteresis widens and resistivity difference decreases in thinner samples, whereas average transition temperature remains constant. Resistivity change can be used to estimate the discommensuration density 1/d at low temperature. (c) Circuit model of discommensuration network.

Dimensionality is yet another parameter that governs the transport properties of 1T-TaS_2. As the thickness of encapsulated samples decreased from 8 to 2 nm (in 2 nm increments), their resistivity profiles changed continuously as seen in Fig. 4.6a from bottom to top using a 1 K/min sweep rate. The resistivity versus temperature profile for an unencapsulated 20 nm flake has also been included for reference; its electrical properties resembled that of a bulk sample, suggesting the diminished effect of oxidation at this thickness. Thinner samples, on the other hand, had a

hysteresis loop stretching over a wider range of temperatures, consistent with data for the device in Fig. 4.4a. This is plotted quantitatively in Fig. 4.6b, which shows, in the upper and middle panels respectively, the average temperature $T_{c,avg}$ at which the transition occurs and the width of the hysteresis loop $\Delta T = T_{c,warm} - T_{c,cool}$ (the transition temperatures upon warming and cooling), both as a function of sample thickness. Since the change in resistivity was not infinitely steep during the phase transitions, especially for thinner samples, T_c is defined as the temperature at which the first derivative in resistivity was maximized. ΔT increases from 40 K for a bulk crystal, to 60 K for the 20 nm device, and finally to 120 K for the 4 nm device. $T_{c,avg}$ did not vary appreciably across different thicknesses, staying between 180 and 190 K. This means that 1T-TaS_2 does not preferentially reside in the NC or C phase as it is thinned down, but rather that the metastable phase, whichever it may be depending on the direction of the temperature sweep, is prolonged due to a heightened energy barrier between the phases (Fig. 4.1d). The difference in

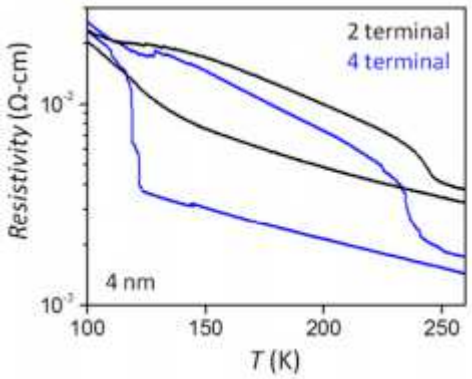

Figure 4.7: Extracting contact resistivity. Two- and four-terminal resistivity vs. temperature for 4-nm-thick flakes. The difference is proportional to resistivity of edge contacts.

resistivity, however, tended to be smaller in thinner samples than their thicker counterparts at a given temperature until it vanished altogether at 2 nm, where no transition was observed. The bottom panel of Fig. 4.6b plots the difference in resistivity $\Delta\rho$ between warming and cooling at

180 K, normalized to ρ of the more conductive NC phase, versus sample thickness – here, the set of solid circles are plotted directly from experimental data in Fig. 4.6a while the open squares account for contact resistance (Fig. 4.7). From the data, the 20 nm sample underwent a jump in resistivity about an order of magnitude larger than that of the 6 nm sample at the phase transition, and the 2 nm sample did not undergo a jump at all, suggesting the presence of more discommensurations characteristic of the NC state caused by larger energy barrier upon thinning. Furthermore, the larger energy barrier in thinner samples hinders the kinetics of the NC-C transition as evidenced by the smoother jumps in that limit. This can be better understood by modeling the discommensurations as a network of resistors (as shown by white lines in Fig. 4.6c) possessing a characteristic length d, or equivalently, a density 1/d. With d being much smaller than the length of the device and conduction at low temperatures occurring through this network, it can be deduced that $R \sim \rho_{DC}*d$, where ρ is the resistivity per unit length of each discommensuration channel. At higher temperatures, where the discommensuration network is well-defined, $R_{NC} \sim \rho_{DC}*D_{NC}$ with $D_{NC} \sim 80$ Å. [7, 8] Combining these two equations yields $(\Delta R/R_{NC}) \sim (d/D_{NC}) - 1$, which can be solved for d using data from Fig. 4.6b; it turns out that $d \sim D_{NC}$ for the 2 nm sample, increasing to 70-160 nm for the 20 nm sample.

TEM diffraction images of encapsulated 12 nm and 2 nm samples at high and low temperatures complement the data seen in transport. Figure 4.8a displays overlaid diffraction patterns at 295 K (red peaks) and 100 K (blue peaks) for the 12 nm (left panel) and 2 nm (right panel) samples. Note that 100 K was the lowest achievable temperature here. As before, Ta Bragg peaks are connected by dashed white lines. Extra dimmer peaks are visible here compared to the blue panel in Fig. 4.1a due to the hBN overlayer. Gray circles highlight CDW peaks in both panels, but peaks circled in blue for the 12 nm sample are noticeably absent for the 2 nm

sample, indicating the former has fully transitioned into the C phase while the latter remains in the NC phase at 100 K. This picture is consistent with the transport data in Fig. 4.6a.

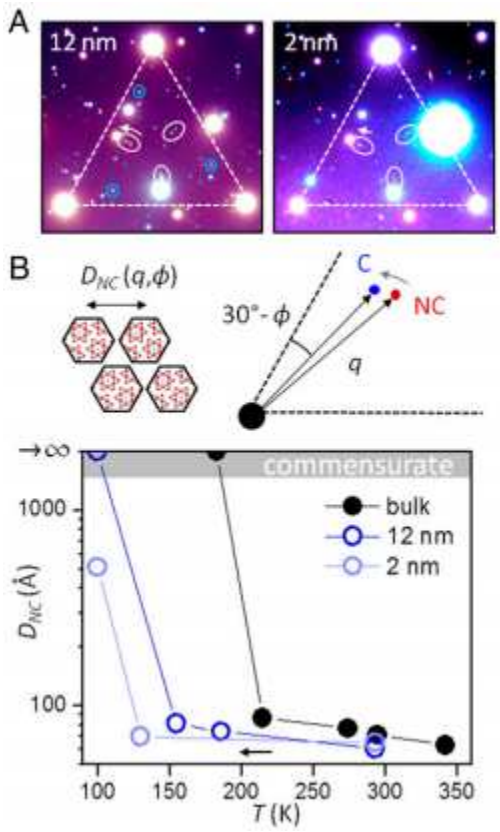

Figure 4.8: Dimensional dependence of phase transition – electron diffraction. (a) Overlaid TEM diffraction images of ultrathin 1T-TaS_2 covered with hBN taken at 295 K (red peaks) and 100 K (blue peaks) for two flake thicknesses. hBN preserves CDW order (circled peaks) but introduces additional diffraction spots. (b) (upper right) Zoom-in schematic of CDW diffraction peaks showing temperature evolution. Position of NC spot can be used to estimate commensurate domain periodicity D_{NC} (upper left). (lower) D_{NC} vs. temperature with cooling measured for the two covered samples compared with data reproduced from Ref. [8]. Reduced thickness pushes NC to C phase transition to lower temperature.

The movement of the red peak within the gray circle from the NC to C position in Fig. 4.8a upon cooling can be analyzed quantitatively (referring to the schematic in Fig. 4.8b, upper right) to obtain the domain periodicity D_{NC}, according to Ref. [8]:

$$D_{NC} = \frac{a}{\sqrt{(\frac{2\pi\Delta\varphi}{360}°)^2 + (\frac{\Delta\lambda}{\lambda_c})^2}}$$

Here, $\Delta\varphi = \varphi - \varphi_C$, $\varphi_C = 13.9°$, $\Delta\lambda$ is the apparent wavelength averaged over many domains, and $\lambda_C = \sqrt{13}a$. As the domains grew larger, the NC peaks moved closer to the C peaks. D_{NC} can be extracted using the measured position and angle of the CDW wavevectors for these two samples over a range of temperatures; the results are shown in Fig. 4.8b, along with STM data from the surface of a bulk sample by Thomson et al. [8] While the width of the discommensuration region remained relatively fixed at ~22 Å when bulk 1T-TaS_2 was in the NC phase, D_{NC} was largely temperature-dependent, growing from 60 to 90 Å to an arbitrarily large value as the temperature decreased from 340 to 215 to ~180 K, respectively. Thinning the sample delayed the onset of the C phase (from the NC phase) to lower temperatures and slowed the growth of CDW domains during the transition. D_{NC} for both thin flakes was comparable to that of a bulk crystal at room temperature (~60-70 Å); upon cooling, the 12 nm flake made the transition from NC to C between 100 and 150 K, whereas no full transition was observed for the 2 nm flake even down to 100 K. Nevertheless, at 100 K D_{NC} grew to roughly 500 Å, showing that the transition occurred slowly but surely.

Both transport and TEM measurements indicated that the barrier between the NC and C phases strengthens as the dimensionality is reduced, widening the metastable region of the transition. Physically, the transition involves melting or dismantling the NC discommensuration network, and previous studies have suggested that the barrier is caused by local pinning due to defects or impurities in the material. [16] Clusters of localized defects have been confirmed by STM studies on nominally pure samples, where the spacing between adjacent defects is on the order of 10 nm. [17, 18] The impact of these defects is reduced in bulk 1T-TaS_2 because the

interlayer stacking of NC domains effectively extends the presence of discommensuration walls [9, 19], unlike in 2-D samples where the NC domains become lines that are pinned down more easily. This is illustrated for a 2-D model of thickness t in Fig. 4.9, which shows that when t is less than the mean spacing between impurities, the pinning energy for a discommensuration

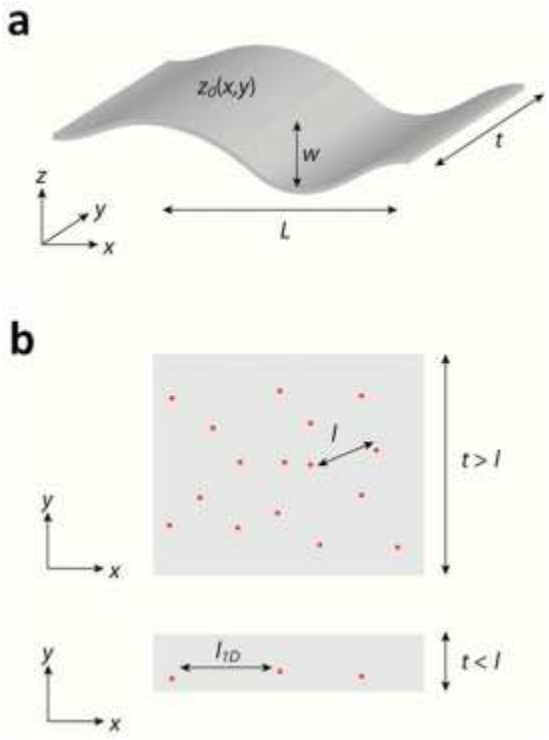

Figure 4.9: Schematic picture of a DC plane and important length scales. (a) shows 3-D view and (b) shows 2-D projection. Red dots denote the location of impurities inside a DC plane. The effective mean impurity distance is l for $t > l$, whereas it is $l_{1\text{-}D}$ for $t < l$.

plane scales as $E_{pin} \sim t^{-2/3}$, transitioning from collective weak pinning to strong individual pinning. The pinning acts to stabilize the NC discommensuration network while cooling but also prevents the nucleation and growth of discommensurations while warming, extending the range of metastability in both directions as per the experimental results.

This model may also help explain the role of DC currents in driving or suppressing phase transitions as seen in Fig. 4.4b, c. Cooling down 1T-TaS_2 in equilibrium starting from the NC

state lowers the energy barrier, and an added DC current accelerates this process by giving an extra push to the system towards the C phase ground state, driving away discommensurations and allowing domains to grow steadily (Fig. 4.4c). On the other hand, flowing a large DC current while cooling down prevents domain growth and the transition into the C state (Fig. 4.4b). Thus the DC current provides a knob to tune the activation barrier between the NC and C phases.

4.6 Synthesis of 1T-TaS_2

High-quality single crystals of 1T-TaS_2 were grown by the chemical vapor transport (CVT) method with iodine as a transport agent. The high-purity Ta (3.5 N) and S (3.5 N) were mixed in chemical stoichiometry and heated at 850 °C for 4 days in an evacuated quartz tube. The harvested TaS_2 powders and iodine (density: 5 mg/cm^3) were then sealed in another quartz tube and heated for 2 weeks in a two-zone furnace, in which the source zone and growth zone were fixed at 900 °C and 800 °C, respectively. The tubes were rapidly quenched in cold water to ensure retaining of the 1T phase.

4.7 Device assembly and fabrication

Thin TaS_2 was exfoliated onto SiO_2/Si wafers inside a N_2-filled glovebox containing below 2 ppm O_2 concentration. Outside the glovebox single-crystal hBN flakes were exfoliated separately onto SiO_2/Si. Using a PDMS stamp covered with PPC, thin hBN (<30 nm thick) was picked up via the method described in Ref. [10]. This sample was then moved inside the glovebox. To prepare the 1T-TaS_2 for TEM study, the hBN was used again to pick up 1T-TaS_2 in situ and the hBN/1T-TaS_2 transferred onto a TEM chip with a SiN membrane. The chip was then moved outside of the glovebox and cleaned in acetone, followed by isopropanol.

To prepare 1T-TaS_2 for transport studies, flakes were again exfoliated on SiO_2/Si inside the glovebox. hBN was used to cap 1T-TaS_2 in a manner similar to that described above. First, electron beam resist (950K PMMA A6, thickness ~300 nm) was used as an etch mask to define the device channel. The pattern was written using a 30 keV electron beam lithography system with an exposure dosage between 300 and 450 $\mu C/cm^2$. Afterward, the stack was etched in an Oxford ICP 80 system using plasma generated from a mixture of O_2 and CHF_3 gases with a flow rate of 4 and 40 sccm, respectively. This etch leaves 1T-TaS_2 exposed at the edges of the channel. It was found that a 1-min etch time can completely etch away flakes under 10 nm thick.

A subsequent lithography step was then used to pattern metal electrodes contacting the 1T-TaS_2 edge. A second identical etch was performed immediately before metal evaporation (1 nm Cr/50 nm Au) to expose a new edge with reduced oxidation. Alternatively, thin 1T-TaS_2 was picked up with hBN/graphene heterostructures and the entire stack placed on another hBN substrate. Here, few-layer graphene was used as electrodes to contact the top surface of the 1T-TaS_2. No substantial difference was seen in the temperature-dependent resistivity behavior between these two processes.

4.8 SEM/TEM

The conventional TEM experiments, including electron diffraction, were conducted on an FEI T12 Bio-Twin operating at 80 keV. Temperatures as low as ~97 K were accessible using a cryogenic specimen stage. A high vacuum environment and the microscope's fixed cryo-shields prevented accumulation of ice on the specimen when held at low temperatures. High-resolution scanning TEM images were collected on a FEI Tecnai F20 transmission electron microscope

operating at 200 keV with a probe forming a semiangle of roughly 9.6 mrad and a high-angle annular dark field detector at a camera length of 150 mm.

4.9 Conclusions

The results in this chapter clearly demonstrate the ability to electrically control the NC-C phase transition in ultrathin 1T-TaS_2, making it potentially useful for device applications, and shed light on the nature of its 2-D state. Specifically, it was established that the system could be preferentially driven into either the NC or C state depending on its initial conditions as well as whether or not an additional DC current is present. Moreover, the encapsulation technique that allowed for these studies may also be applied to other air-sensitive TMDs.

The contents of this chapter were published as [20]. The author of this thesis was an author of this paper, who contributed to device fabrication, electronic transport measurements, and data analysis.

4.10 References

1. Li, L. J., et al. "Fe-doping–induced superconductivity in the charge-density-wave system 1T-TaS_2." *EPL (Europhysics Letters)* 97.6 (2012): 67005.
2. Liu Y, et al. (2013) Superconductivity induced by Se-doping in layered charge-density wave system 1T-$TaS_{2-x}Se_x$. *Applied Physics Letters* 102(19): 192602.
3. Sipos B, et al. (2008) From Mott state to superconductivity in 1T-TaS_2. *Nature Materials* 7(12): 960–965.
4. Yoshida, Masaro, et al. "Controlling charge-density-wave states in nano-thick crystals of 1T-TaS_2." *Scientific Reports* 4 (2014): 7302.
5. Yu, Yijun, et al. "Gate-tunable phase transitions in thin flakes of 1T-TaS_2." *Nature Nanotechnology* 10.3 (2015): 270.
6. Yoshida, Masaro, et al. "Memristive phase switching in two-dimensional 1T-TaS_2 crystals." *Science Advances* 1.9 (2015): e1500606.
7. Wu, Xian Liang, and Charles M. Lieber. "Direct observation of growth and melting of the hexagonal-domain charge-density-wave phase in 1T-TaS_2 by scanning tunneling microscopy." *Physical Review Letters* 64.10 (1990): 1150.
8. Thomson, R. E., et al. "Scanning tunneling microscopy of the charge-density-wave structure in 1T-TaS_2." *Physical Review B* 49.24 (1994): 16899.
9. Spijkerman, Albert, et al. "X-ray crystal-structure refinement of the nearly commensurate phase of 1 T− TaS_2 in (3+ 2)-dimensional superspace." *Physical Review B* 56.21 (1997): 13757.
10. Wang, L., et al. "One-dimensional electrical contact to a two-dimensional material." *Science* 342.6158 (2013): 614-617.

11. Hollander, Matthew J., et al. "Electrically driven reversible insulator–metal phase transition in 1T-TaS_2." *Nano Letters* 15.3 (2015): 1861-1866.
12. Vaskivskyi, I., et al. "Fast non-thermal switching between macroscopic charge-ordered quantum states induced by charge injection." *arXiv preprint arXiv:1409.3794* (2014).
13. Gruner, George. *Density waves in solids*. CRC Press, 2018.
14. McMillan, W. L. "Landau theory of charge-density waves in transition-metal dichalcogenides." *Physical Review B* 12.4 (1975): 1187.
15. McMillan, W. L. "Theory of discommensurations and the commensurate-incommensurate charge-density-wave phase transition." *Physical Review B* 14.4 (1976): 1496.
16. Rice, T. M., S. Whitehouse, and P. Littlewood. "Impurity pinning of discommensurations in charge-density waves." *Physical Review B* 24.5 (1981): 2751.
17. Giambattista, B., et al. "Scanning tunneling microscopy of atoms and charge-density waves in 1T-TaS_2, 1T-$TaSe_2$, and 1T-VSe_2." *Physical Review B* 41.14 (1990): 10082.
18. Arguello, C. J., et al. "Visualizing the charge density wave transition in 2H-$NbSe_2$ in real space." *Physical Review B* 89.23 (2014): 235115.
19. Tanda, Satoshi, et al. "X-ray study of charge density wave structure in 1T-TaS_2." *Journal of the Physical Society of Japan* 53.2 (1984): 476-479.
20. Tsen, Adam W., et al. "Structure and control of charge density waves in two-dimensional 1T-TaS_2." *Proceedings of the National Academy of Sciences* 112.49 (2015): 15054-15059.

Chapter 5

Electronic transport in graphene-CrX_3 heterostructures

5.1 Motivation

Multiple attempts have been made over the years to induce long-range ferromagnetic order in 2-D systems. [1-5] Recent efforts have focused on coupling graphene to ferromagnetic insulators [6-8], as per theoretical predictions claiming that doing so could give rise to a topological band gap (exchange gap) at the Dirac point of graphene due to strong spin-orbit coupling and a finite exchange interaction between the two materials [9-11]. This induced gap, which leads to a quantized anomalous Hall conductance of $\pm 2e^2/\hbar$, embodies the quantum anomalous Hall effect (QAHE). As shown in Fig. 1.2 (right), the QAHE can be visualized as magnetization within the sample itself producing locking between electron spin and its propagation direction along an edge channel. This contrasts with the quantum Hall effect (QHE), where an external magnetic field causes electrons to propagate in the same direction along edge channels regardless of their spin orientation, and the quantum spin Hall effect (QSHE), characterized by counter-propagating modes along the sample edge. [12] Thus far, the QAHE has only been observed once in an experimental setting, namely, in thin films of Cr-doped $(Bi,Sb)_2Te_3$, a magnetic topological insulator. [13] Since then, researchers have sought to reproduce the phenomenon in van der Waals heterostructures at significantly higher temperatures (from tens of mK to tens of K), a real possibility given pristine interfaces between adjacent layers and far lower defect densities in individual crystals. [14] Chromium trihalides of the form CrX_3 constitute a class of potential ferromagnetic insulators.

This chapter details the fabrication, testing, and overall effectiveness of several such graphene-ferromagnetic insulator heterostructure devices that differ from one another in geometry, with particular attention given to how each new geometry builds on the previous ones.

5.2 Fabrication challenges

There are two main challenges in these experiments. First, the graphene must retain a high mobility even when it is in contact with the magnetic material. From a device fabrication standpoint, this limits the sequence of steps in the procedure as well as the chemicals used at each step. Second, each of the CrX_3 compounds poses a unique challenge in terms of processing, the least of which is sensitivity to air. $CrCl_3$, for instance, dissolves in acetone, a solvent commonly used to clean surfaces. CrI_3, on the other hand, is extremely sensitive to moisture and light. This necessitates working in a N_2-filled glovebox and ensuring that samples are well-encapsulated by hBN. The sample geometries described below, listed in chronological order, demonstrate how various techniques were used to combat these difficulties and improve upon shortcomings of their predecessors.

5.3 Method 1 – $CrCl_3$/graphene/hBN

Graphene and hBN were exfoliated on separate SiO_2/Si substrates and the latter was used to pick up the former as described in Chapter 2. The hBN/graphene stack was "inverted" (such that the graphene lay on top), placed on a new SiO_2/Si substrate, and annealed at 350 °C to remove the PPC prior to performing e-beam lithography to pattern electrical contacts. E-beam lithography was performed by spincoating the substrate with a double layer of poly(methyl methacrylate) (PMMA) 495K A4 and 950K A6 (for a larger undercut compared to a single resist layer), baking

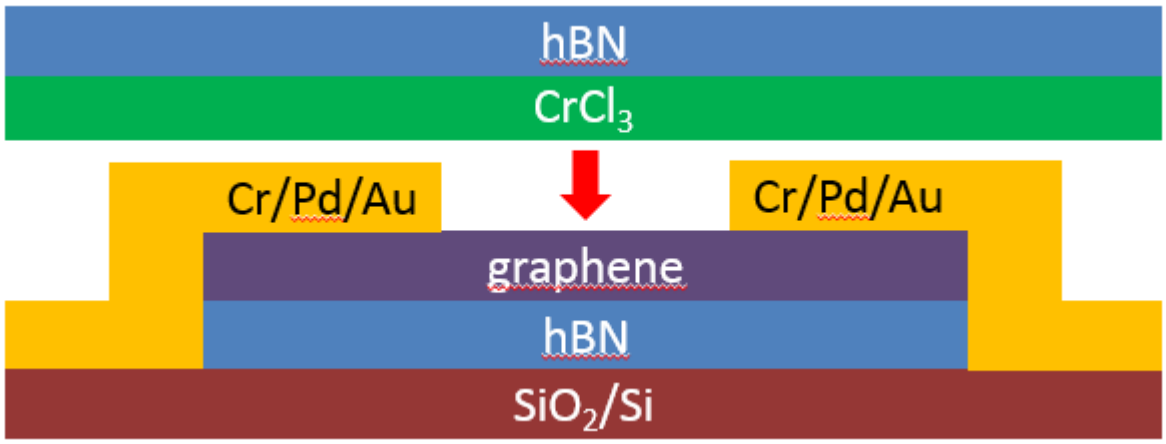

Figure 5.1: Device geometry from Method 1. hBN/$CrCl_3$ were transferred onto a prepatterned stack of graphene/hBN.

on the hot plate at 180 °C after each layer, and using a Nanobeam electron beam lithography system to write the actual design. After removing the exposed resist by developing the chip, Cr/Pd/Au was deposited with thicknesses 2/40/50 nm, respectively. At this point, the device was probed at room temperature to ensure that a Dirac peak could be clearly seen before continuing with subsequent fabrication steps. The same pickup procedure was used to pick up a 10 nm $CrCl_3$ flake with a larger 30 nm hBN flake, both of which were transferred onto the prepatterned graphene/hBN stack. The device geometry is illustrated in Fig. 5.1.

5.4 Method 2 – $CrCl_3$/mono hBN/graphene/hBN

The second device geometry, carried out nearly in parallel with the first, was designed to prevent direct contamination of the graphene surface that Method 1 suffered from, as will be elaborated upon in the data analysis below. Specifically, instead of performing lithography directly on the graphene surface, a monolayer of hBN was first inserted between the $CrCl_3$ and graphene by picking it up after the graphene and before inverting the now 3-layer stack. An additional round of lithography and etching (using CHF_3) was then required to pattern the monolayer

hBN/graphene/thicker hBN into a Hall bar. Only then were side contacts patterned and deposited as in Ref. [15]. The final step was transferring the hBN/$CrCl_3$ as in Method 1. Note, however, that PMMA residue could still reside at the surface of the monolayer hBN, between the graphene and $CrCl_3$. Given the obscured signal believed to arise from contamination at the interface and/or mechanical stress due to the $CrCl_3$ conforming to elevated metal contacts in the first device geometry (again, elaborated upon below), this second geometry was not tested. All efforts were instead redirected toward Method 3. The second device geometry is illustrated in Fig. 5.2.

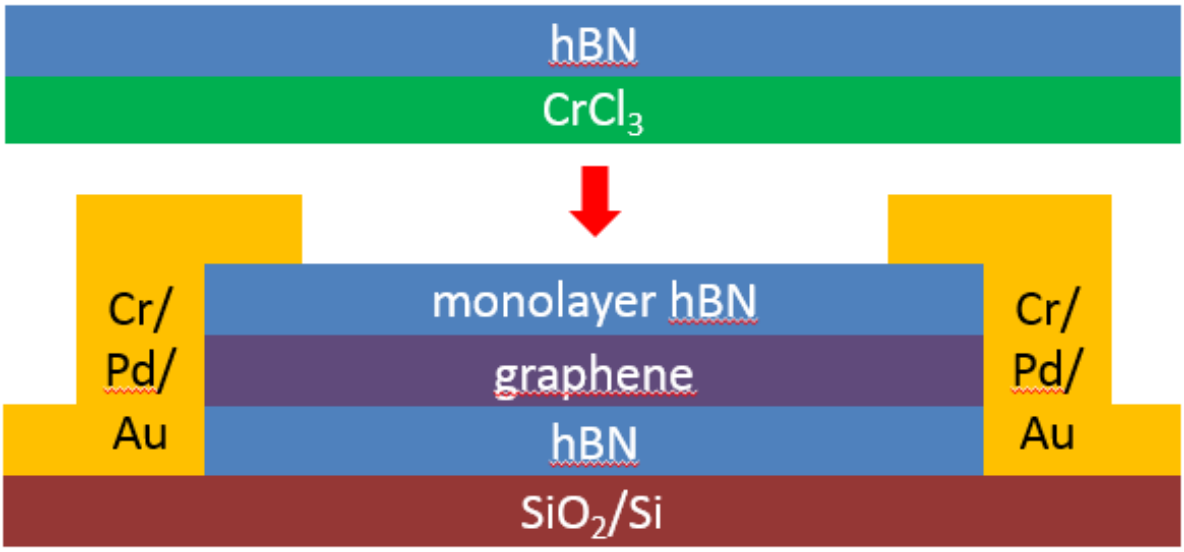

Figure 5.2: Device geometry from Method 2. A monolayer of hBN was added to the graphene/hBN stack before etching, depositing metal contacts, and performing the final hBN/$CrCl_3$ transfer.

5.5 Method 3 – via hBN/graphene/CrI_3

The third device scheme, known as "vias," utilized a new technique for making electrical contact that has recently been tested on other air-sensitive materials such as 2H-$NbSe_2$. [16] This technique was implemented because of its ability to maintain a truly clean interface between the

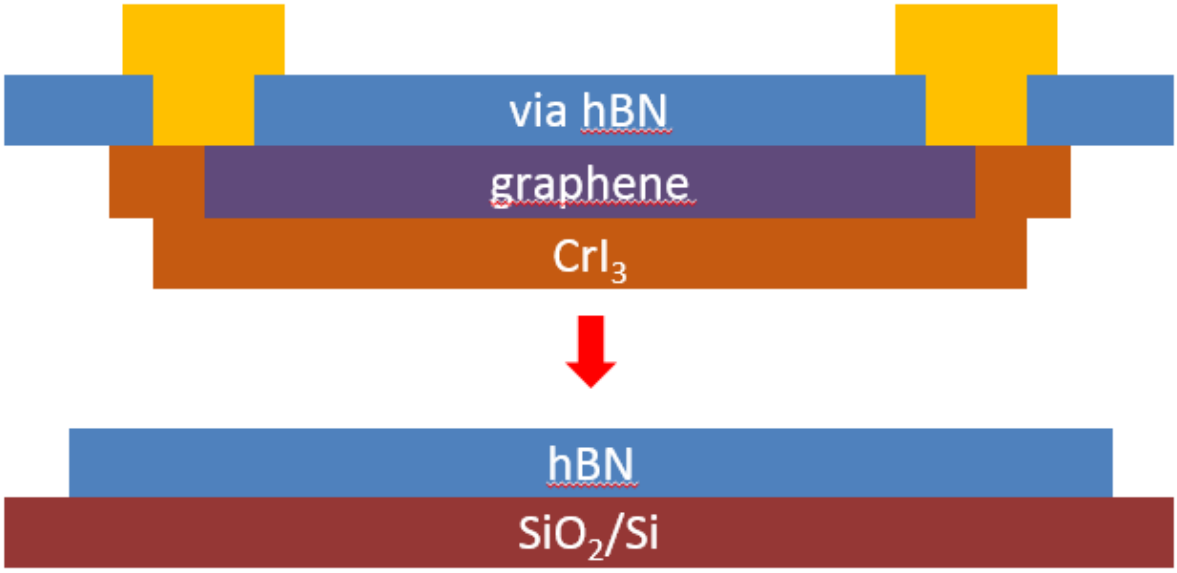

Figure 5.3: Device geometry from Method 3. The via hBN was fabricated first before assembling the rest of the stack.

graphene and ferromagnet, a marked improvement over the previous two device geometries. Vias are another name for metal deposited in lithographically patterned and etched holes in hBN flakes. Given the need for a current drain/source and both transverse and longitudinal voltage probes, the vias were arranged in a Hall bar geometry. A schematic of the completed stack is shown in Fig. 5.3. As described in Ref. [16] and shown in Fig. 5.4, the procedure for making via hBN stacks consists of patterning and etching holes in a relatively thick (~30-50 nm) hBN flake, performing a second round of lithography to open up holes that are slightly larger than the original ones, depositing metal in the holes, picking up the metal-filled hBN, and finally using it to pick up graphene and the ferromagnet. Two points are worth mentioning here before continuing on with the final (ongoing) device geometry and data analysis for the first set of measurements.

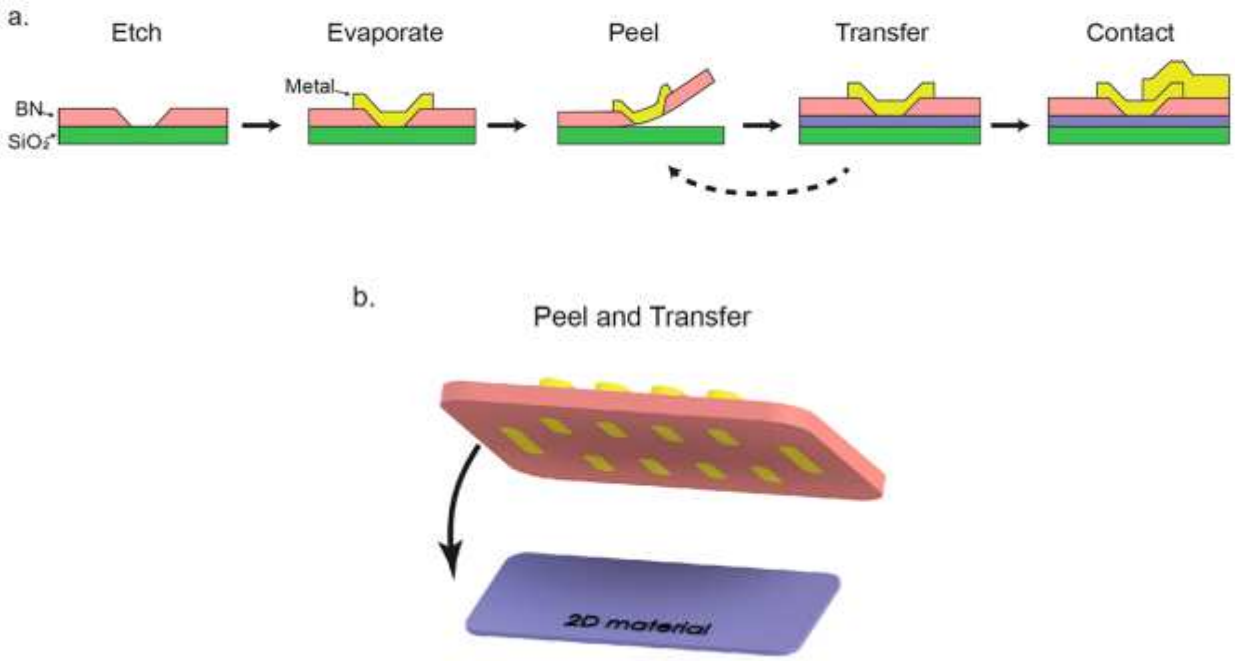

Figure 5.4: Procedure for making via contacts and heterostructures – (a) side view and (b) angle view diagram. Reproduced from Ref. [16].

First, a switch was made from $CrCl_3$ to CrI_3. This was because CrI_3 has a higher magnetic ordering temperature and more pronounced magnetic anisotropy than $CrCl_3$, which could potentially make it easier to observe the QAHE. [17] Moreover, several recent experiments have confirmed the robustness of CrI_3 in the few-layer limit. [18-22]

Second, the effectiveness of double encapsulation by hBN from the top and bottom, where both hBN flakes were continuous and not etched, was tested prior to commencing fabrication with vias. An optically thin piece of CrI_3 was first located in the glovebox and fully sandwiched between larger pieces of hBN above and below. After soaking it in acetone for one hour and monitoring it over set time intervals, it was determined that neither acetone nor moisture could seep through the hBN. This can be seen in Fig. 5.5, where the outline of CrI_3 (highlighted in yellow in Fig. 5.5a) clearly remained after one hour, in stark contrast to unencapsulated flakes of CrI_3 on another chip (Fig. 5.6), which disappeared within seconds.

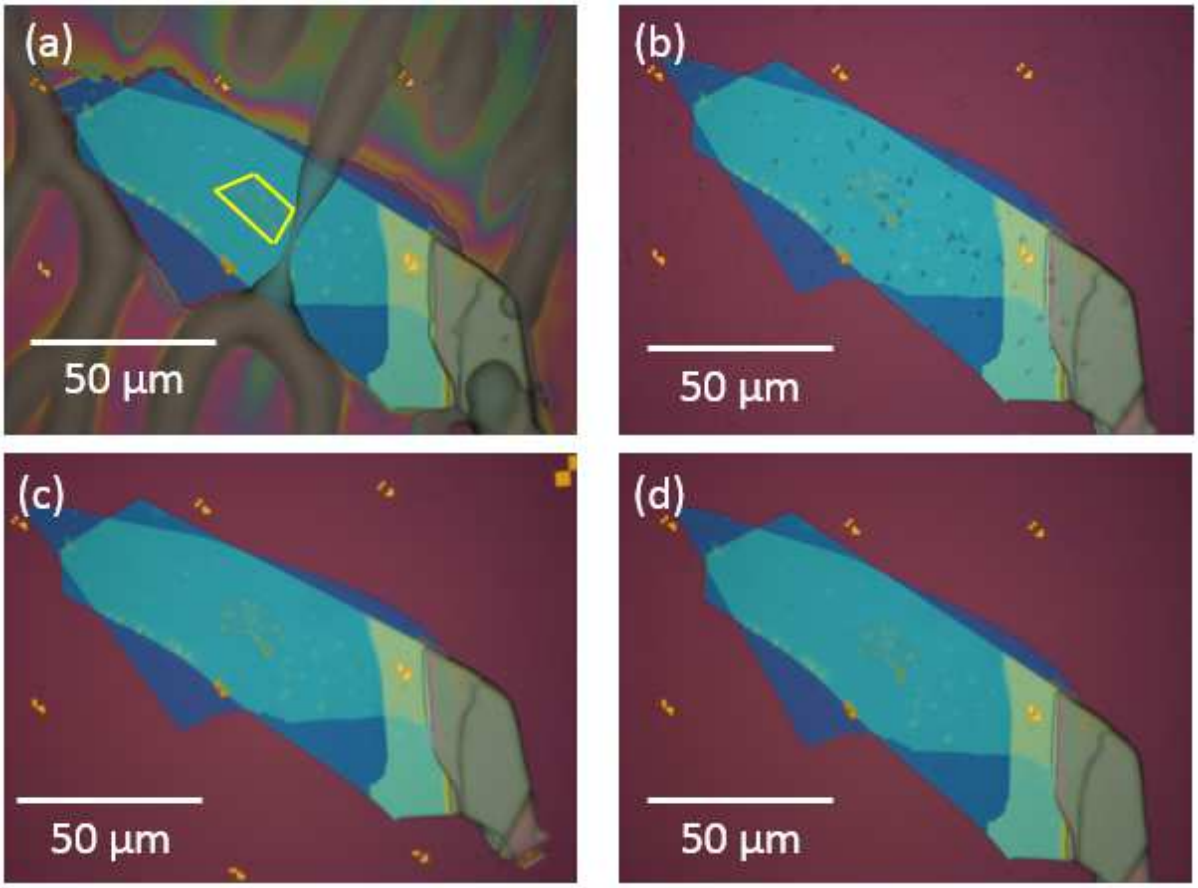

Figure 5.5: Time-lapsed, 100× optical micrographs of thin, doubly encapsulated CrI_3 outlined in yellow in (a). The images were taken in air. Yellow spots on the CrI_3 were present immediately after transferring in the glovebox and were likely gaps between the CrI_3 and the bottom hBN caused by a relatively fast transfer. Before (a) and after soaking in acetone for 10 seconds (b), 1 minute (c), and 2 minutes (d).

Unfortunately, it was found that double encapsulation with a via hBN as the top layer (as opposed to hBN without vias) does not work nearly as well because moisture is able to seep through microscopic openings near the vias and damage the CrI_3 underneath, however tightly sealed they may appear from optical images and AFM (Fig. 5.7). This is consistent with geometric considerations, taking into account the fact that the CrI_3 must contact the vias directly if 1. The latter must lie at the edge of the graphene to capture current flow there, and 2. The CrI_3 must cover the entirety of the graphene, not just part of it, due to the long-range nature of the

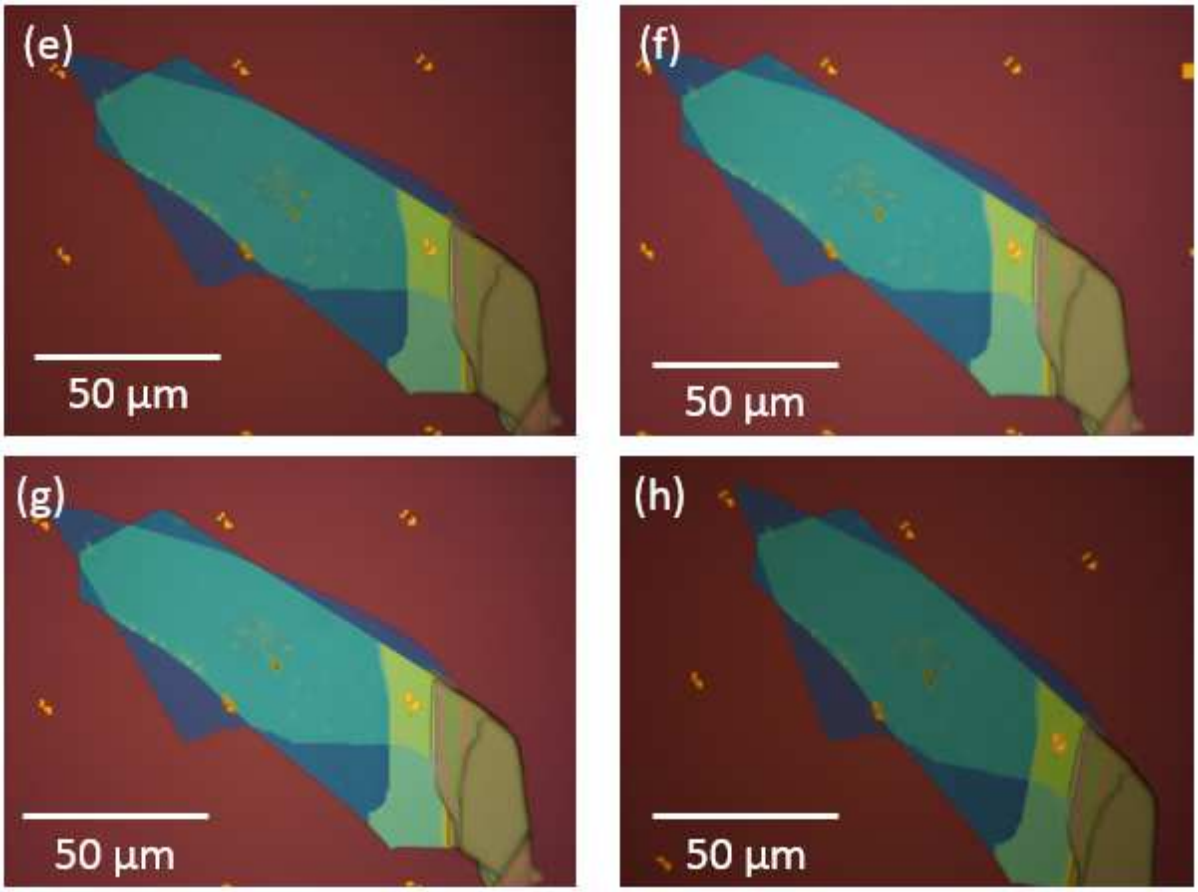

Figure 5.5 (cont.): Optical images of doubly encapsulated CrI_3 after soaking in acetone for 5 minutes (e), 10 minutes (f), 30 minutes (g), and 1 hour (h).

QAHE. As such, a fourth device geometry was sought that would prevent moisture from affecting the underlying CrI_3 in any way.

5.6 Method 4 – etched hBN/mono hBN/graphene/CrI_3/hBN

The fourth device scheme builds upon the third by aiming to eliminate any gaps in the vias through which moisture can enter and damage the CrI_3. This is achieved as follows. First, a Hall bar pattern is etched on the top hBN without depositing the metal yet (labelled in Fig. 5.8 as the "unfilled via hBN"). Next, polycaprolactone (PCL) is used to pick it up at approximately 40 °C

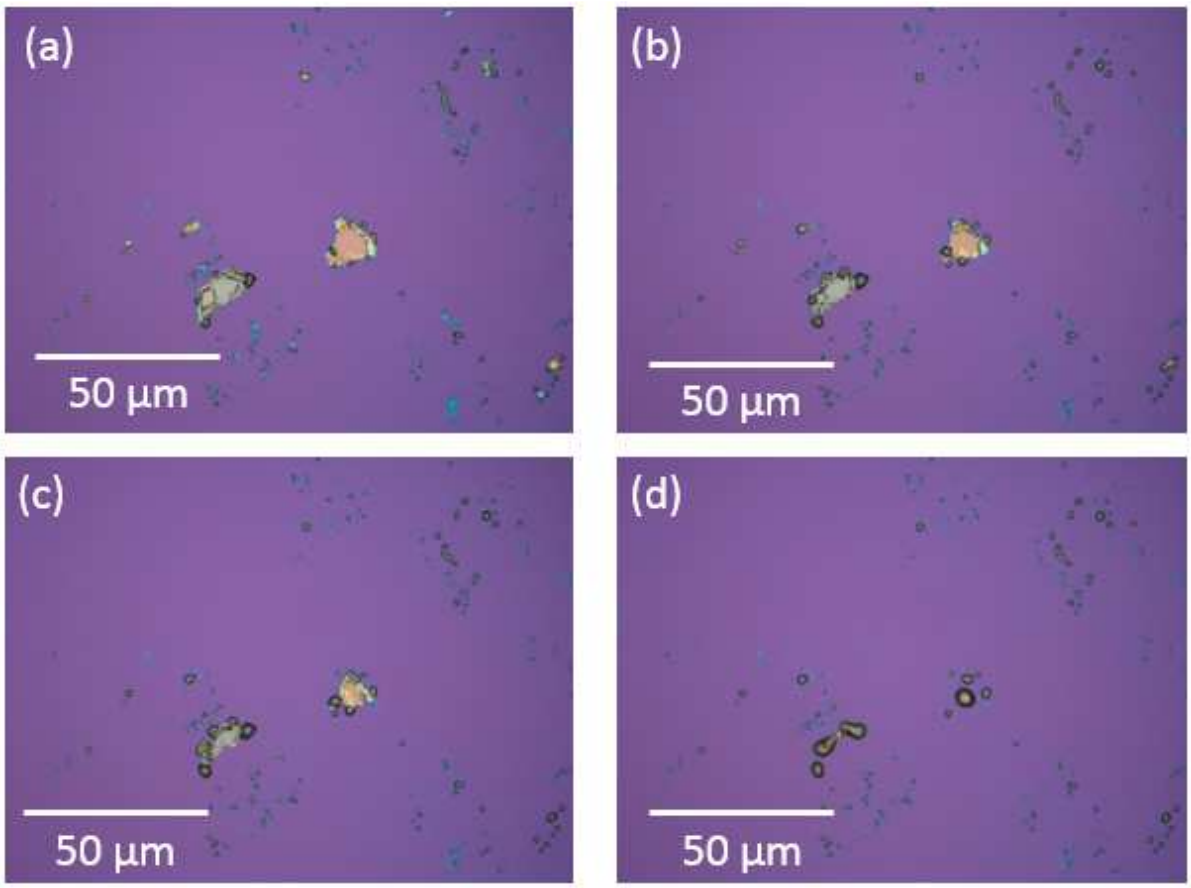

Figure 5.6: 100× optical images of unencapsulated CrI_3 in air. (a)-(d) were acquired in order over the course of ~10 s; no precise times are provided here due to the extremely short time scales over which degradation took place.

(according to the procedures outlined in Chapter 2), followed by a monolayer or bilayer of hBN. PCL is favored over PPC in this case because PCL is stickier and has been known to pick up ultrathin hBN without making it crack. The mono- or bilayer hBN serves as a tunnel barrier that simultaneously blocks the entry of moisture while allowing electrons to tunnel through. From the literature, the tunneling current through hBN of these thicknesses remains linearly proportional to the applied voltage, assuming the latter is at low bias. [23-24] After picking up the graphene and CrI_3 and transferring them onto the bottom hBN, metal contacts are finally evaporated into the holes in the top hBN.

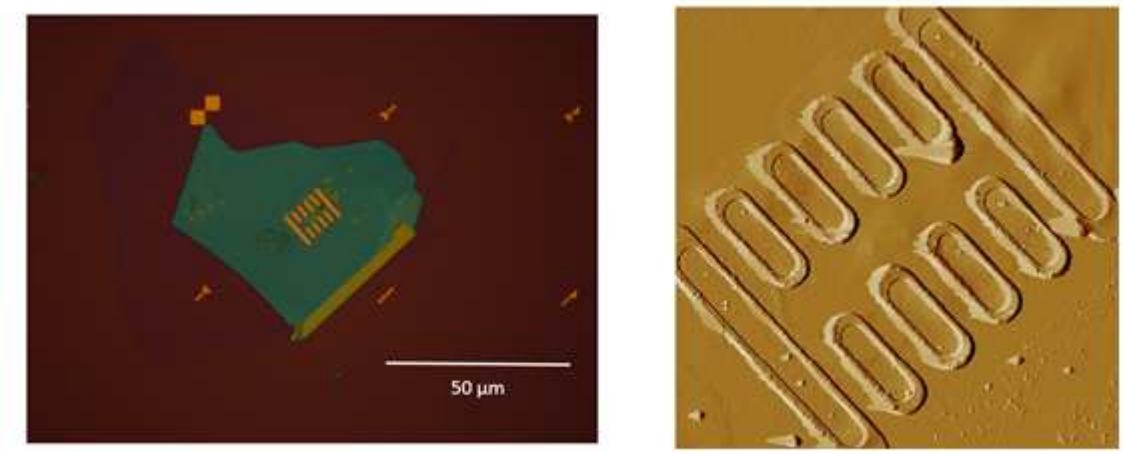

Figure 5.7: Optical micrograph (left) and zoomed in AFM image (right) of via hBN/graphene/CrI_3 stack made using Method 3. No cracks or shifting of the vias were evident, but the CrI_3 underneath had completely disappeared in a matter of minutes.

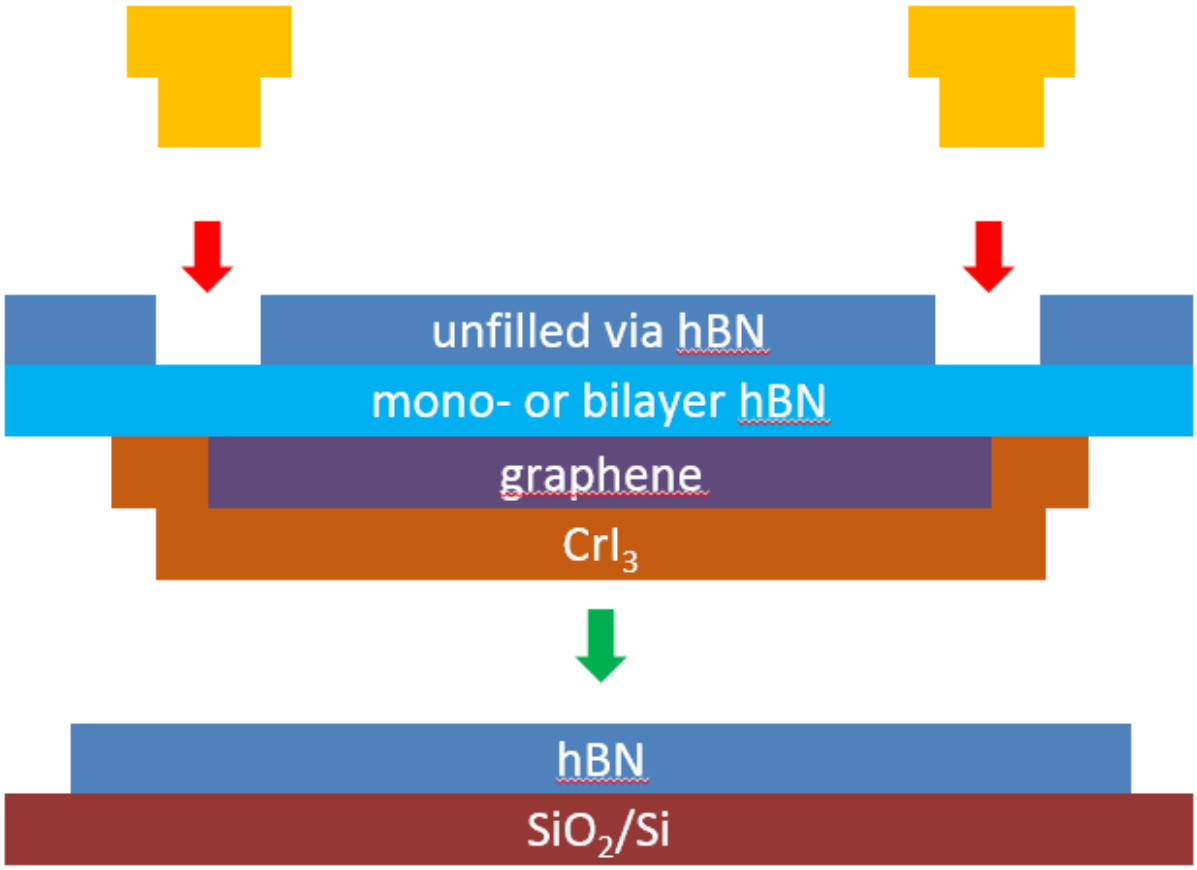

Figure 5.8: Device geometry from Method 4. Instead of depositing metal in the via hBN before assembling the stack, the pre-etched hBN is first used to pick up monolayer hBN to protect the CrI_3 underneath, then the stack is transferred onto the bottom hBN (green arrow). Metal contacts are evaporated only afterwards (red arrows).

5.7 Transport measurements

All data shown below were taken on a device fabricated using Method 1 because of the aforementioned issues with Methods 2 and 3. The device was loaded in a cryostat capable of reaching a base temperature of 1.8 K and applying a maximum out-of-plane field of 7.9 T. Two- and four-terminal measurements done before and after cooling showed that the contact resistances and intrinsic device resistances were of a reasonable magnitude. The device mobility μ was 91000 cm^2/Vs and 110000 cm^2/Vs on the hole and electron side, respectively, at base temperature. An attempt was made to observe the Dirac peak (described in Chapter 1) on a separate device made of $CrCl_3$/graphene transferred onto prepatterned electrodes prior to testing this device, but none was seen even when the graphene was gated to high voltages. This was likely due to the electrodes screening the Si back gate. The fact that a Dirac peak was observed using Method 1 nevertheless demonstrates that it is possible to preserve the mobility of graphene after placing it in direct contact with the magnet. Furthermore, the mobility of the graphene in this device was several orders of magnitude higher than in previous work by Chang et al. (where $\mu \sim 760$ cm^2/Vs). [13] Four sets of "megasweeps" were performed (two at base temperature, two at 25 K), starting at the minimum (maximum) field over the course of 13 hours per sweep, all the while varying the back gate voltage V_g between +/-10 V, corresponding to a carrier density of 7.6×10^{12} cm^{-2}. The longitudinal (R_{xx}) and Hall (R_{xy}) resistances were recorded simultaneously, and a current of 100 nA sourced through the device during all measurements. Symmetrization and antisymmetrization of R_{xx} and R_{xy} were performed on datasets with both reversed field orientations and sweep directions to account for any possible hysteresis effects associated with the magnetization of $CrCl_3$.

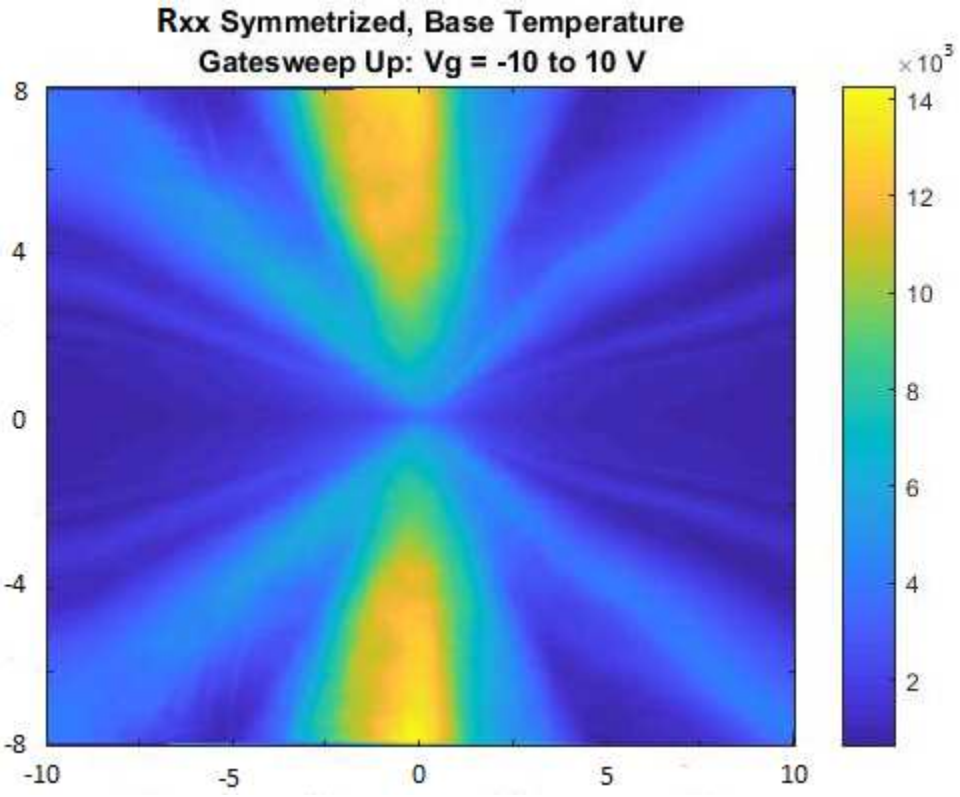

Figure 5.9: Symmetrized R_{xx} (Ω) megasweep of gate (horizontal axis) and field (vertical axis), from -10 to 10 V (left to right) and -8 to 8 T (bottom to top), respectively. The data were taken at T = 1.8 K.

Figures 5.9 and 5.10 show fan diagrams corresponding to symmetrized and antisymmetrized megasweeps in R_{xx} and R_{xy}, respectively, while Figs. 5.11 and 5.12 show line cuts of resistance versus magnetic field at gate voltages of -5, 0, and 5 V. Two phenomena are evident here: Shubnikov-de Haas oscillations and the gradual emergence of quantum Hall plateaus. Starting with the latter, quantum Hall plateaus are regions where R_{xy} remains constant with magnetic field. Occurring concurrently with the disappearance of R_{xx}, they are a physical manifestation of the alternate filling and depopulation of Landau levels – energy eigenvalues of electrons confined to two dimensions in the presence of a perpendicular magnetic field. These levels are analogous to the simple quantum harmonic oscillator, but with oscillation frequencies proportional to the magnetic field. The precise value of R_{xy} at these plateaus can be used to

calculate how many Landau levels are filled and the number of edge states present. Shubnikov-de Haas oscillations occurring in R_{xx} are a precursor to these plateaus and are found at weaker fields, before the full-fledged formation of discretized Landau levels. The presence of these oscillations in Fig. 5.11 demonstrates that the graphene was relatively free of disorder, though the absence of an unambiguous quantum Hall signal at higher external fields (defined as the aforementioned regions of zero longitudinal resistance and constant, nonzero Hall resistance) suggests that the interface between the graphene and ferromagnet may not have been ideal. Two possible reasons for this are the exposure of graphene to PMMA during lithography prior to transferring on the $CrCl_3$, as well as induced strain in the $CrCl_3$ as large parts of it were draped over the metal contacts. Either factor could also threaten the delicate, short-range exchange interaction and/or spin-orbit coupling (as mentioned in Chapter 1) that are vital to the observation of the QAHE, which demands a uniform potential across the interface.

More interesting, however, is the nonlinearity of R_{xy} near zero field, a telltale sign of the anomalous Hall effect (AHE) according to a previous study in Ref. [6] in which proximity-induced ferromagnetism was observed in graphene placed atop a ferromagnetic YIG substrate. This is shown in Fig. 5.13. Unlike the ordinary Hall effect (OHE), in which positive and negative charge carriers are segregated transverse to the direction of current flow (again with a perpendicular magnetic field), the AHE is observed only in ferromagnetic materials and shows an exaggerated segregation effect even without the external field. The underlying mechanism of the AHE is an “anomalous velocity” stemming from the Berry phase curvature in momentum space. [14]

5.8 Conclusions

While additional work remains to be done to fabricate a device that simultaneously preserves the intrinsic properties of CrI_3 against degradation in air and establishes a clean, uniform graphene/CrI_3 interface, the efforts detailed in this chapter demonstrate that such challenges can be overcome bit by bit. Initial transport measurements on even the most straightforward graphene/$CrCl_3$ device have shown signs of the anomalous Hall effect in graphene, signaling its gradual magnetization. Furthermore, the advent of novel hBN encapsulation techniques such as the use of via hBNs offers a promising route towards the eventual realization of the QAHE in graphene-ferromagnet heterostructures at temperatures heretofore unseen.

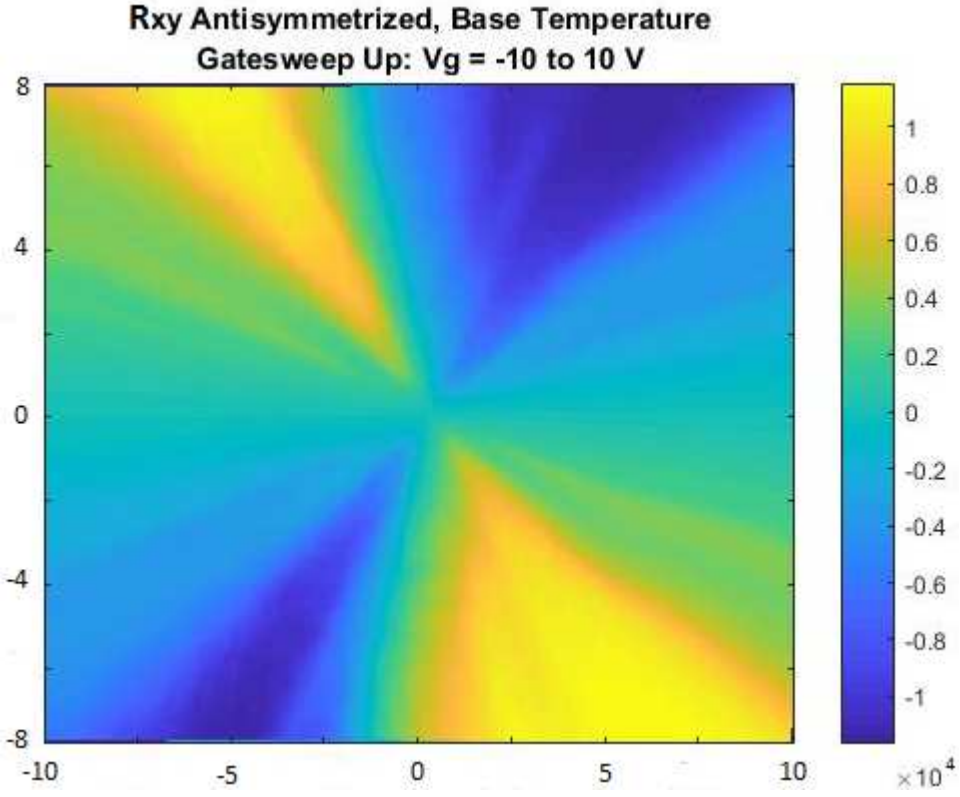

Figure 5.10: Antisymmetrized R_{xy} (Ω) megasweep of gate (horizontal axis) and field (vertical axis), from -10 to 10 V (left to right) and -8 to 8 T (bottom to top), respectively. The data were taken at T = 1.8 K.

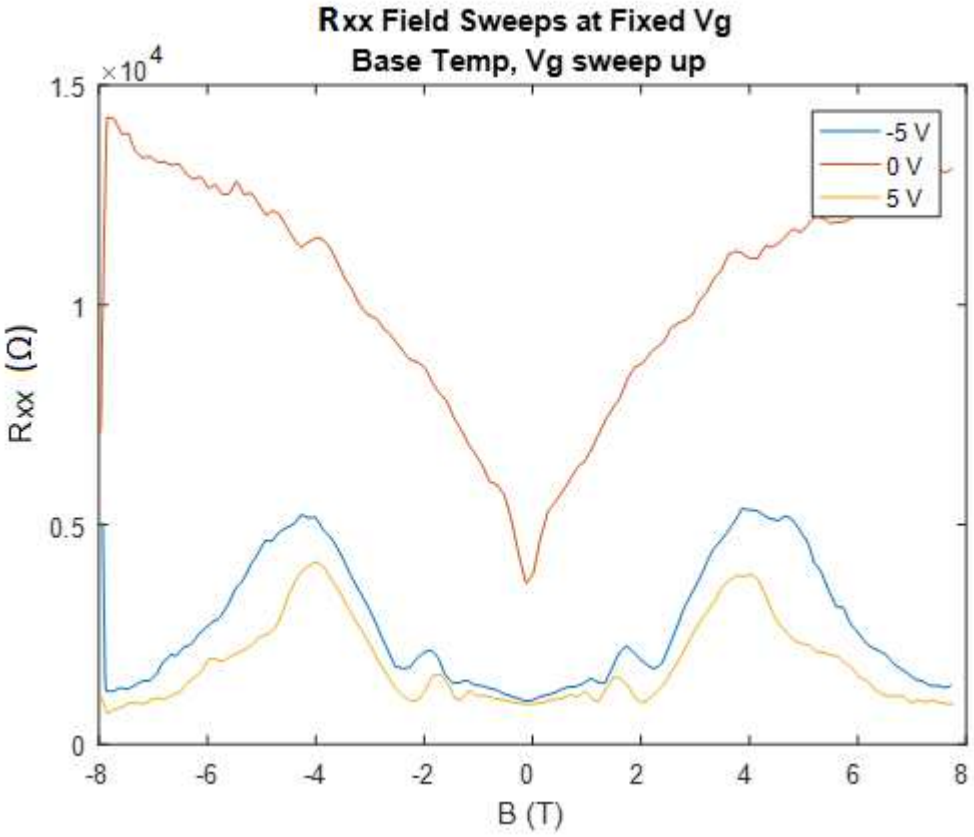

Figure 5.11: R_{xx} (Ω) as a function of applied field at V_g = -5, 0, and 5 V. Oscillations were visible on both sides. The data were taken at T = 1.8 K.

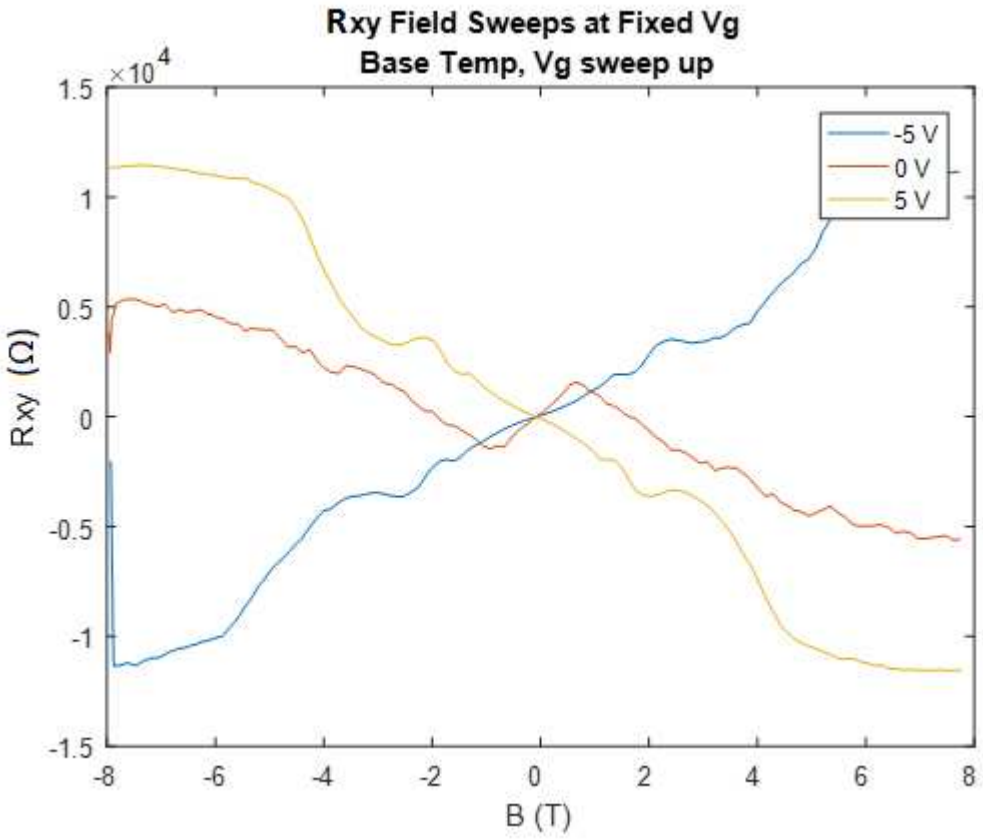

Figure 5.12: R_{xy} (Ω) as a function of applied field at V_g = -5, 0, and 5 V. Quantum Hall plateaus began to develop around B = ±4-5 T. The data were taken at T = 1.8 K.

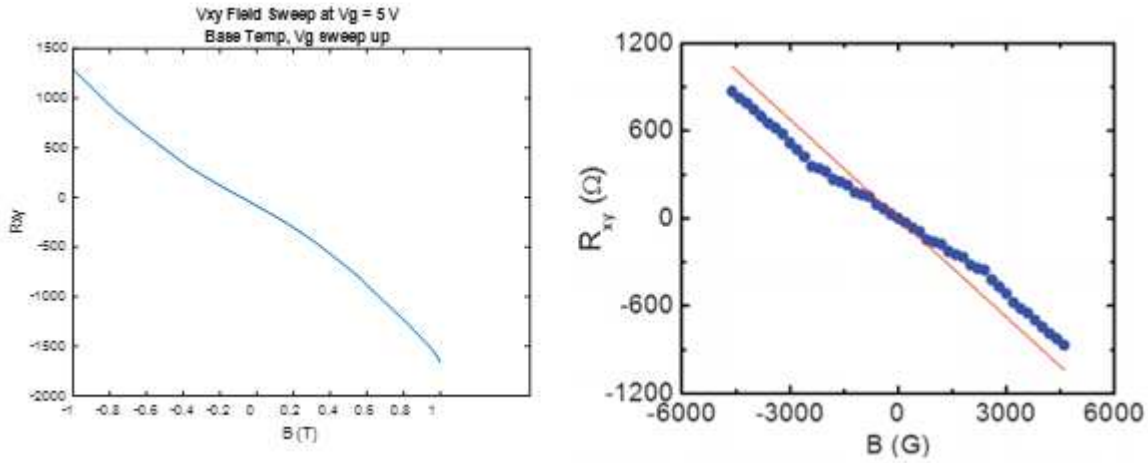

Figure 5.13: Low-field nonlinearity in R_{xy} for graphene/$CrCl_3$ system (left) compared to nonlinearity in R_{xy} for graphene/YIG system (right, with red line denoting ordinary Hall signal). The right figure was reproduced from Ref. [6].

5.9 References

1. Kikkawa, J. M., et al. "Optical studies of locally implanted magnetic ions in GaAs." *Physical Review B* 50.3 (1994): 2003.
2. Smorchkova, I. P., et al. "Spin transport and localization in a magnetic two-dimensional electron gas." *Physical Review Letters* 78.18 (1997): 3571.
3. Haury, A., et al. "Observation of a ferromagnetic transition induced by two-dimensional hole gas in modulation-doped CdMnTe quantum wells." *Physical Review Letters* 79.3 (1997): 511.
4. Kikkawa, J. M., et al. "Room-temperature spin memory in two-dimensional electron gases." *Science* 277.5330 (1997): 1284-1287.
5. Smorchkova, I. P., et al. "Giant magnetoresistance and quantum phase transitions in strongly localized magnetic two-dimensional electron gases." *Physical Review B* 58.8 (1998): R4238.
6. Wang, Zhiyong, et al. "Proximity-induced ferromagnetism in graphene revealed by the anomalous Hall effect." *Physical Review Letters* 114.1 (2015): 016603.
7. Tang, Chi, et al. "Approaching quantum anomalous Hall effect in proximity-coupled YIG/graphene/h-BN sandwich structure." *APL Materials* 6.2 (2018): 026401.
8. Wei, Peng, et al. "Strong interfacial exchange field in the graphene/EuS heterostructure." *Nature Materials* 15.7 (2016): 711.
9. Zhang, Jiayong, et al. "Robust quantum anomalous Hall effect in graphene-based van der Waals heterostructures." *Physical Review B* 92.16 (2015): 165418.
10. Qiao, Zhenhua, et al. "Quantum anomalous Hall effect in graphene proximity coupled to an antiferromagnetic insulator." *Physical Review Letters* 112.11 (2014): 116404.

11. Qiao, Zhenhua, et al. "Quantum anomalous Hall effect in graphene from Rashba and exchange effects." *Physical Review B* 82.16 (2010): 161414.
12. Oh, Seongshik. "The complete quantum Hall trio." *Science* 340.6129 (2013): 153-154.
13. Chang, Cui-Zu, et al. "Experimental observation of the quantum anomalous Hall effect in a magnetic topological insulator." *Science* (2013): 1232003.
14. Weng, Hongming, et al. "Quantum anomalous Hall effect and related topological electronic states." *Advances in Physics* 64.3 (2015): 227-282.
15. Wang, L., et al. "One-dimensional electrical contact to a two-dimensional material." *Science* 342.6158 (2013): 614-617.
16. Telford, Evan J., et al. "Via Method for Lithography Free Contact and Preservation of 2D Materials." *Nano Letters* 18.2 (2018): 1416-1420.
17. Lado, Jose L., and Joaquín Fernández-Rossier. "On the origin of magnetic anisotropy in two dimensional CrI_3." *2D Materials* 4.3 (2017): 035002.
18. Huang, Bevin, et al. "Layer-dependent ferromagnetism in a van der Waals crystal down to the monolayer limit." *Nature* 546.7657 (2017): 270.
19. Klein, Dahlia R., et al. "Probing magnetism in 2D van der Waals crystalline insulators via electron tunneling." *arXiv preprint arXiv:1801.10075* (2018).
20. Song, Tiancheng, et al. "Giant tunneling magnetoresistance in spin-filter van der Waals heterostructures." *arXiv preprint arXiv:1801.08679* (2018).
21. Wang, Zhe, et al. "Very Large Tunneling Magnetoresistance in Layered Magnetic Semiconductor CrI_3." *arXiv preprint arXiv:1801.08188* (2018).
22. Kim, Hyun Ho, et al. "One million percent tunnel magnetoresistance in a magnetic van der Waals heterostructure." *arXiv preprint arXiv:1804.00028* (2018).

23. Lee, Gwan-Hyoung, et al. "Electron tunneling through atomically flat and ultrathin hexagonal boron nitride." *Applied Physics Letters* 99.24 (2011): 243114.
24. Britnell, Liam, et al. "Electron tunneling through ultrathin boron nitride crystalline barriers." *Nano Letters* 12.3 (2012): 1707-1710.

Chapter 6

Other work and future directions

6.1 Motivation

The use of Raman spectroscopy to characterize layer thickness in 2-D samples has proved to be fruitful in numerous studies ever since it was used to fingerprint monolayer graphene. [1-4] This is natural given the unique properties, optical and otherwise, that distinguish the monolayer form of these materials from their thicker counterparts. Monolayers of $ZrTe_5$ and 1T'-$MoTe_2$, for example, were theoretically predicted to be quantum spin Hall insulators [5, 6], while $CrSiTe_3$ and $CrCl_3$ were candidates for studying magnetism down to the monolayer [7-11], a topic that was thoroughly debated until the phenomenon was confirmed by a magneto-optical Kerr effect (MOKE) study [12]. This chapter serves two purposes. First, it will summarize efforts to characterize monolayers of these four materials and, in keeping with the overall theme of this thesis, highlight the importance of preserving their structural integrity by either performing the studies in an inert environment or encapsulating them with hBN to prevent unwanted exposure to air. Second, it will recapitulate the current status of ongoing projects and provide possible routes for future work.

6.2 Raman study of thin $ZrTe_5$

$ZrTe_5$ was the first of the four materials to be investigated. Citing a computational study claiming that its interlayer coupling is comparable to that of graphite [6], it was thinned down via micromechanical exfoliation and examined by Raman spectroscopy. The uniaxial nature of bulk $ZrTe_5$ carried over to its thinner forms, and it was often the case that the laser spot (~1 μm^2) was

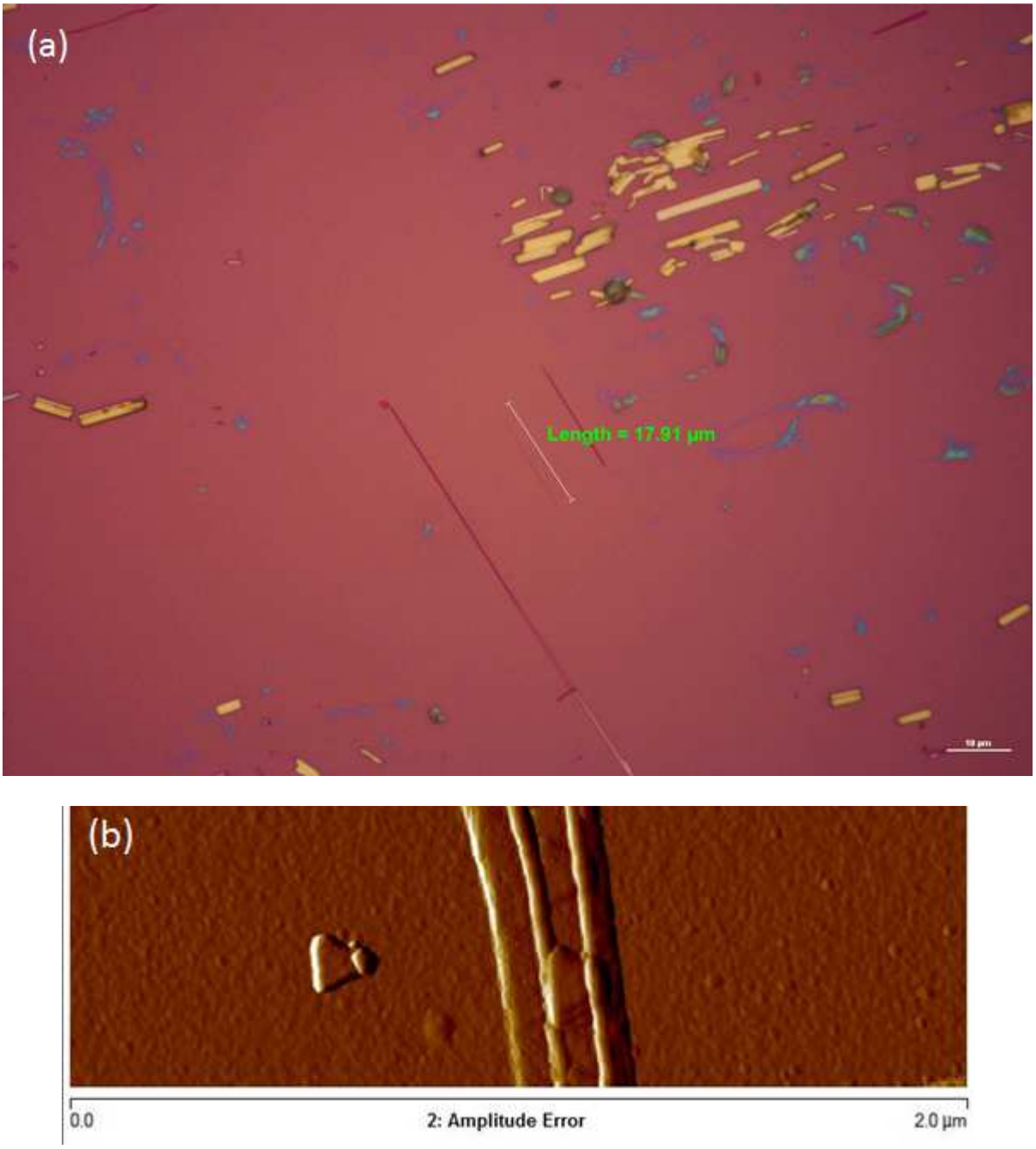

Figure 6.1: 100× optical micrograph (a) and AFM image (~0.6 µm × 2 µm) (b) of representative $ZrTe_5$ flakes. The sample height in (b) varied between 5-15 nm.

wider than the sample itself. Moreover, optical and AFM images revealed that it does not cleave uniformly, with a single AFM (~0.6 µm × 2 µm) scan showing heights ranging from 5-15 nm (a unit cell is roughly 1.4 nm thick, so this corresponds to a minimum of roughly 3-4 layers). Some

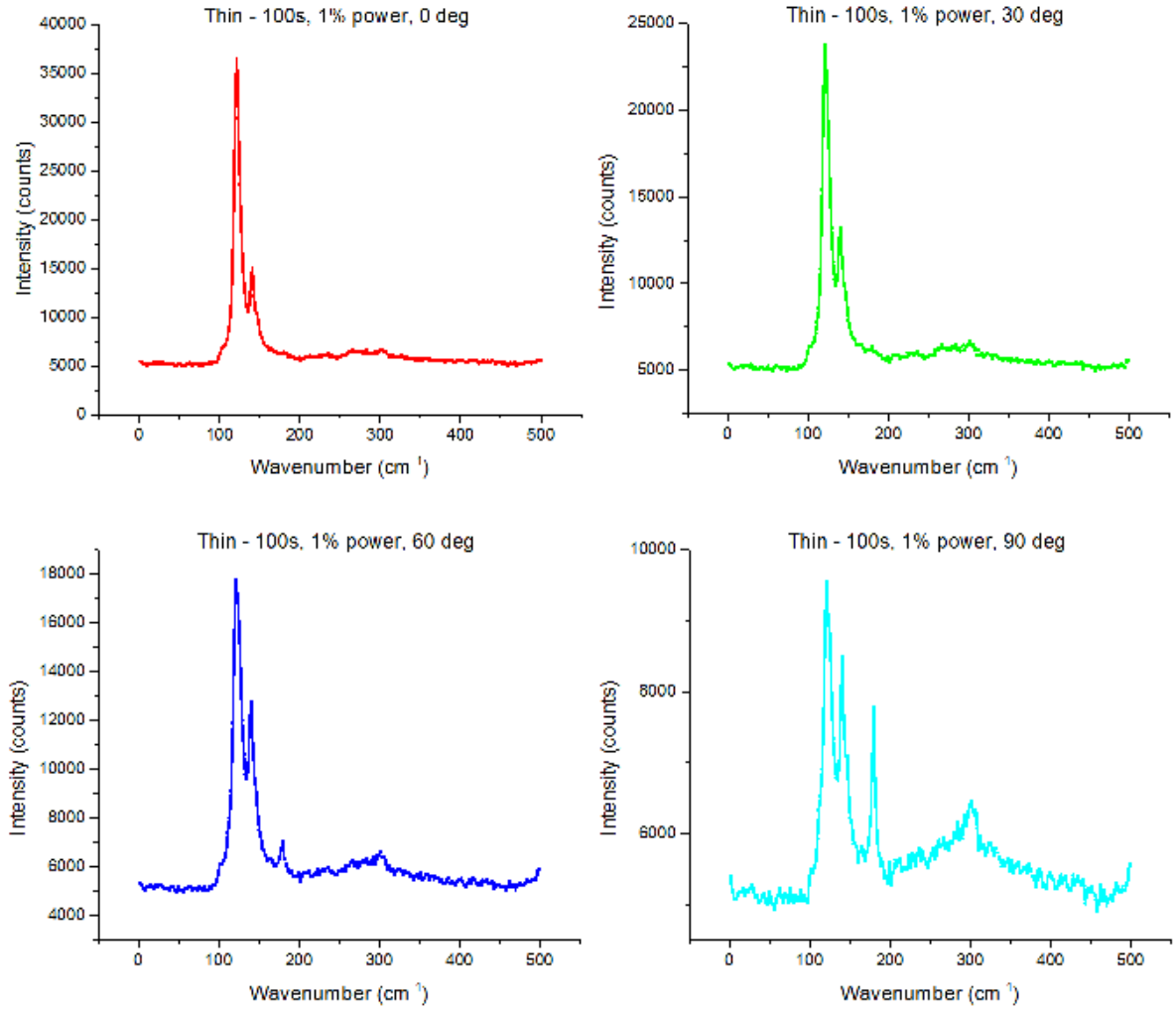

Figure 6.2: Raman spectra showing polarization dependence of a thin $ZrTe_5$ sample whose *a*-axis was rotated between 0 and 90° relative to the polarization of the incident beam. The data were acquired with an incident laser power of 270 μW over 100 s using a 532 nm laser.

representative images are shown in Fig. 6.1. All optical measurements on $ZrTe_5$ were performed on a Renishaw InVia micro-Raman system at an excitation wavelength of 532 nm (green). While the initial plan was to determine sample thickness by comparing the height of $ZrTe_5$ Raman peaks to that of the bare SiO_2/Si substrate, the fact that thinner samples were not uniform even within the area occupied by the laser spot (which was, again, wider than the samples themselves) posed significant challenges in terms of repeatable beam alignment, obfuscating meaningful

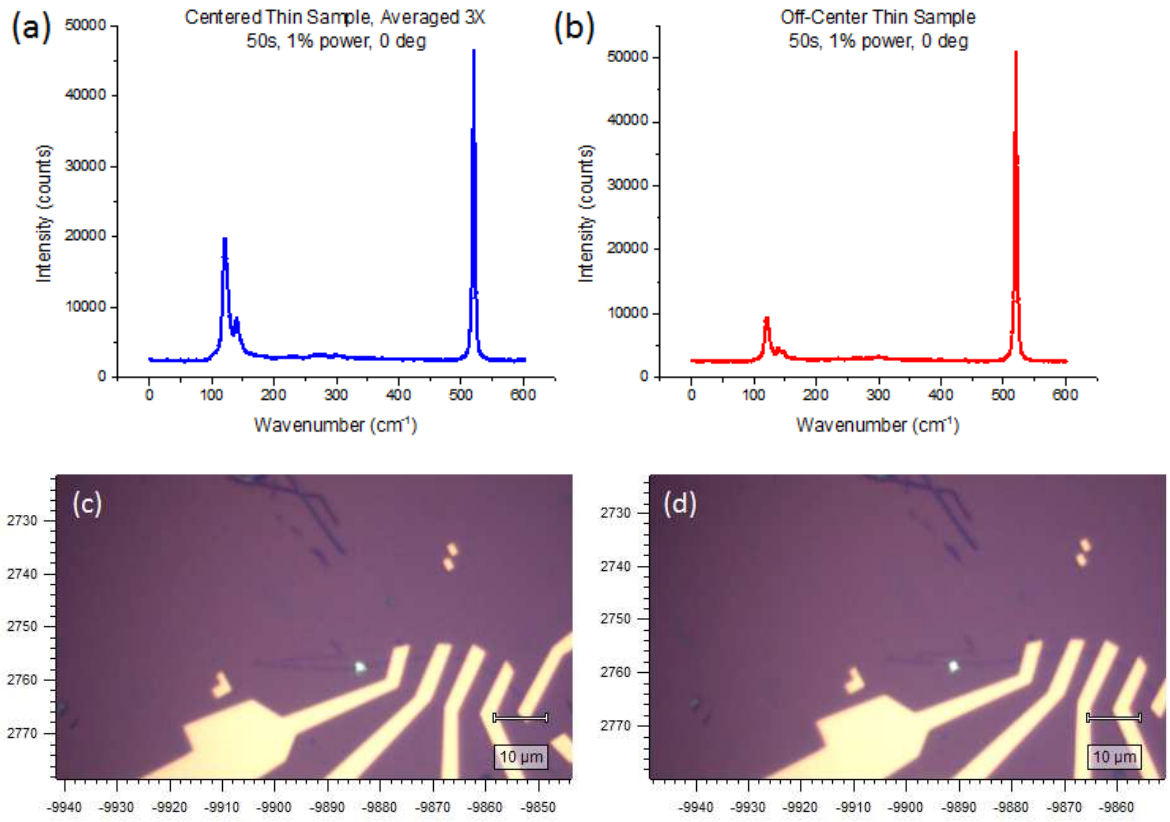

Figure 6.3: Raman spectra (a, b) and corresponding optical micrographs (c, d) of thin $ZrTe_5$ where the laser spot was centered (a, c) and slightly off-center (b, d). The data were acquired with an incident laser power of 270 µW over 50 s using a 532 nm laser.

conclusions to this end. Nevertheless, the compound exhibited a clear polarization dependence, with an A_g mode near 180 cm^{-1} strengthening as the *a*-axis of the sample was gradually rotated from 0 to 90° with respect to the incident laser polarization (all polarizations were analyzed); this is demonstrated in Fig. 6.2. [13] This finding underscored the structural anisotropy of $ZrTe_5$, so in subsequent runs extra care was taken to reorient the sample to the same angle after every measurement for consistency. Lateral movement of the sample relative to the beam, however, was unavoidable, as shown by the differing spectra between on-sample and even slightly off-sample measurements in Fig. 6.3a-b. Figure 6.3c-d show the corresponding optical micrographs.

It was also found that the intensities of the first and second $ZrTe_5$ Raman peaks (located at ~121 and 140 cm^{-1}) relative to the third differed from findings in the literature, suggesting possible degradation in air and motivating encapsulation by hBN for later studies. [13]

6.3 Raman study of thin 1T'-$MoTe_2$

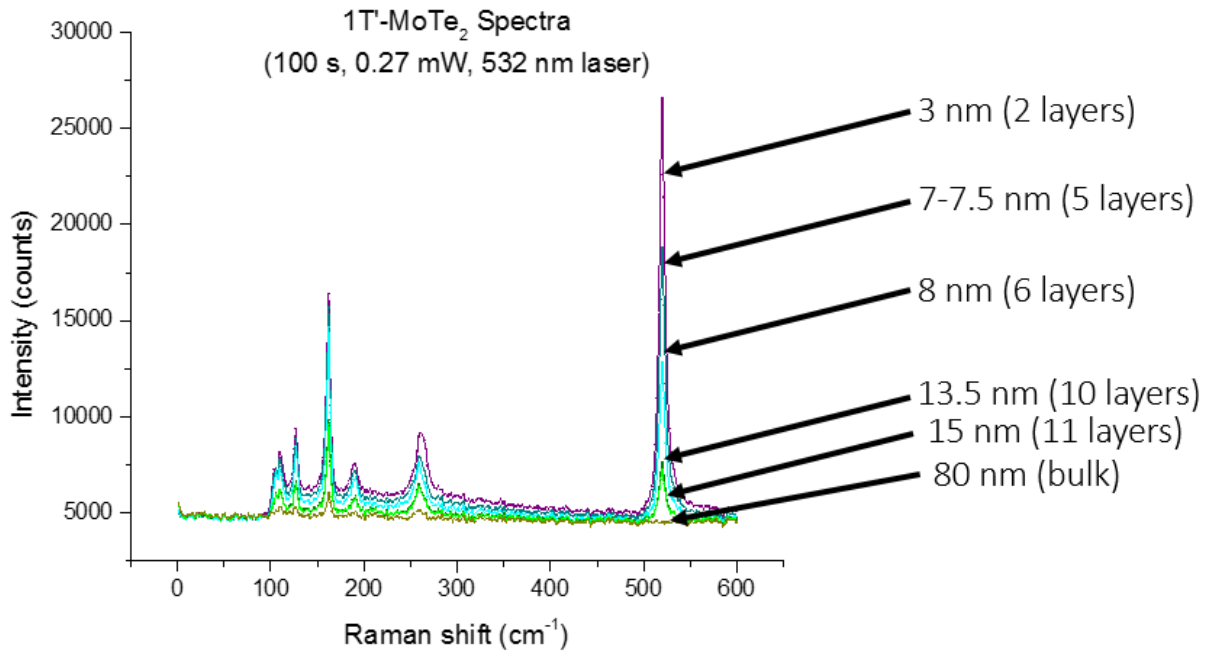

Figure 6.4: Raman spectra of unencapsulated 1T'-$MoTe_2$ showing thickness dependence. The data were acquired with an incident laser power of 270 μW over 100 s using a 532 nm laser.

The same set of measurements were repeated on 1T'-$MoTe_2$ on SiO_2/Si, beginning with unencapsulated samples ranging from 3 to 80 nm, which correspond to bilayer to bulk flakes. A total of six modes at energies above 100 cm^{-1}, the approximate cutoff from the edge filter, were observed in this case – 4 more than were found experimentally in Ref. [14], though many of the modes were predicted by density functional theory (DFT) in the same publication. These spectra

are shown in Fig. 6.4 along with their respective thicknesses and layer numbers. Table 6.1 lists the peaks found in this experiment next to those predicted by DFT.

Peak position (cm^{-1})	Mode type (from DFT)
104.5	B_g
109	A_g
127	A_g
162	A_g or B_g
190	? (*)
260	A_g

Wavenumber (cm^{-1})	Mode type (from DFT)
73.75	B_g
80.41	A_g
101.01	B_g
111.27	A_g
125.69	A_g
161.10	A_g
162.52	B_g
254.58	A_g
269.22	A_g

Table 6.1: Locations of observed $MoTe_2$ Raman peaks (left) and comparison to predicted modes and their classification from DFT (right; reproduced from Ref. [14]). (*) refers to a mode also observed in Ref. [17] but not predicted by Ref. [14].

Two patterns emerged upon analyzing the peak intensity of the strongest $MoTe_2$ mode (at 161 cm^{-1}) and the underlying Si mode (at 520 cm^{-1}) as a function of sample thickness. First, the intensity of the selected $MoTe_2$ peak decreased with increasing sample thickness. Second, the intensity of the Si peak also decreased with increasing sample thickness, but at a faster rate. Ignoring reflection for the moment, the Raman scattering strength R_{MoTe2} varies as

$$R_{MoTe_2} \propto \left|\chi_{MoTe_2}\right|^2 P_{inc} \frac{1 - e^{-(\alpha_1+\alpha_2)L}}{\alpha_1 + \alpha_2}$$

where χ is the susceptibility of the material, P_{inc} is the incident laser power, α_i's are the absorption coefficient for the incoming and reflected beams, and L is the sample thickness. Similarly, the scattering strength of the Si Raman peak R_{Si} varies as

$$R_{Si} \propto |\chi_{Si}|^2 P_{inc} \frac{e^{-(\alpha_1+\alpha_2')L}}{\alpha_1^{Si}+\alpha_2^{Si}}.$$

In the following analysis, it is assumed that the susceptibility may be independent of L, the scattering efficiency is much weaker than the absorption, and $\alpha_1 = \alpha_2 = \alpha_2' = \alpha$. Experimentally, the absorption coefficient of $MoTe_2$ nanosheets at 532 nm was determined to be ~1 cm^{-1}. [15] Theoretically, R_{MoTe2} should increase with L provided that α and χ_{MoTe2} are independent of L and the wavelength λ. Furthermore, if αL≪1 for all α, then R_{MoTe2} should be

Sample thickness from AFM (nm)	Intensity (counts) of 161 cm^{-1} $MoTe_2$ mode	Intensity (counts) of 520 cm^{-1} Si mode	$\frac{R_{MoTe_2}}{R_{Si}}$
3	10,427	21,690	0.48
7-7.5	10,049	14,077	0.71
8	9,210	8,240	1.11
13.5	4,719	3,027	1.56
15	4,540	2,498	1.82
80	1,204	~0	∞

DECREASE (161 cm^{-1} $MoTe_2$ mode)

DECREASE (520 cm^{-1} Si mode)

Table 6.2: Absolute intensity of strongest $MoTe_2$ peak versus that of Si peak (including their ratios) for various flake thicknesses.

proportional to L. Neither of these predictions held true according to the intensity analysis in Table 6.2. However, R_{Si} vanished with increasing L as expected. Taking the ratio of the previous two equations yields

$$\frac{R_{MoTe_2}}{R_{Si}} \propto \frac{|\chi_{MoTe_2}|^2}{|\chi_{Si}|^2} \frac{\alpha_{Si}}{\alpha_{MoTe_2}} (e^{2\alpha_{MoTe_2}L} - 1).$$

If αL≪1, then this ratio is proportional to L, which was approximately seen. However, R_{Si} decreased with L, indicating that either 1. αL>1 such that χ and α depend on thickness in a way that makes it scale as L (with α~0.18/nm), or 2. The effect of reflection is dominant, increasing

with increasing thickness. Plots of the absolute intensities of $MoTe_2$ and Si peaks, as well as their ratio, are shown in Fig. 6.5. Figure 6.6 contains an optical image of a $MoTe_2$ sample with multiple thicknesses, encapsulated by hBN, and Fig. 6.7 shows Raman spectra for different regions. While the Raman peaks looked similar to those in unencapsulated samples, evidently this did not hold true at all temperatures as the sample (called Sample 1 in Chapter 3) showed severe degradation upon heating.

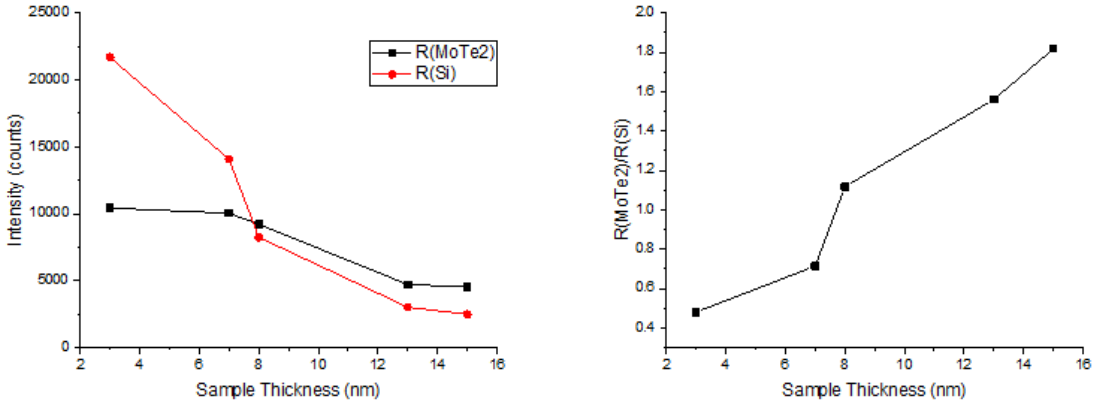

Figure 6.5: Plot of absolute intensities of strongest $MoTe_2$ and Si peaks versus sample thickness (left), and their ratio versus sample thickness (right).

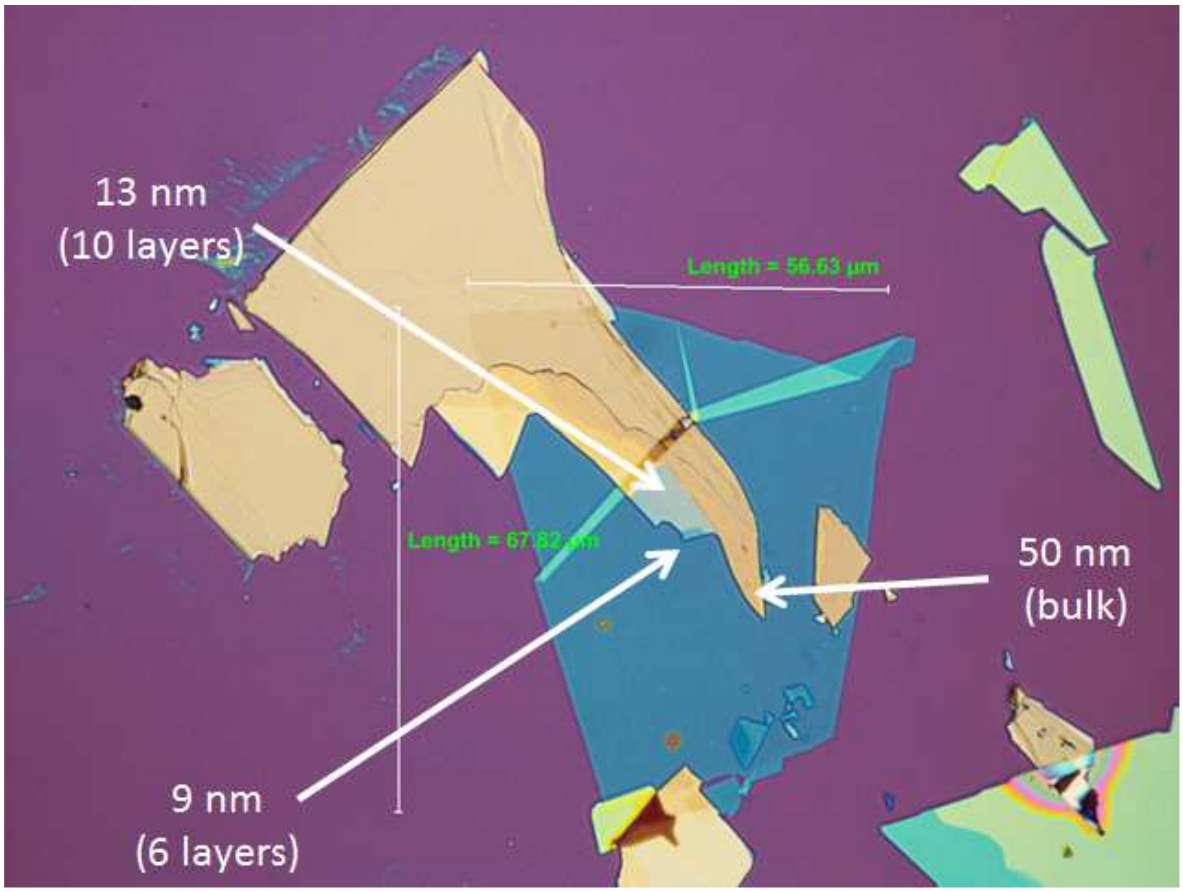

Figure 6.6: Optical micrograph of encapsulated $MoTe_2$ sample with multiple thicknesses. The hBN is approximately 20 nm thick.

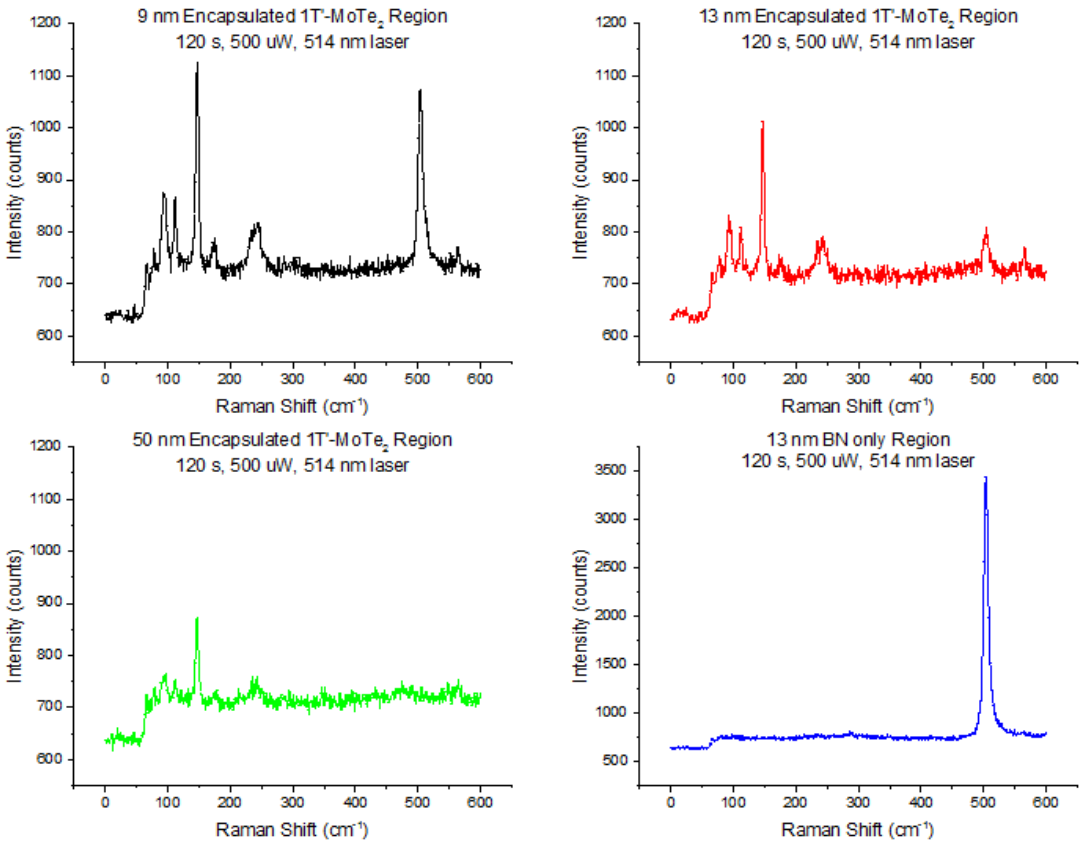

Figure 6.7: Raman spectra of different encapsulated regions of sample in Fig. 6.6. The data were acquired with an incident laser power of 500 μW over 120 s using a 514 nm laser.

6.4 Raman study of thin $CrSiTe_3$

The final set of Raman measurements focused on two layered materials that are ferromagnetic in the bulk, $CrSiTe_3$ and $CrCl_3$. Preliminary data taken on ultrathin, unencapsulated samples of the former showed virtually no signal besides the standard Si peak at 520 cm^{-1} originating from the substrate. As proved in Chapter 3, thermal degradation is also of great concern when dealing with tellurium-based compounds, which have a tendency to break down into tellurium nanocrystals at sufficiently high temperatures.

Keeping these points in mind, bulk crystals of $CrSiTe_3$ were moved to and exfoliated in a N_2-filled glovebox, then encapsulated by hBN using a polymer-free technique. The idea behind this was that transfers performed using polymers such as PPC require heating up to 85 °C in air (or 120 °C in the glovebox, where there is minimal moisture), and it was best to avoid this if at all possible. Instead, hBN was exfoliated directly onto PDMS, which was subsequently cut into smaller squares and stamped directly onto the desired flake of $CrSiTe_3$. Presumably, the van der Waals adhesion between hBN and the PDMS is not as strong as with another layered materials

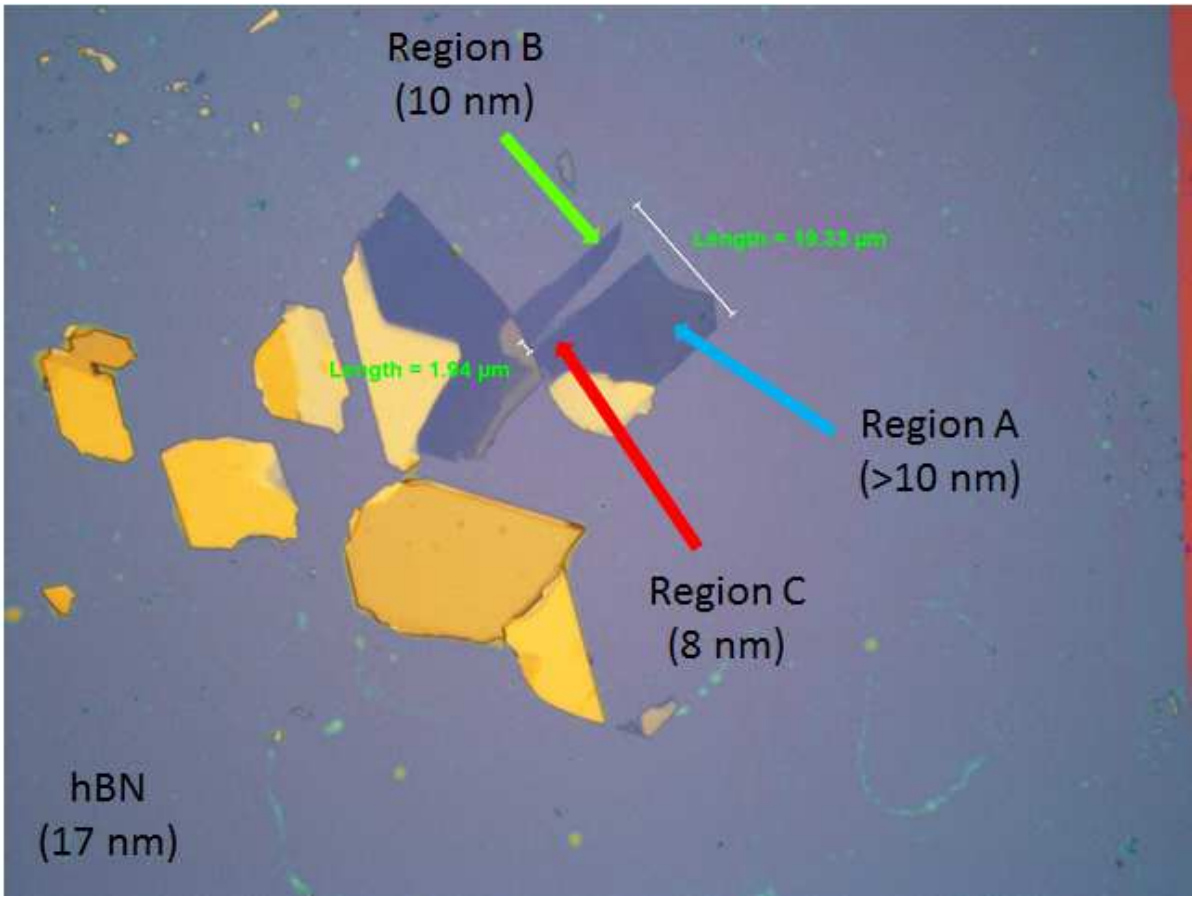

Figure 6.8: Optical micrograph of encapsulated $CrSiTe_3$ sample, with hBN covering all but the far right edge. Regions A, B, and C were probed. The sample was encapsulated using a polymer-free technique.

and the SiO_2/Si substrate. Shown in Fig. 6.8 is an optical image of a $CrSiTe_3$ sample encapsulated in this manner.

Three areas of different thicknesses on the sample were probed, labelled Regions A, B, and C. To ensure that hBN encapsulation was actually effective, three sets of spectra were acquired for each thickness, all using the Horiba micro-Raman system inside the glovebox: before encapsulation, immediately after encapsulation (but before removing from the glovebox), and 1.5 hours after encapsulation (during which time the sample was removed from the glovebox

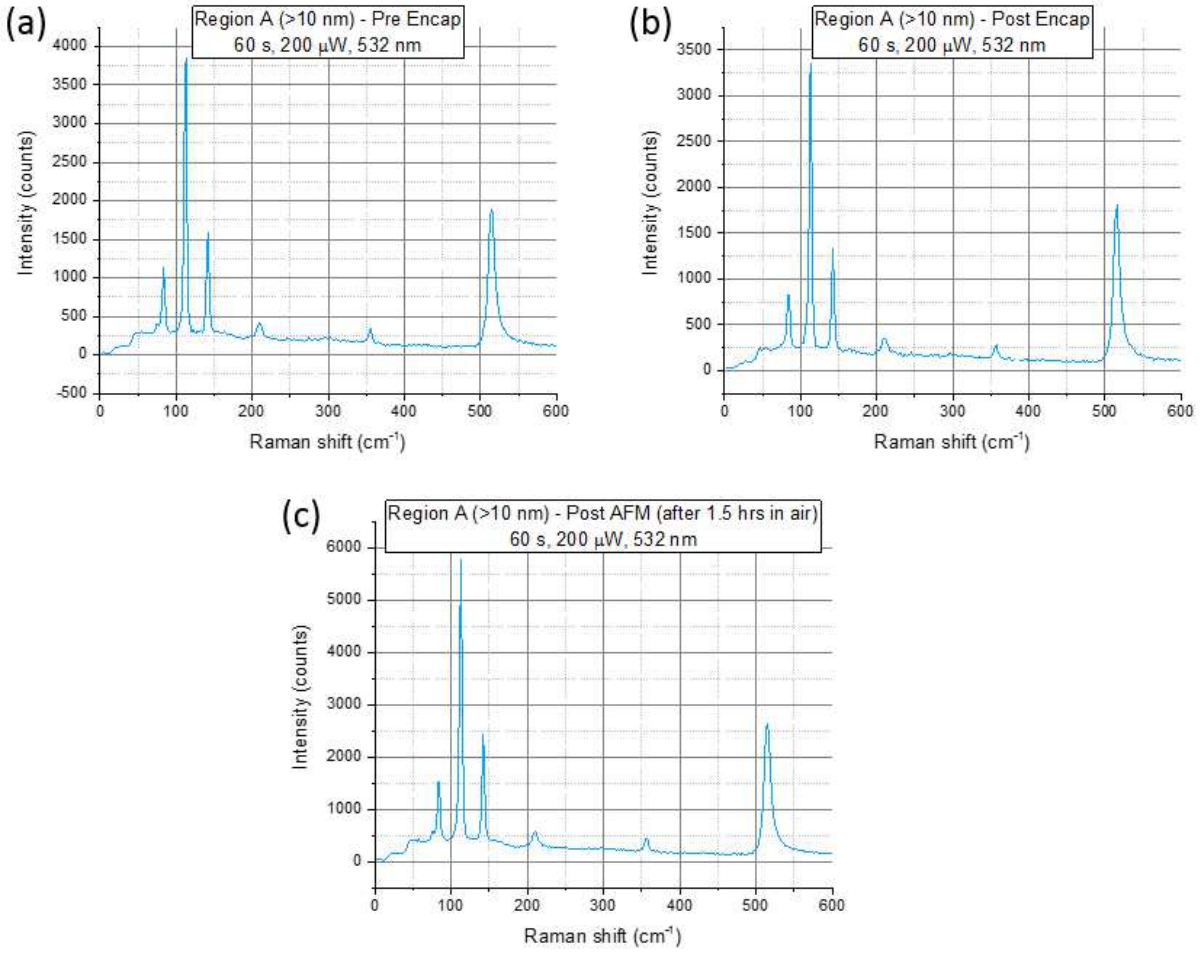

Figure 6.9: Raman spectra of Region A (>10 nm) (a) before, (b) immediately after, and (c) 1.5 hours after encapsulation. The encapsulated $CrSiTe_3$ was exposed to air in (c). The data were acquired with an incident laser power of 200 μW over 60 s using a 532 nm laser.

and AFM'ed in air). The results are shown in Figs. 6.9-6.11, where (a), (b), and (c) were taken in sequential order. Although no noticeable changes were detected in the Raman spectrum of Region A (>10 nm) after removal from the glovebox, this was not the case for the two thinner regions, Regions B (10 nm) and C (8 nm). In particular, both developed an additional "shoulder" around 153-155 cm^{-1}, highlighted by purple arrows in Figs. 6.10c and 6.11c. These indicate that irreversible changes, oxidation for instance, had occurred in the sample, and thus encapsulation alone was not enough to protect it.

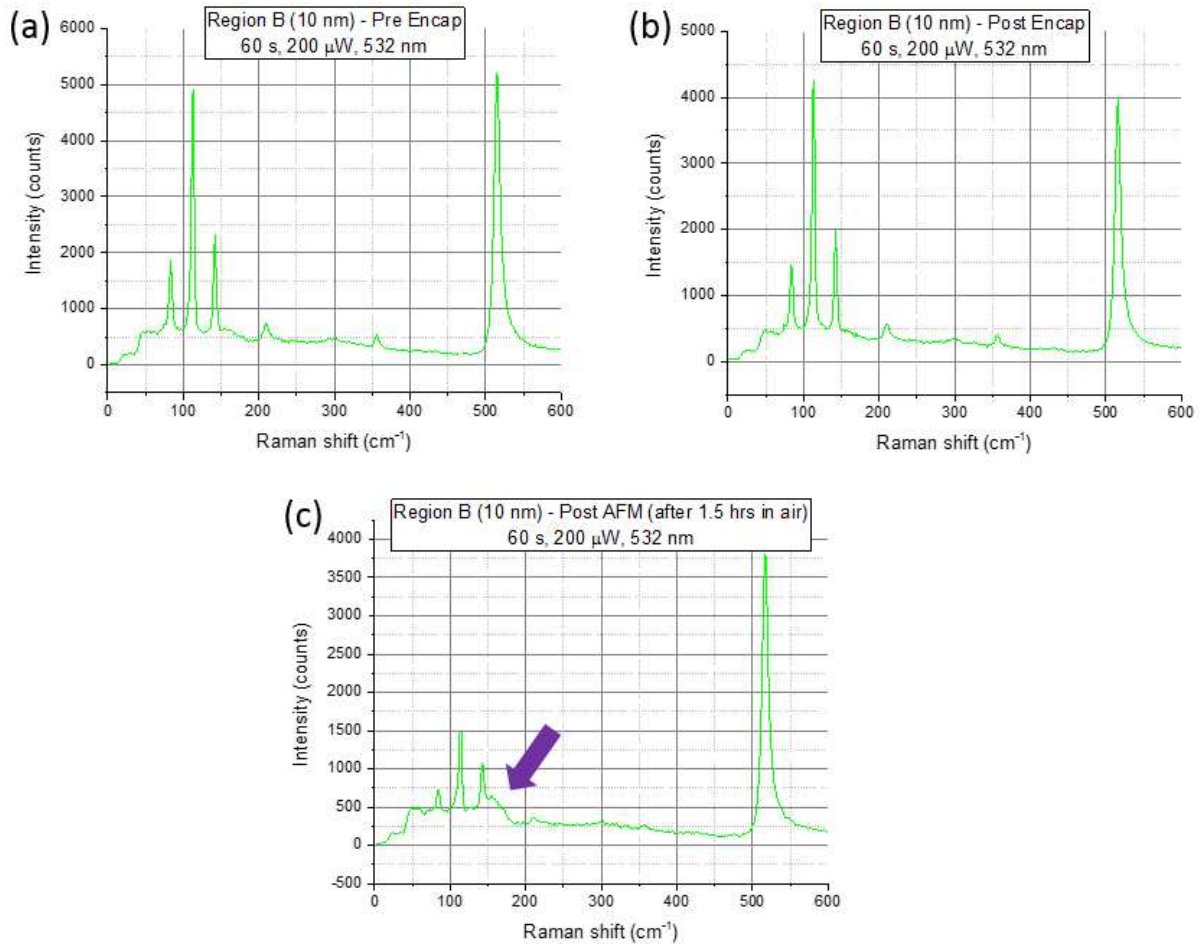

Figure 6.10: Raman spectra of Region B (10 nm) (a) before, (b) immediately after, and (c) 1.5 hours after encapsulation. The encapsulated $CrSiTe_3$ was exposed to air in (c). The purple arrow points to a shoulder-like feature indicating irreversible change in the sample. The data were acquired with an incident laser power of 200 µW over 60 s using a 532 nm laser.

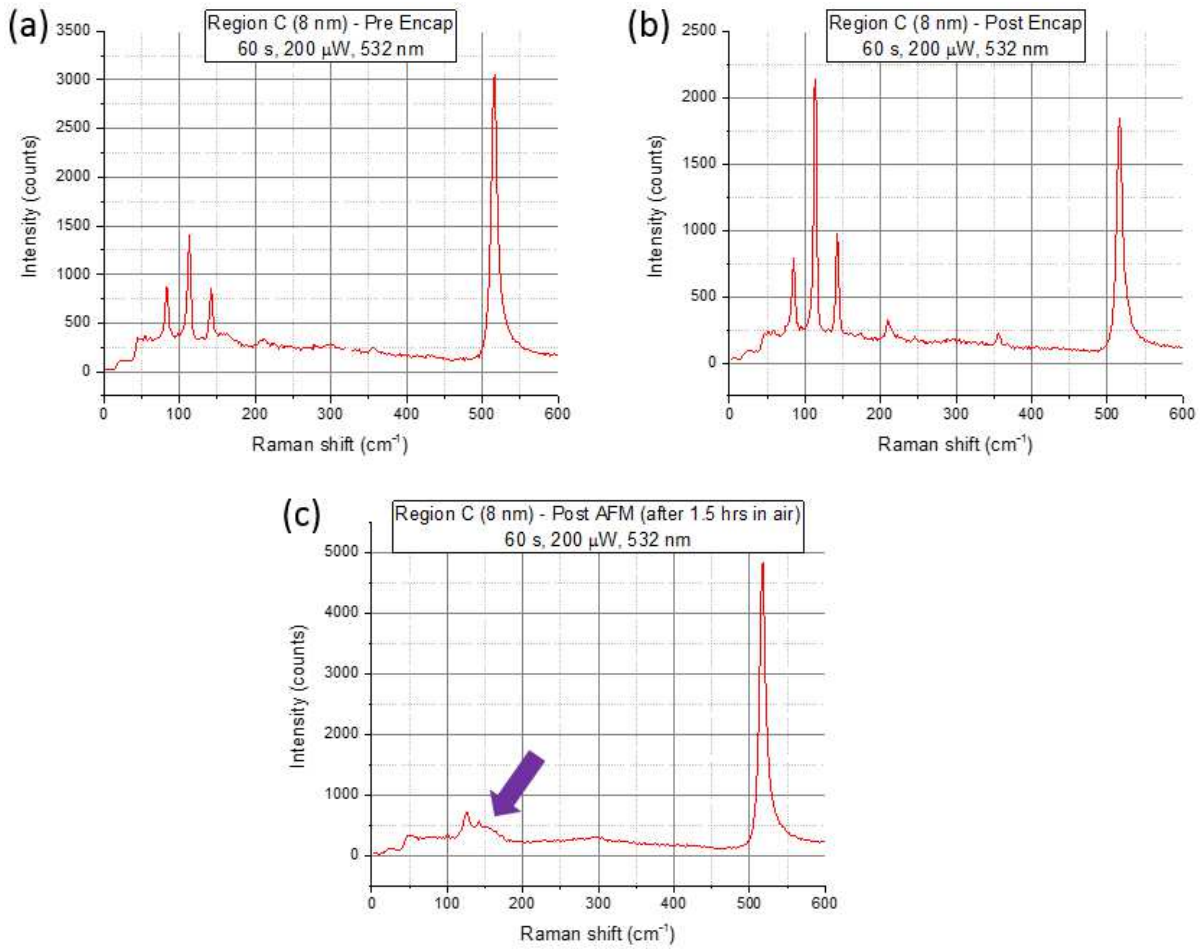

Figure 6.11: Raman spectra of Region C (8 nm) (a) before, (b) immediately after, and (c) 1.5 hours after encapsulation. The encapsulated $CrSiTe_3$ was exposed to air in (c). The purple arrow points to a shoulder-like feature indicating irreversible change in the sample. The data were acquired with an incident laser power of 200 μW over 60 s using a 532 nm laser.

6.5 Raman study of thin $CrCl_3$

The Raman peaks of $CrCl_3$ were found to be much weaker than those of $CrSiTe_3$ for a given sample thickness, prompting an increase in acquisition times. As demonstrated in Figs. 6.9-6.11, encapsulating samples with hBN without removing them from the glovebox does not affect their Raman spectra, hence data for $CrCl_3$ was only collected before encapsulation and after encapsulation (followed by exposure to air, this time for 3.5 hours). Optical images of the three

probed regions, spread over two samples, are shown in Fig. 6.12. The 1 nm region is a monolayer, the 2 nm region a bilayer, and the 26-27 nm region effectively bulk. The corresponding Raman spectra are shown in Figs. 6.13-6.15. The Raman spectrum of SiO_2/Si is provided in Fig. 6.16 for reference. Unlike $CrSiTe_3$, encapsulated $CrCl_3$ did not show signs of

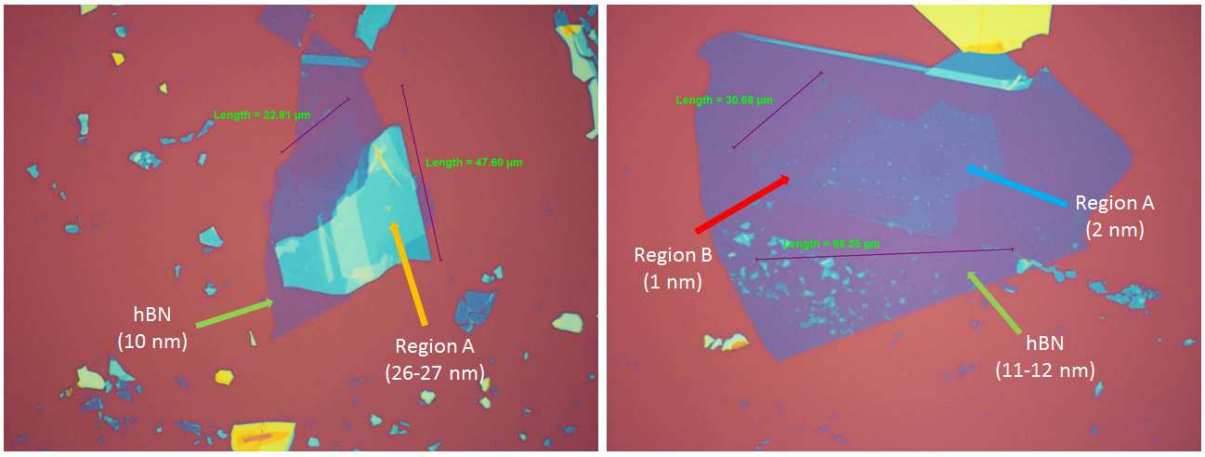

Figure 6.12: Optical micrographs of encapsulated $CrCl_3$ samples. Region A (left, 26-27 nm thick) and Regions A and B (right, 2 and 1 nm, respectively) were probed. The sample was encapsulated using a polymer-free technique.

degradation after removal from the glovebox, as evidenced by its relatively unchanged features (in particular, the already weak peak at 200 cm^{-1}) before and after encapsulation. However, the lack of strong Raman peaks to begin with for the monolayer and bilayer $CrCl_3$ regions made them difficult to characterize, if at all possible. This was especially true for the monolayer case, where a peak may well have overlapped with a weak Si peak at 300 cm^{-1} according to the literature. [16]

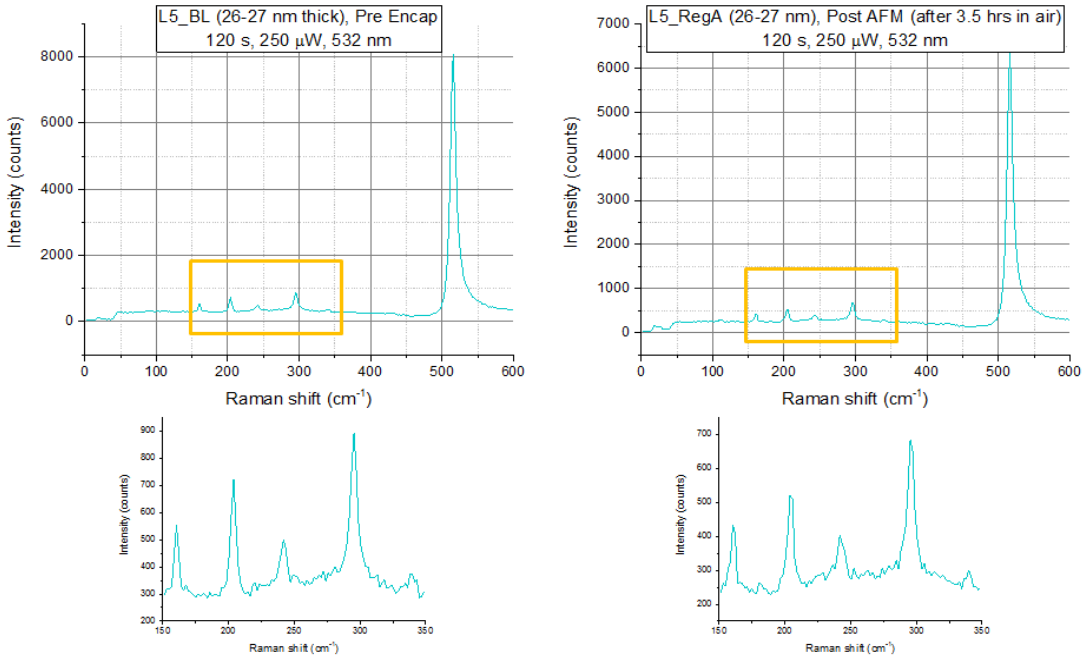

Figure 6.13: Raman spectra of the 26-27 nm thick region of $CrCl_3$ before encapsulation (left) and after exposing it to air for 3.5 hours post-encapsulation (right). The data were acquired with an incident laser power of 250 µW over 120 s using a 532 nm laser. The boxed yellow area is enlarged below.

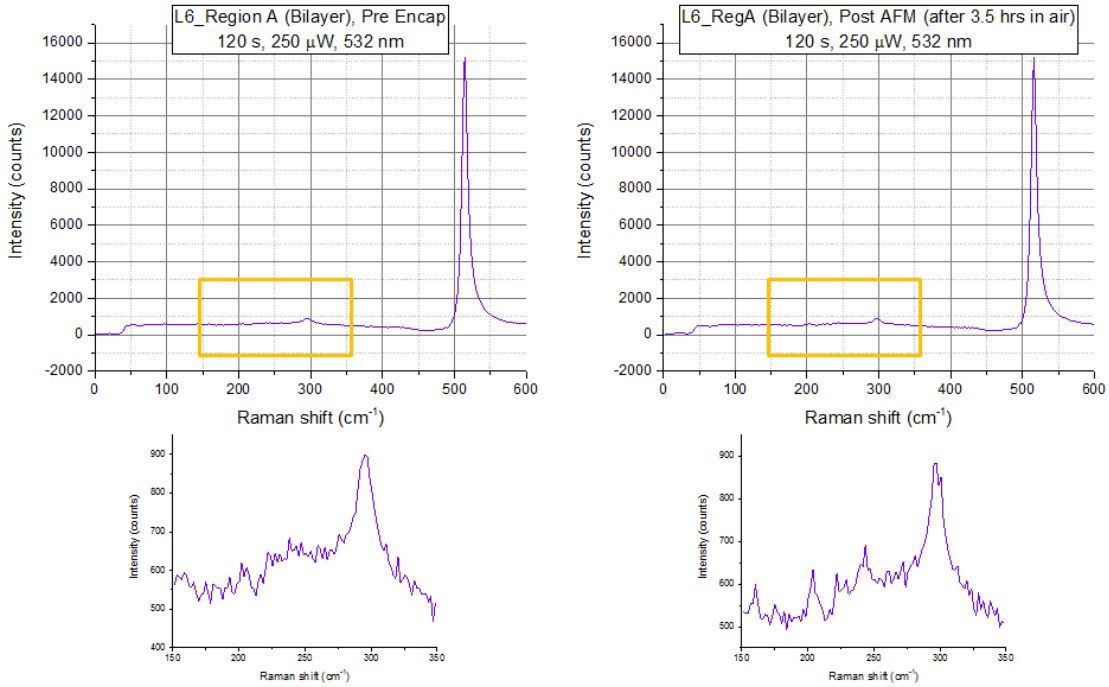

Figure 6.14: Raman spectra of the 2 nm (bilayer) region of $CrCl_3$ before encapsulation (left) and after exposing it to air for 3.5 hours post-encapsulation (right). The data were acquired with an incident laser power of 250 µW over 120 s using a 532 nm laser. The boxed yellow area is enlarged below.

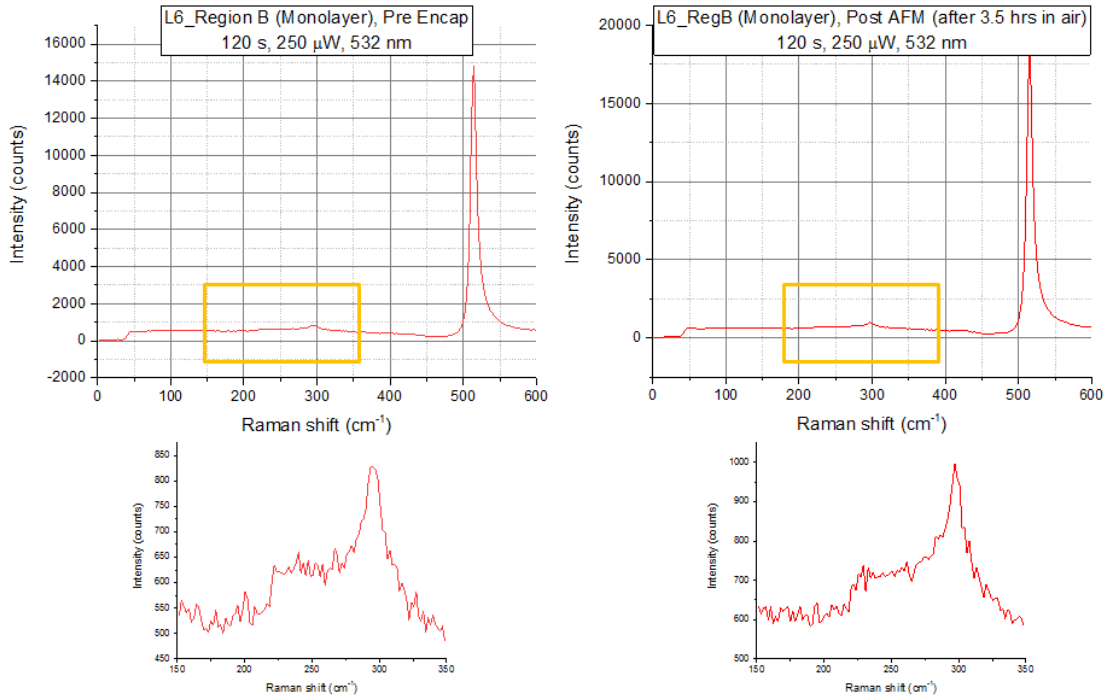

Figure 6.15: Raman spectra of the 1 nm (monolayer) region of $CrCl_3$ before encapsulation (left) and after exposing it to air for 3.5 hours post-encapsulation (right). The data were acquired with an incident laser power of 250 µW over 120 s using a 532 nm laser. The boxed yellow area is enlarged below.

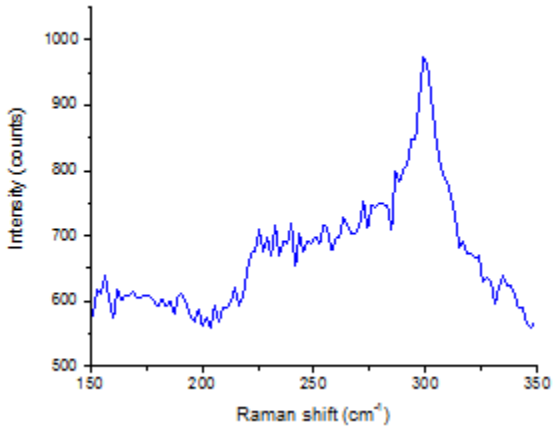

Figure 6.16: Raman spectrum of bare SiO_2/Si for comparison. The data were acquired with an incident laser power of 250 µW over 120 s using a 532 nm laser.

6.6 Conclusions and future work

All in all, the work described in this thesis paves the way for further studies of air-sensitive samples. Optically, one can imagine conducting Raman studies on the remaining chromium trihalides or the ternary compound $Cr_2Ge_2Te_6$ to determine unique characteristics of their respective monolayers given the clear differences in Raman signal between bulk and quasi-2-D crystals. The hBN encapsulation technique can be applied to both the top and bottom of these flakes to seal any gaps that may appear due to the roughness of SiO_2/Si surfaces, and different substrates can be substituted for SiO_2/Si in the case where the 300 cm^{-1} Si peak overlaps with the $CrCl_3$ peak, provided the optical contrast remains sufficiently large. Finally, efforts are underway to find new ways of contacting graphene in graphene/CrI_3 heterostructures and strengthening the prerequisite spin-orbit coupling to observe the QAHE, including prepatterned graphite contacts and introducing a TMD on one side of the graphene.

6.7 References

1. Ferrari, Andrea C., et al. "Raman spectrum of graphene and graphene layers." *Physical Review Letters* 97.18 (2006): 187401.
2. Wang, Qing Hua, et al. "Electronics and optoelectronics of two-dimensional transition metal dichalcogenides." *Nature Nanotechnology* 7.11 (2012): 699.
3. Terrones, H., et al. "New first order Raman-active modes in few layered transition metal dichalcogenides." *Scientific Reports* 4 (2014): 4215.
4. Zhang, Xin, et al. "Phonon and Raman scattering of two-dimensional transition metal dichalcogenides from monolayer, multilayer to bulk material." *Chemical Society Reviews* 44.9 (2015): 2757-2785.
5. Qian, Xiaofeng, et al. "Quantum spin Hall effect in two-dimensional transition metal dichalcogenides." *Science* (2014): 1256815.
6. Weng, Hongming, Xi Dai, and Zhong Fang. "Transition-metal pentatelluride $ZrTe_5$ and $HfTe_5$: A paradigm for large-gap quantum spin Hall insulators." *Physical Review X* 4.1 (2014): 011002.
7. Lin, Ming-Wei, et al. "Ultrathin nanosheets of $CrSiTe_3$: a semiconducting two-dimensional ferromagnetic material." *Journal of Materials Chemistry C* 4.2 (2016): 315-322.
8. Lebègue, Sébastien, et al. "Two-dimensional materials from data filtering and ab initio calculations." *Physical Review X* 3.3 (2013): 031002.
9. Li, Xingxing, and Jinlong Yang. "$CrXTe_3$ (X= Si, Ge) nanosheets: two dimensional intrinsic ferromagnetic semiconductors." *Journal of Materials Chemistry C* 2.34 (2014): 7071-7076.

10. Sivadas, Nikhil, et al. "Magnetic ground state of semiconducting transition-metal trichalcogenide monolayers." *Physical Review B* 91.23 (2015): 235425.
11. Zhang, Wei-Bing, et al. "Robust intrinsic ferromagnetism and half semiconductivity in stable two-dimensional single-layer chromium trihalides." *Journal of Materials Chemistry C* 3.48 (2015): 12457-12468.
12. Huang, Bevin, et al. "Layer-dependent ferromagnetism in a van der Waals crystal down to the monolayer limit." *Nature* 546.7657 (2017): 270.
13. Zwick, A., et al. "Lattice modes in the linear chain compound $ZrTe_5$." *Solid State Communications* 44.2 (1982): 89-94.
14. Keum, Dong Hoon, et al. "Bandgap opening in few-layered monoclinic $MoTe_2$." *Nature Physics* 11.6 (2015): 482.
15. Wang, Kangpeng, et al. "Broadband ultrafast nonlinear absorption and nonlinear refraction of layered molybdenum dichalcogenide semiconductors." *Nanoscale* 6.18 (2014): 10530-10535.
16. Sowden, R. E., J. M. Orza, and S. Montero. "Vibrational spectra of anhydrous chromium (III) chloride." *Polyhedron* 1.5 (1982): 475-477.
17. Park, Jin Cheol, et al. "Phase-engineered synthesis of centimeter-scale 1T′-and 2H-molybdenum ditelluride thin films." *ACS Nano* 9.6 (2015): 6548-6554.

Appendix: Publication list of Dennis Wang

[1] Frenzel, Alex J., McLeod, Alexander S., Wang, Dennis Z., Liu, Yu, Lu, Wenjian, Ni, Guangxin, Tsen, Adam W., Sun, Yuping, Pasupathy, Abhay N., and Basov, Dimitri N. "Infrared Nanoimaging of the Metal-Insulator Transition in the Charge-Density-Wave van der Waals Material 1 T− TaS_2." *Physical Review B* 97.3 (2018): 035111.

[2] Kerelsky, Alexander, Nipane, Ankur, Edelberg, Drew, Wang, Dennis, Zhou, Xiaodong, Motmaendadgar, Abdollah, Gao, Hui, Xie, Saien, Kang, Kibum, Park, Jiwoong, Teherani, James, and Pasupathy, Abhay. "Absence of a Band Gap at the Interface of a Metal and Highly Doped Monolayer MoS_2." *Nano Letters* 17.10 (2017): 5962-5968.

[3] Wang, Dennis, Smyser, Kori, Rhodes, Daniel, Balicas, Luis, Pasupathy, Abhay, and Herman, Irving P. "Passivating 1T′-$MoTe_2$ Multilayers at Elevated Temperatures by Encapsulation." *Nanoscale* 9.37 (2017): 13910-13914.

[4] Tsen, Adam W., Hovden, Robert, Wang, Dennis, Kim, Young Duck, Okamoto, Junichi, Spoth, Katherine A., Liu, Yu, Lu, Wenjian, Sun, Yuping, Hone, James C., Kourkoutis, Lena F., Kim, Philip, and Pasupathy, Abhay N. "Structure and Control of Charge Density Waves in Two-Dimensional 1T-TaS_2." *Proceedings of the National Academy of Sciences* 112.49 (2015): 15054-15059.

[5] Zhang, Datong, Wang, Dennis Z., Creswell, Richard, Lu, Chenguang, Liou, Jonathan, and Herman, Irving P. "Passivation of CdSe Quantum Dots by Graphene and MoS_2 Monolayer Encapsulation." *Chemistry of Materials* 27.14 (2015): 5032-5039.